Modeling Deep-Sea Hydrothermal Plumes and the Circulation Pattern of the Endeavour Ridge Segment

by

Ian Gregory Babcock Adams

(Under the Direction of Daniela Di Iorio)

Abstract

Hydrothermal vents have a large and multidisciplinary impact on the ocean, and represent a rich and diverse field of study. In this research, we focus first on the physical characteristics of an individual plume and second on the influences of hydrothermal venting on fluid circulation patterns over a ridge valley system.

To study the turbulent and internal characteristics of a single focused hydrothermal vent plume, a large eddy simulation (LES) turbulent convection model for a hydrothermal fluid injected into a tidally modulated stratified crossflow is used. The goal is to characterize the fine scale dissipation rates of turbulent kinetic energy (TKE) and thermal variance. In characterizing the turbulent quantities we make several interesting discoveries: the use of isotropic Smagorinsky mixing coefficients is invalid in focused venting for the grid spacing used, the TKE dissipation and thermal

variance dissipation are balanced shear production and vertical advection respectively, and the main contributing factor of the refractive index fluctuations observed by acoustic scintillation is the thermal variance dissipation.

To study the regional effects of multiple venting fields on flow circulation within a ridge valley and to characterize the magnitude and patterns of flow brought about by combined diffuse and focused venting, we utilize the finite-volume community ocean model (FVCOM) to build a high resolution simulation of the Endeavour Ridge segment. Results show the cumulative effects of multiple hydrothermal vent fields, vent induced vertical motion, and strong topographical forcing throughout the region. Our results support the presence of hydrothermal vent driven circulation cells most clearly seen where crossflow is weakest. The scale of these cells is on the order of several hundreds of meters in diameter.

INDEX WORDS: Physical Oceanography, Hydrothermal Vents, Hydrothermal Plumes, Large Eddy Simulation, FVCOM, Endeavour Ridge, Dante

Modeling Deep-Sea Hydrothermal Plumes and the Circulation Pattern of the Endeavour Ridge Segment

by

Ian Gregory Babcock Adams

B.S., Birmingham-Southern College, 2014

A Dissertation Submitted to the Graduate Faculty of the

University of Georgia in Partial Fulfillment of the Requirements for the Degree.

Doctor of Philosophy

Athens, Georgia

2020

Modeling Deep-Sea Hydrothermal Plumes and the Circulation Pattern of the Endeavour Ridge Segment

by

Ian Gregory Babcock Adams

Major Professor: Daniela Di Iorio

Committee: Renato Castelao
Patricia Medeiros
Christof Meile
C. Brock Woodson

Electronic Version Approved:

Ron Walcott
Dean of the Graduate School
The University of Georgia
December 2020

ACKNOWLEDGMENTS

I would like to thank my Advisor, Daniela Di Iorio and the members of my committee for their valuable guidance and feedback through my PhD process, as well as my lab colleagues Jared McKnight, Trevor Richards, James Kelly and Mahdi Razaz. Special thanks to William Lavelle, who developed the turbulent convection model that we modified for our the research projects, and Guangyu Xu for his insightful conversations into computer modeling. I would also like to thank Catherine Edwards for giving me the opportunity to go on fieldwork assignments, and Jaime Palter's lab at URI for including me in their research cruise through UNOLS.

CONTENTS

LIST OF FIGURES

LIST OF TABLES

CHAPTER 1

GENERAL INTRODUCTION

At the deep ocean seafloor where pressures reach hundreds of atmospheres and temperatures can drop as low as 2°C, a fascinating high energy system manifests itself. Magma heated fluid spews out of cracks in the crust, leaking high levels of heat and chemicals into the deep ocean. This process is known as hydrothermal venting. These vents were first discovered in 1977 where on the Galapagos Hydrothermal Expedition a dive with the human occupied vehicle (HOV) Alvin, first laid eyes on a hydrothermal vent (Corliss et al. 1979). This exciting discovery of hydrothermal vents continues to provide a rich opportunity for research across all disciplines of oceanography.

The physical process of hydrothermal venting and plume formation is shown is Figure 1.1. Ambient seawater (2°C) seeps through cracks in the ocean crust at seafloor spreading sites or subduction zones. This ambient fluid then comes into contact with sub-seafloor magma and is heated to high temperatures. As it reaches temperatures up to $450°C$, the seawater exchanges chemicals and minerals with the surrounding rocks and becomes hydrothermal fluid. This hot hydrothermal fluid then escapes from underneath the seafloor at venting locations. It quickly rises under the effects of buoyancy caused by its relatively low density compared to the surrounding seawater. As this hydrothermal fluid rises, it entrains ambient seawater

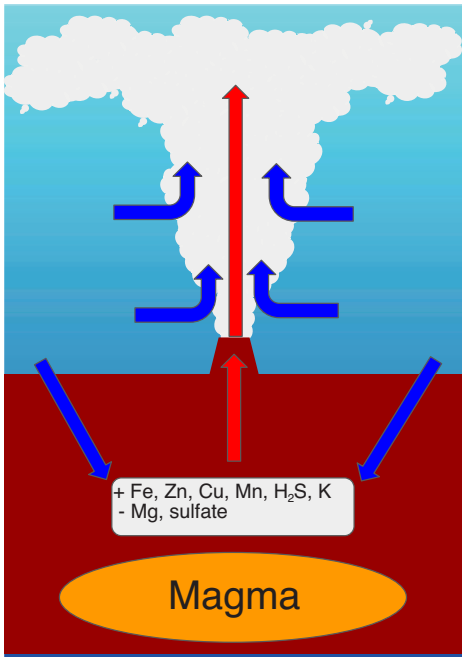

Figure 1.1: Hydrothermal effluent, caused by bottom water percolating through cracks in the crust, exchanging heat with the magma and chemicals with the subseafloor, and interacting with the bottom ocean to form a high-temperature chemically-laden turbulent plume

containing nutrients and small organic matter, and forms a turbulent buoyant plume. It eventually reaches a depth of neutral buoyancy, where the plume spreads out over a large horizontal area. This process is an important mechanism that transports heat, leached chemicals, and entrained fluid into the deep ocean, particularly when the effects of hydrothermal venting locations are scaled up over all mid-ocean ridges where venting is known to occur.

Although the primary focus of this dissertation is on the physical characteristics and phenomena brought about by hydrothermal venting, it is important to discuss the broader impacts of vent research on diverse fields of

oceanography. Hydrothermal fluid is rich in dissolved metals such as iron, copper, zinc, potassium and manganese, as well as the neutral compound hydrogen sulfide (Millero 2013). As the dissolved metals in the hot effluent mix with the cold oxygen rich ambient water, some metal compounds such as metal sulfides precipitate out forming the characteristic chimney structures of the vent. The chemicals and heat remaining in the plume are advected upwards through the water column, and can be carried all the way to the plume's neutrally buoyant layer (at a depth dependent on both stratification and the initial buoyancy flux) where they are then horizontally dispersed. In this way hydrothermal plumes act both as a source of chemicals in the deep ocean, as well as a mechanism for dispersal of those chemicals. Hydrothermal plume chemistry has many applications, both near to and far from the venting sites. The chemicals transported by hydrothermal plumes can be found tens of kilometers away from the venting site (Moffett and German 2018), and have impacts into our understanding of chemical cycling in the ocean. It's important to note that although the plume is rich in many chemicals, it is strongly depleted in both magnesium and sulfate (Millero 2013). In fact, the absence of magnesium is so marked that diminished levels in the deep ocean are used as an indication of hydrothermal venting (Wright and Rothery 1989).

Because hydrothermal vents are known to introduce significant quantities of metals into the deep ocean there is naturally a great deal of interest in the chemical consequences of those metals (Stüben et al. 1992; Resing et al. 2015). Perhaps the most studied plume metal is iron (Fe), due to its importance as an oceanic nutrient

and its relative scarcity. Because the plume is a significant source of iron, its influence on the wider ocean will depend on its ultimate fate. It has been established that the iron can be transported far from the localized venting source (Wu et al. 2011; Nishioka et al. 2013; Fitzsimmons et al. 2014). This long range transport of iron has a global impact on ocean biogeochemistry (Resing et al. 2015; Tagliabue and Resing 2016). An interesting study by Sander and Koschinsky (2011) shows that organic matter in hydrothermal effluent can form metal complexes in the plume to stabilize them, thereby increasing the availability of metals for transport throughout the oceans. Analysis of particulate matter from a hydrothermal vent on the East Pacific Rise found that mineral-containing aggregates were always associated with organic matter and that the organic matter biomass was rich in sulfur (Breier et al. 2012), again pointing to the importance of hydrothermal vent effluent in the biogeochemical cycle.

The GEOTRACES program is a multinational interdisciplinary program aimed at quantifying trace elements and isotopes in the ocean and understanding the mechanisms of transport. German et al. (2016) examined the global impact of hydrothermal activity on trace elements and isotopes (TEIs), and discussed the implications in terms of future GEOTRACES research. In 2018 such a comprehensive study of TEIs within hydrothermal vents was carried out under the auspices of GEOTRACES (Moffett and German 2018).

The abundance of chemical micro-nutrients along with the heat generated by the hydrothermal venting sites provides an environment where diverse biology has

been found to flourish. These organisms have adapted to the high temperatures to take advantage of the nutrient rich, high energy system. One of the biggest surprises in the discovery of hydrothermal vents was the presence of a very diverse community of life. Hydrothermal vents support a diverse community of extremophiles that thrive in an ecosystem previously thought to be untenable to native life. In addition, the plume assists in the migration of vent communities by transporting larvae and nutrients. While most people are familiar with the giant tubeworms, snails, slugs, and crabs that surprised the scientists on the Alvin, more closely connected to the hydrothermal effluent are the chemosynthetic microbes which are the basis of the food chain. Extensive microbial communities have been found on chimney surfaces (Takai et al. 2008), within the subseafloor vent environment (Reveillaud et al. 2016), and inside the vent plume itself (Bennett et al. 2011). A large amount of work has been done on these microbial communities that live around hydrothermal vents, as well as the complex interdependencies they have with eachother (Mullineaux et al. 2018) and the plume system (Dick et al. 2013). Perhaps most interestingly, the hydrothermal vent is thought to be a close representation to prelife earth conditions, and the biogeochemistry occurring at these venting sites could give insight into the processes that brought about the existence of the first living particles on earth (Barge et al. 2019; Herschy et al. 2014; Barge et al. 2015).

Geologically, hydrothermal venting provides a window into the Earth's interior, giving information on the composition and temperatures of sub-seafloor rock. The interactions between the deep ocean water and the subseafloor geological

conditions are complex and multi layered, making it difficult to fully analyze the system. As direct measurements of subseafloor processes are quite difficult, one way in which the geology of venting sites can be interrogated is through examination of the composition and activity of the hydrothermal plume. These hydrothermal systems are intricately linked to sub-seafloor geology.

The contents of the plumes not only tell us the kinds of materials that exist beneath the crust (as well as the chemical reactions taking place), but hydrothermal systems are constantly influenced by geological events. Perhaps most notably was the Axial seamount megaplume event that occurred in 2015. This event released a large amount of vent effluent and heat into the ocean, influencing chemical and flow patterns (Xu et al. 2018). Physical responses in hydrothermal venting have long been observed in respose to seismic events (Baker et al. 1995). Hydrothermal fluid characteristics have also been investigated as an indicator of magmatic activity, further relating geological seismic events and hydrothermal activity (German et al. 2020). The more hydrothermal venting is studied (particularly over longer and longer timescales), the more links between geological actions and venting will be discovered.

One of the critical aspects of research in regions of hydrothermal venting has been locating venting sites to determine how widespread the phenomenon is and to characterize different types of venting. In the years since they were discovered, it has been established that submarine venting is widely distributed globally (Baker et al. 1995; Baker and German 2004; Beaulieu et al. 2015). Research into vents isn't limited to the deep sea, as hydrothermal activity can be found in many different

locations across the world. Volcanic activity can cause hydrothermal vents to occur within large lakes, such as the one at Yellowstone Park. Here researchers investigate the hydrothermal effluent to better understand the underground composition and history of this highly volcanic site (Linder 2017). These vents are part of the worlds largest continental hydrothermal system, and have also been studied to elucidate the hydrothermal response to geological and environmental influences (Sohn et al. 2017).

The physics of hydrothermal plumes is complex and yet holds the key to unraveling local and regional oceanographic and geological behavior. The turbulent plume that arises from hydrothermal venting is of interest to physical oceanographers. Study has examined physical relationships of plume rise and entrainment of ambient fluid (Turner 1986). The hydrothermal vent has also been found to emit ambient light, thought to be caused by fluid mixing and highly turbulent behaviour (White et al. 2002).

Turbulent flow generated by shear cascades plume energy down to smaller and smaller scales until it is dissipated by friction, transferring plume energy into the ocean and mixing hydrothermal fluids in the deep sea. The rate at which this energy dissipates, what factors control the rate of dissipation, and how turbulent the plume becomes, all affect plume characteristics such as rise height, size, and area of influence. A thorough description of general plume characteristics can be found in the classic book by Turner (1979). A plume is defined as any column of fluid moving through another. Generally, buoyant discharge can be classified as a pure jet, a pure plume, or something in between. The distinction between jets and plumes is in the

motive force. In a jet, the moving column of fluid is propelled by momentum. Jets are most often characterized by a large source velocity. In a plume, the fluid is instead driven by buoyancy, and doesn't necessarily have a large initial source velocity. As a jet or plume develops through the ambient fluid, some turbulent mixing occurs. This causes the rising water to lose its momentum or buoyancy. Turbulent entrainment also serves to widen the plume, causing greater diameters farther from the plume source.

After the plume effluent has reached a zone of neutral buoyancy, the plumelike physics may have dissipated, but it is still a rich location of physical interest. Flows within hydrothermal systems such as ridge valleys are important to characterize, because they give important transport information away from the venting site. In a study of the Mid Atlantic Ridge, Thurnherr et al. (2002) found that vertical shear within the valley contributed strongly to the mixing of hydrothermal effluent within the ridge. Surface eddies have also been seen to alter the flow of hydrothermal effluent. These large eddies capture effluent and transport the hydrothermal fluid much farther (and in different directions) than it would have otherwise spread (Adams et al. 2011).

Plume physics is a challenging subject to research because the remote location and high temperature conditions present unique measurement problems. For this reason, a wealth of sophisticated and interesting techniques have been developed for the study of hydrothermal vents. Vent plumes can be difficult to locate, and recent research has been focused on the use of both autonomous underwater vehicles

(AUVs) and remote operated vehicles (ROVs) in tandem with 3D imaging to produce detailed pictures of the seafloor and to locate hydrothermal vent sources (Teague et al. 2017). Turbulence in the plume has been investigated through the use of vertical microstructure profilers (VMPs) (Thurnherr and Laurent 2012). Rona et al. (2002) developed a technique using acoustic imaging and visualization to construct a 3D picture of two adjacent black smokers to infer vertical rise velocities and heat flux. Sarrazin et al. (2009) used a flow dual sensor to investigate the low temperature diffuse venting that occurs through a hydrothermal venting field. Until relatively recently, studies of jet and plume behavior have been consistently dominated by experimental approaches (Kotsovinos and List 1977; Kotsovinos 1977; George et al. 1977; List 1982; Papanicolaou and List 1987; Dai et al. 1994; Papanicolaou and List 1988). These observational experiments consisted of physical measurements of lab generated plumes, often on small scales, via fluid injection. Another useful tool to study hydrothermal venting is modeling. Since this dissertation consists of original modeling studies of hydrothermal vent plumes, related background and current work in modeling is presented in subsequent sections to emphasize relevance and connections to our work.

Vent research has applications well beyond the deep ocean, even reaching other worlds. Exploring Ocean Worlds (EXOW) is a multidisciplinary NASA project designed to "identify ocean worlds, characterize their oceans, evaluate their habitability, search for life, and ultimately understand any life [they] find" (Hendrix et al. 2019). The Roadmap Ocean Worlds (ROW) team identifies a potential

environment for ocean world life as having two main conditions: A source of energy, and a mechanism for exchange of resources. Hydrothermal vents are a key component to this mission as they provide the environment (energy and nutrients), the transport mechanism, and a means to interact with ocean circulation. Venting has been found to occur on the ocean world Enceladus, and it has been proposed that hydrothermal vents exist on other ice-covered ocean worlds as well (Hendrix et al. 2019). Thus it is important to characterize hydrothermal vents on ocean worlds, and modeling the hydrothermal interactions is a powerful method to study a system that isn't readily accessible. These ocean world hydrothermal vent conditions are being recreated in the lab, to examine if they could generate molecules associated with life (Barge et al. 2015) (Barge et al. 2019). Earth observation of hydrothermal effluent is also being made to provide a biological and chemical context for any measurements a probe would make (German et al. 2020).

Since their discovery in 1977 (Corliss et al. 1979), the known number of hydrothermal vent sites has increased tremendously (Beaulieu and Szafranski 2018). The InterRidge society database (Beaulieu and Szafranski 2018) lists nearly 700 active and inactive venting fields, with each site typically containing multiple venting sources. The prevalence of hydrothermal vents is thought to be quite large, with concentrations centered around mid ocean ridge locations (Baker and German 2004). Given the extent of mid ocean ridge (MOR) coverage on the seafloor, hydrothermal venting has implications to the global ocean heat budget as a potentially widespread collection of heat sources.

Hydrothermal vents exist in clusters of venting activity. These are known as vent fields, and incorporate multiple distinct venting zones of various temperatures. They typically span diameters of 100m, and take spatially diverse shapes. They are characterized by large chimneys formed from the mineral precipitate that falls out of the hydrothermal effluent.

Within the venting field there are two distinct types of hydrothermal venting - focused flow and diffuse flow. Focused flow is what is typically thought of when imaging the plume that arises from high temperature vents; focused flow is emitted from specific spots within the vent field. The effluent reaches temperatures of up to 450 °C, with large buoyantly driven vertical velocities. They contain large concentrations of chemicals as has been previously discussed, and are the main driving contributors to the formation of the mineral chimneys that typify the venting field. Diffuse flow is a much lower temperature phenomenon than focused flow, but is still reasonably warm (20-40 °C) relative to the deep sea. Diffuse flow occurs throughout the entire venting field. Concentrations of vent originating chemicals are also typically lower than in focused flow. Despite this, it is thought that diffuse flow is a larger contributor to both chemical and heat flux to the global ocean, as it covers a much larger area, and thus accounts for a greater portion of the total venting activity worldwide.

1.1 Endeavour Ridge Segment

The Endeavor Ridge segment of the Juan De Fuca Ridge is located 300 km off the coast of Washington state in the Northeast Pacific at an average depth of 2000 meters. It is an active spreading center 10 km long and 1 km wide. Two crests of rock flank the ridge valley, which contains five distinct hydrothermal venting fields spaced approximately 2 to 3 kilometers apart. The region along with the location of each of the venting fields, is shown in Figure 1.2. Each vent field can release hydrothermal effluent as hot as 350 °C (Kelley et al. 2001). The Juan de Fuca Ridge is characterized by tidal, inertial and weather band period influences, with near ridge intensification indicative of trapped subinertial flow motion (Lavelle and Cannon 2001). Although the region is well understood, the heat budget estimates of the Juan de Fuca Ridge have exhibited a wide range of values (McDuff 1995).

The five main vent fields located within the valley of the Endeavour Ridge are approximately 100 m in diameter, and vent via both high temperature focused flow and low temperature diffuse flow. Small groups of individual venting sites within the fields form venting chimneys, which create rising hydrothermal fluid that coalesces into distinct plumes at heights of approximately 10 meters above the venting source (Lupton et al. 1985). These focused flow plumes can reach rise heights a few hundred meters above the venting sources, where entrainment and mixing cause the effluent to reach neutral buoyancy (Lupton et al. 1985). Depending on the location of the venting source, hydrothermal plumes may be bounded by the ridge walls. Deeper

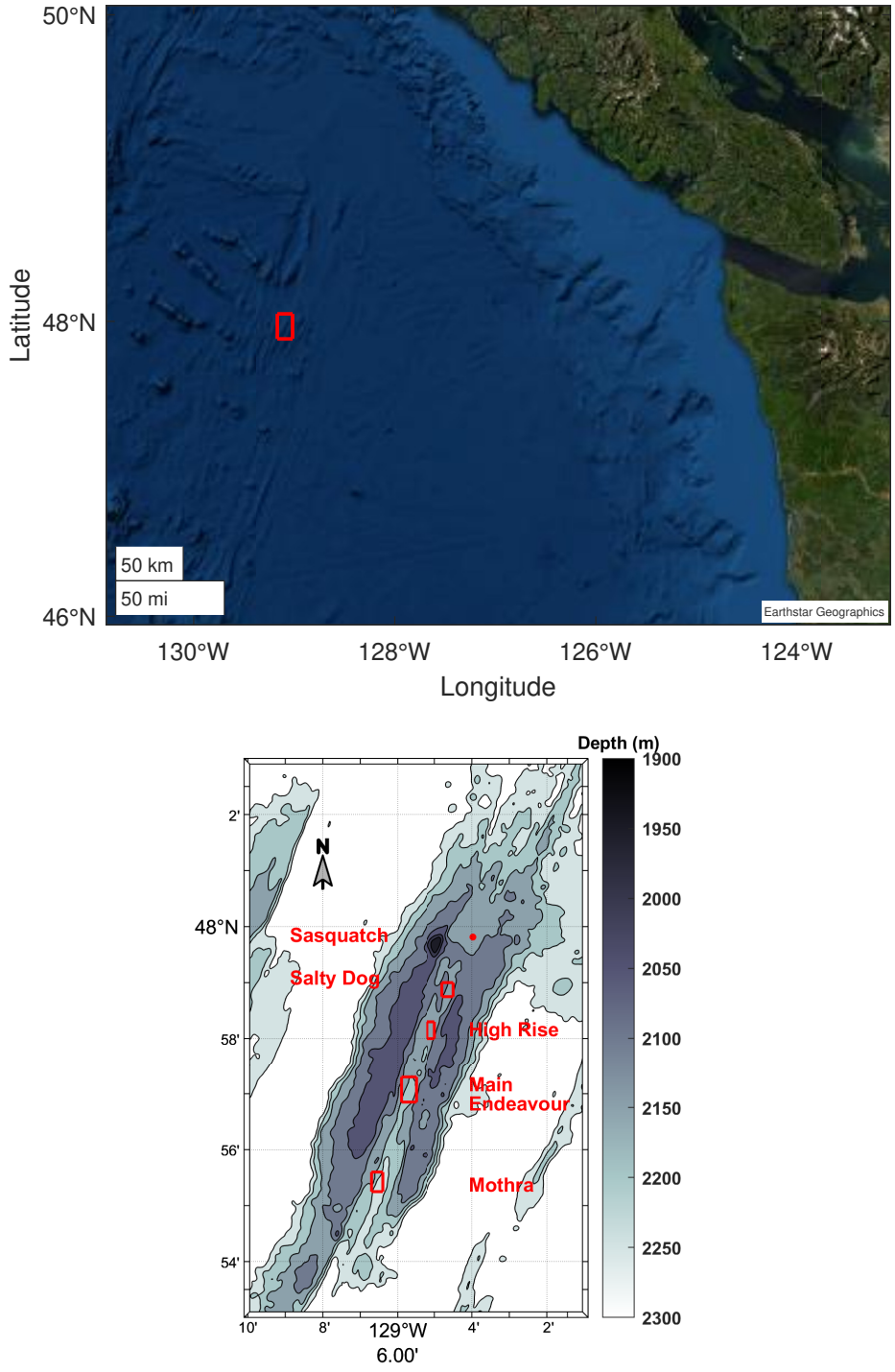

Figure 1.2: The features of the Endeavour Ridge Segment of the Juan de Fuca Ridge are shown, along with the locations of venting fields within the ridge valley.

plumes reach neutral buoyancy below the ridges, while shallower plumes can achieve a rise height above the ridges and escape the system. These shallower plumes are typically advected westward. Venting fields in the Southern part of the Endeavour Ridge have higher venting when compared to those in the north. This is due to the relative age of the fields. Fields in the South (Mothra, Main Endeavour, and High Rise) were formed more recently than their Northern counterparts (Sasquatch and Salty Dawg). The Endeavour Segment is a highly researched area and a number of experiments have been carried out that provides motivation for the research presented here.

A detailed understanding of plume characteristics is important for two overarching reasons. First, plume characteristics are influenced by geological and oceanographic events, such as changes in internal temperature, tectonic motion, and tidal events. If we understand how hydrothermal activity reacts to specific geological and oceanographic forcings, we can infer those forcings via hydrothermal plume observation. Second, if the connection between deep sea currents and plume characteristics can be established, we can draw conclusions about what deep sea currents would look like given location and number of venting sites. For example, interactions between hydrothermal plume dynamics and deep sea currents could give insight on how circulation is modified near a venting site, such as the development of a circulation cell in which water is brought into the vent system and transported upward via entrainment.

1.2 Outline of Dissertation

To investigate plume dynamics, we will use two different methods to explore the physical characteristics and influences of hydrothermal venting. Chapter 2 (a submitted manuscript) uses a Large Eddy Simulation (LES) model to focus on a single vent plume to elucidate the important mechanisms by which the venting activity injects and disperses turbulent energy throughout the ocean bottom. Chapter 3 examines the effects of different source conditions on the plume turbulence characteristics using results from the same model used in the previous chapter. Chapter 4 describes a project designed to explore the effects and influences that multiple hydrothermal venting fields have on regional currents through a spreading ridge using a variable resolution FVCOM mesh. Chapter 5 gives overall conclusions to the research presented and recommendations for future work

CHAPTER 2

TURBULENT PROPERTIES OF A DEEP-SEA HYDROTHERMAL PLUME IN A TIME VARYING CROSSFLOW

Adams, I. G. B., and D. Di Iorio. Submitted to Journal of Geophysical Research - Oceans, 09/19/2020

Abstract

A large eddy simulation is applied to a high temperature hydrothermal vent plume in a stratified and tidally modulated crossflow, to identify the turbulence and mixing characteristics. The model parameters and source conditions that best represent the vertical velocity and refractive index fluctuations, measured 20 m above the Dante sulfide mound in the Main Endeavour vent field, are a heat transport of 50 MW over a cross sectional area of 4×4.5 m^2. From this model run with output up to 25 m above the source and with 1 Hz sampling, the shear production of turbulent kinetic energy (TKE), the mean and turbulent transport of TKE, and the buoyancy production/dissipation are quantified showing that shear production dominates. Similarly, thermal variance production, and its mean and turbulent transport, are also quantified showing that the advective term dominates. Because of enhanced entrainment of ambient water into the plume during strong crossflows all the mean and turbulent quantities show tidally modulated values. Assuming steady state, the dissipation rates are evaluated. During strong crossflow the tilting of the vertical velocity contours and isotherms plays a critical role in the stability of the plume and in creating high shear and thermal gradients on the upstream side of the plume center axis. These dissipation rates are used to quantify the refractive index fluctuations and given the high thermal dissipation quantities, it is the main contributing factor in acoustic forward scatter.

Plain Language Summary

At mid ocean ridges, magma heated fluid, flows out of cracks in the crust, releasing high levels of heat and chemicals into the deep ocean in the form of hydrothermal plumes. Because of its buoyancy it quickly rises forming a turbulent convective plume and entrains ambient seawater creating a transport mechanism into the deep ocean. Ocean currents complicate the rise of the buoyant plume limiting its rise height by enhancing the amount of ambient water entrained into the plume resulting in tidally modulated vertical velocities, turbulent properties and rise heights. Modeling these systems lead to better understanding of the mixing strengths within the plume and the rates at which turbulent kinetic energy (TKE) and temperature variations are produced and dissipated. These quantities are almost impossible to measure in a deep sea hydrothermal vent environment. Results show that shear is the primary mechanism for producing TKE and that advection of temperature variability by the mean and turbulent vertical velocity is the primary mechanism for producing temperature fluctuations at 20 m above the vent orifice.

2.1 Introduction

Hydrothermal vents inspire widespread interest across multiple disciplines of oceanography. Since their discovery in 1977 (Corliss et al. 1979), the known number of hydrothermal vent sites have increased to nearly 700 active and inactive venting fields, with each site typically containing multiple venting sources (The InterRidge

Vents Database (Beaulieu and Szafranski 2018)). The number of yet-to-be-discovered hydrothermal fields is also thought to be quite large, primarily centered around inter ridge locations (Baker and German 2004). Current oceanographic research explores a wide variety of phenomena that occur in the vicinity of hydrothermal vents. Hydrothermal vents provide a complex habitat for a diverse population of organisms. The plume activity and effects have been linked to deep sea pelagic food webs (Phillips 2017). Trace metal concentrations, and their partitioning, within the plumes contribute to chemical budgets for the deep ocean (Findlay et al. 2015). The chemical contributions of hydrothermal vent plumes are also being investigated as potential drivers for change in sedimentary accumulation rates (Cullen and Coogan 2017).

Of particular interest to physical oceanographers are the development and characteristics of the hydrothermal vent plume itself. Hydrothermal vents provide an injection point of hot fluid at the ocean floor, into an ambient environment of cold, stably stratified water, forming a turbulent plume. As the plume rises under its buoyancy tidal and aperiodic cross flows cause plume bending and tidal variance of plume characteristics (Xu and DiIorio 2011). Some plume properties of interest are vertical rise velocities, mixing strengths, turbulent temperature variance and dissipation as well as turbulent kinetic energy production and dissipation. In exploring the development of plume properties, computer modeling is ideally suited for obtaining detailed information where experimental data are difficult if not impossible to obtain.

Models of hydrothermal vent plumes in steady and tidally varying crossflows with realistic stratification has been developed and examined previously (Lavelle et al. 2013; Lavelle 1997). The basic model is a three-dimensional time-dependent non-hydrostatic large eddy simulation. Large eddy simulations use numerical evaluation of the spatially or temporally filtered momentum (the Navier Stokes equations), heat, salt and mass conservation equations to resolve large scale eddies. Small scale eddies are approximated via large eddy mixing parameterizations. A hydrostatic approximation would not be suitable for these plumes because of the strong buoyancy induced vertical accelerations in the plume stem. One of the key goals in this paper is to use the three dimensional convection model to explore the turbulent characteristics of the fully developed plume. Of particular interest are the internal processes that contribute to turbulent production and dissipation rates of kinetic energy and thermal variance assuming a steady state balance. These components are not easily resolvable with typical ocean instrumentation, but they can be examined with a the turbulent convection model. The turbulent dissipation rate for kinetic energy can be estimated from the Reynolds averaged sub-scale turbulent shear production, buoyancy production (or dissipation) and from the mean and turbulent transport of turbulent kinetic energy. In the same way, the turbulent dissipation rate for thermal variance is estimated from thermal gradients and from the mean and turbulent transport of thermal variance.

Field observations of the mean vertical velocity and the level of refractive index fluctuations (see Figure 2.1) were earlier obtained at the Endeavour Segment,

Juan de Fuca Ridge in the NE Pacific within the hydrothermal vent plume at Dante within the Main Endeavor Field (Xu and DiIorio 2011). Dante is a sulfide mound rising to a height of 25 meters above the seafloor that has multiple vent chimneys. This particular structure is one of many within the Main Endeavor Field, being the next to southmost cluster of five vent fields within the Endeavour segment. The chimney itself is a conglomerate of several distinct small smoker discharge areas distributed over its surface. These venting orifices create plumes which combine or coalesce to form the plume that is considered to be the Dante plume. This can be presumed, as the coalesced plume from a series of sources is indistinguishable from a single plume originating at a virtual point source located some distance below the height at which the distinct plumes have coalesced into a single plume (Kaye and Linden 2004). It is at this coalesced height that the model initiates and to find the virtual source depth of the model, information about entrainment and upward flux is obtained.

Field observations were also used to assess the best set of model parameters. Different source areas, heat transport and vertical mixing (Smagorinsky) coefficients are considered and the level of the refractive index fluctuations (denoted by the structure parameter $C^2_{n_{eff}}$) is obtained. This parameter is dependent on the thermal variance dissipation rate (ϵ_θ), and the kinetic energy dissipation rate (ϵ) and the measurement cannot distinguish between the two in forward acoustic scatter experiments. The vertical Smagorinsky coefficient for eddy viscosities (and hence diffusivities) were varied to test its effect the turbulence and vertical velocity.

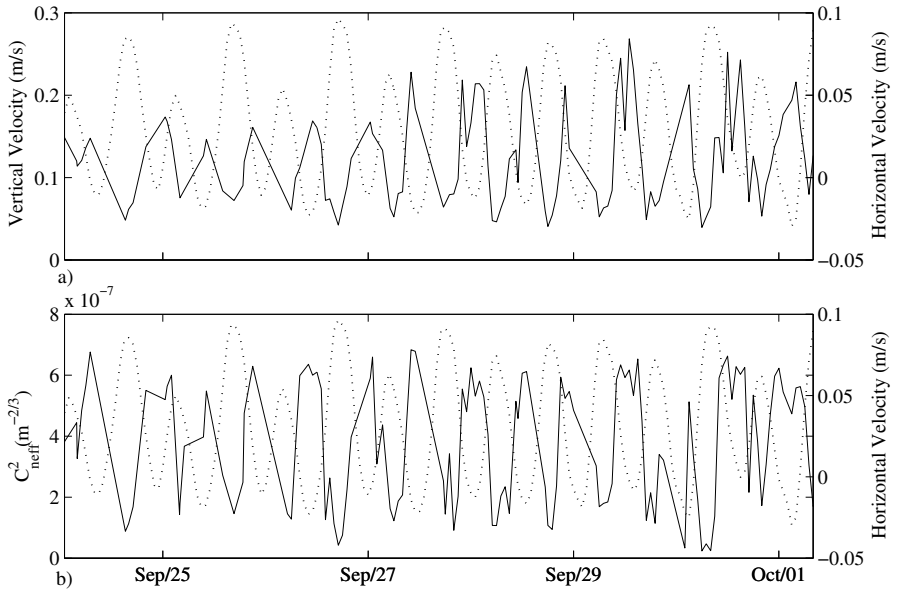

Figure 2.1: Acoustic scintillation measurements at a height of 20 m above the Dante sulfide mound (Xu and DiIorio 2011) of the a) vertical velocity and b) refractive index structure parameter over an 8 day time period. The horizontal current aligned along the acoustic propagation path is denoted as a dotted line.

Section 2.2 describes the model equations, and quantifies the turbulence equations that are used to study the turbulent properties of a hydrothermal plume (eddy scale mixing, buoyancy and shear production, mean and turbulent transport and the inferred dissipation quantities). Section 3 shows model results and compares to observations to find an experimental run that closely resembles the measured vertical velocity and refractive index fluctuations. Turbulent properties for kinetic energy, thermal variance and refractive index for this run are then discussed. Section 2.4 summarizes and concludes key findings.

2.2 Methods

The model developed by Lavelle (1997) and Lavelle et al. (2013) for hydrothermal plumes in steady and time varying cross flows is modified in order to study the turbulent properties of plumes. What is different about the model in this paper is that a calculated Richardson number is included to quantify the vertical mixing; the horizontal and vertical shear strain rates are also redefined. Model parameters and output are then chosen so that the large eddy simulations capture the turbulent characteristics of a deep sea hydrothermal plume.

Model Equations

A detailed description of the turbulent convection model for a hydrothermal fluid discharging into a tidally modulated, stratified cross flow is outlined in Lavelle et al. (2013). The model horizontal currents (u_{BKG}, v_{BKG}) here are extrapolated from the

tidal currents estimated in Xu and DiIorio (2012) and the stratification (θ_{BKG}) is based on measurements made in 2008. The large eddy simulation requires only that the length scales within the inertial-subrange are resolved in order to estimate the dissipation rates and that the velocity field does not need to be resolved down to the Kolmogorov scale. The large eddy equations for velocity ($\mathbf{u}$), continuity, and temperature (θ) (similar equations exist for salinity and an arbitrary concentration) are respectively:

$$\frac{\partial}{\partial t}\mathbf{u} + \mathbf{u}\cdot\nabla\mathbf{u} = -\frac{\nabla p}{\rho_o} - 2\mathbf{\Omega}\times\mathbf{u} - \nabla\cdot\tau/\rho_o - g\rho/\rho_o\hat{k} - \alpha\cdot(\mathbf{u}-\mathbf{u}_{BKG}) + \mathbf{F}_B \quad (2.1)$$

$$\nabla\cdot\mathbf{u} = 0 \quad (2.2)$$

$$\frac{\partial}{\partial t}\theta + \mathbf{u}\cdot\nabla\theta = -\nabla\cdot\mathbf{q} + Q_\theta - \alpha_s(\theta-\theta_{BKG}) \quad (2.3)$$

where t is time, p is pressure, ρ is density ($\rho_o = 1025\text{kg/m}^3$ is a fixed reference density), $g = 9.81$ m/s^2 is the gravitational constant, and the vertical Coriolis parameter is $2\Omega\sin(47.95) = 1.08\times10^{-4}$ s^{-1}. The body force $\mathbf{F}_B$ is related to the tidal forcing and Q_θ is related to the source heat flux with multiplicative constants ρ_o and specific heat $c_p = 4200$ J/(kg^{o}C) canceled in each term of the heat equation. Sponge functions are denoted by α and α_s. See Lavelle et al. (2013) for more detailed explanation of these terms.

The momentum flux (stress tensor) is τ/ρ_o and the heat flux is $\mathbf{q}$, both of which must be modeled by introducing an eddy viscosity and diffusivity respectively. For an incompressible fluid, assuming rotational symmetry about the z-axis, the

momentum (see Wajsowiczw (1993) and Smagorinsky (1993)) and heat fluxes, can be expressed as,

$$\begin{aligned}
\tau_{ij}/\rho_o &= -A_{ijkl}S_{kl} \\
&= -\begin{bmatrix} A_H(S_{11}-S_{22})-\nu S_{33} & 2A_H S_{12} & 2A_V S_{13} \\ 2A_H S_{12} & -A_H(S_{11}-S_{22})-\nu S_{33} & 2A_V S_{23} \\ 2A_V S_{13} & 2A_V S_{23} & 2\nu S_{33} \end{bmatrix} \qquad (2.4) \\
&= -\begin{bmatrix} 2A_H S_{11} & 2A_H S_{12} & 2A_V S_{13} \\ 2A_H S_{12} & 2A_H S_{22} & 2A_V S_{23} \\ 2A_V S_{13} & 2A_V S_{23} & 2A_H S_{33} \end{bmatrix} \qquad (2.5) \\
\mathbf{q} &= -K\nabla\theta = -\mathrm{Pr}^{-1}\left(A_H\frac{\partial\theta}{\partial x}, A_H\frac{\partial\theta}{\partial y}, A_V\frac{\partial\theta}{\partial z}\right) \qquad (2.6)
\end{aligned}$$

where $S_{ij} = 1/2(\partial u_i/\partial x_j + \partial u_j/\partial x_i)$ is the symmetric strain rate tensor with $S_{ii} = 0$ (continuity) and the coefficients A_H, A_V are identified as the horizontal and vertical eddy viscosities. The third viscosity ν in equation (4) is referred to as the bulk viscosity and can range from 0 to A_H (Williams 1972). Here $\nu = A_H$ and the properties of the stress tensor are: it is symmetric $\tau_{ij} = \tau_{ji}$, and it reduces to $\tau_{ij}/\rho_o = -2AS_{ij}$ when the viscosity is forced to be isotropic $A = A_H = A_V$. The eddy diffusivity $K_{H,V} = A_{H,V}\mathrm{Pr}^{-1}$, where Pr is the Prandtl number held constant.

Following the method of Smagorinsky (1963) and Smagorinsky (1993) and Lilly (1962), the eddy viscosities and hence diffusivities in the horizontal and vertical

can be written in terms of Smagorinsky coefficients and the shear strain rates as,

$$A_H = (C_{SH}\ell_{SH})^2 S_H + A_{Hmin} \tag{2.7}$$

$$A_V = (C_{SV}\ell_{SV})^2 S_V \left(1 - \frac{\mathrm{Ri}}{\mathrm{Pr}}\right)^{1/2} + A_{Vmin}. \tag{2.8}$$

where the grid length scales, $\ell_{SH} = (\mathrm{dx\ dy})^{1/2}$ and $\ell_{SV} = \mathrm{dz}$ are dependent on the computational cell lengths (dx, dy, dz). Two vertical Smagorinsky coefficients are tested while keeping the horizontal coefficient constant. The horizontal and vertical shear strain rates are respectively,

$$S_H^2 = 2S_{11}^2 + 2S_{22}^2 + 4S_{12}^2 + 2S_{33}^2 \tag{2.9}$$

$$= \left[2\left(\frac{\partial u}{\partial x}\right)^2 + 2\left(\frac{\partial v}{\partial y}\right)^2 + \left(\frac{\partial u}{\partial y} + \frac{\partial v}{\partial x}\right)^2 + 2\left(\frac{\partial w}{\partial z}\right)^2\right] \tag{2.10}$$

$$S_V^2 = 4S_{13}^2 + 4S_{23}^2 \tag{2.11}$$

$$= \left[\left(\frac{\partial u}{\partial z} + \frac{\partial w}{\partial x}\right)^2 + \left(\frac{\partial v}{\partial z} + \frac{\partial w}{\partial y}\right)^2\right] \tag{2.12}$$

Similarly, the square of the horizontal and vertical temperature gradients are defined as,

$$\Theta_H^2 = \left[\left(\frac{\partial \theta}{\partial x}\right)^2 + \left(\frac{\partial \theta}{\partial y}\right)^2\right] \tag{2.13}$$

$$\Theta_V^2 = \left[\left(\frac{\partial \theta}{\partial z}\right)^2\right] \tag{2.14}$$

Each term in S_H^2, S_V^2, Θ_H^2 and Θ_V^2 are all positive definite and it ensures that the turbulent shear and thermal gradient production quantities are all positive, that is, the momentum and heat fluxes will act as sources of TKE and thermal variance respectively.

The Richardson number is defined as, $\mathrm{Ri} = N^2/[(\partial u/\partial z)^2 + (\partial v/\partial z)^2]$ and the stratification is $N^2 = -(g/\rho)\partial\rho/\partial z$ both of which are calculated as a function of time in the model. When $\mathrm{Ri} > \mathrm{Pr} = 3$ (for very stable conditions which are expected outside the plume region) the vertical mixing is set to the background mixing level A_{Vmin}. Background mixing levels in the horizontal and vertical are set as $A_{(H,V)min} = (5 \times 10^{-4},\ 5 \times 10^{-5})$ m^2/s as in previous model runs (Lavelle et al. 2013).

Table 2.1 outlines six model experiments with different source areas $(3 \times 3, 4 \times 4.5, 6 \times 6)$ m^2, heat transports (50, 80) MW, or Smagorinsky coefficients ($C_{SH} = 0.14$, $C_{SV} = [0.04,\ 0.14]$) that were run to find conditions that most resemble observational measurements of plume vertical velocity and turbulent refractive index. The model spatial domain was divided into 192-128-192 cells in the x-y-z directions with computational cell sizes dx=1m, dy=1.5m, dz=2m respectively. The model time step was 1 s and the model was run for 36 hr. Initial model conditions were no flow with temperature and salinity fields based on laterally uniform hydrographic profiles taken from prior ocean measurements at Dante Lavelle et al. 2013. Model cross flow velocities were ramped up over 12 hours to the periodic velocities shown in Figure 2.3 to resemble the horizontal currents observed in Figure 2.1; the heat flux was centered on the source origin in the x-y plan and at 2175 m depth and was ramped

Table 2.1: Model experiments with varying source conditions (heat transport and area) and vertical Smagorinsky coefficients.

	Source Area	Heat transport	Smagorinsky coefficient	z0
Exp 1 (red)	4m×4.5m	50 MW	$C_{SH} = 0.14$ $C_{SV} = 0.04$	2176 m
Exp 2 (green)	6m×6m	50 MW	$C_{SH} = 0.14$ $C_{SV} = 0.04$	2178 m
Exp 3 (blue)	3m×3m	50 MW	$C_{SH} = 0.14$ $C_{SV} = 0.04$	2173 m
Exp 4 (cyan)	3m×3m	50 MW	$C_{SH} = 0.14$ $C_{SV} = 0.14$	2177 m
Exp 5 (black)	3m×3m	80 MW	$C_{SH} = 0.14$ $C_{SV} = 0.04$	2176 m
Exp 6 (magenta)	3m×3m	80 MW	$C_{SH} = 0.14$ $C_{SV} = 0.14$	2180 m

up to Table 2.1 values over the same time period. Once the ramp up period was over, model results were saved hourly over the entire domain and were also saved for each 1 s time step over a smaller domain of 101-43.5-26 m for turbulence analyses.

Turbulence quantities

Spatial and temporal averaging is important to study the statistics of the resolved field and for comparison with the acoustic scintillation result. Fifteen minute time averaged quantities are defined with an overbar and spatially averaged quantities along the y-axis or over the horizontal xy-plane are defined as $\langle\rangle_y$ as $\langle\rangle_{xy}$ respectively. The temporal averaging smooths out the 15 min data to look more like Gaussian distributions in the horizontal cross section. With high frequency 4-dimensional data, a 15 minute time average at all grid points is carried out first to obtain temporal mean quantities for the three dimensional flow field and plume temperature $(\overline{u}, \overline{v}, \overline{w}, \overline{\theta_p})$, where $\theta_p = \theta - \theta_{\mathrm{BKG}}$. The spatial average of vector quantities, however is evaluated where the vertical velocity is greater than a certain threshold, and the e-folding distance for Gaussian like distributions (i.e. $\overline{w} > \max(\overline{w})\exp(-1)$) is

chosen. The radius of a dissolved tracer concentration (like heat) is greater than that of the axial velocity because of dispersion and the ratio of proportionality is 1.2 (Papanicolaou and List 1987). This implies that scalar quantities have a wider Gaussian distribution and so its e-folding distance is $\exp(-1.44)$ (i.e. $\overline{\theta} > \max(\overline{\theta})\exp(-1.44)$, as previously used by Xu and DiIorio (2012)). Spatially varying turbulence quantities for the horizontal flows are then defined as $u' = \overline{u} - u_{\mathrm{BKG}}$, $v' = \overline{v} - v_{\mathrm{BKG}}$ since plume induced horizontal motions are of interest; spatial fluctuations for the vertical velocity and plume temperature, within the plume defined threshold regions, are defined as $w' = \overline{w} - \langle\overline{w}\rangle_{xy}$ and $\theta' = \overline{\theta}_p - \langle\overline{\theta}_p\rangle_{xy}$ respectively. When hourly data is presented in the vertical x-z plane, a three point average along the y direction centered at the origin is taken.

Following the method of Porte-Agel et al. (1998) and Sheng et al. (2000) the resolved-scale transport equation for kinetic energy and thermal variance can be obtained. The turbulent dissipation rates for kinetic energy (ϵ) and thermal variance (ϵ_θ) can then be approximated by computing the Reynolds averaged turbulent production from shear, $P = -\tau_{ij}S_{ij} = A_H S_H^2 + A_V S_V^2$, thermal gradients, $P_\theta = -\mathbf{q}\cdot\nabla\theta = \mathrm{Pr}^{-1}(A_H\Theta_H^2 + A_V\Theta_V^2)$, buoyancy, $B = K_V N^2 = \mathrm{Pr}^{-1}A_V N^2$, and from mean and turbulent transport of turbulent kinetic energy, $\partial/\partial z(\overline{w}q'^2)$, where $q'^2 = (u'^2 + v'^2 + w'^2)/2$, and from thermal variance, $\partial/\partial z(\overline{w}\theta'^2/2)$. Assuming steady state, $\partial/\partial z(\overline{w}q'^2) = P - B - \epsilon$ for TKE and $\partial/\partial z(\overline{w}\theta'^2/2) = P_\theta - \epsilon_\theta$ for temperature variance. From the 4-dimensional data, the dissipation values are then approximated

as,

$$\epsilon = \langle \overline{P} \rangle_{y,xy} - \langle \overline{B} \rangle_{y,xy} - \frac{\partial}{\partial z} \langle \overline{w} q'^2 \rangle_{y,xy} \tag{2.15}$$

$$\epsilon_\theta = \langle \overline{P}_\theta \rangle_{y,xy} - \frac{\partial}{\partial z} \langle \overline{w} \theta'^2 / 2 \rangle_{y,xy} \tag{2.16}$$

where the overbar represents a time average over 15 minutes and the angle brackets denote a spatial average using the thresholds described previously along either the y-axis (for $x - z$ profiles) or over the horizontal xy-plane (for vertical profiles and time series measurements at a given height), the latter being equivalent with the acoustic propagation measurements.

The right hand side of (2.15) represents the turbulent kinetic energy production by shear, the turbulent kinetic energy production by buoyancy (note $N^2 < 0$ within hydrothermal plumes and thus is a buoyancy production term and $N^2 > 0$ outside the plume thus represents a sink of TKE energy by buoyancy), and the mean and turbulent transport of TKE which will be a source when the term is negative implying that more TKE is being advected into the measurement area than is being taken away, resulting in a negative gradient. Similarly the right hand side of (2.16) represents the thermal variance production by thermal gradients and the mean and turbulent transport of thermal variance which will be a source term when negative, implying that more thermal variance is being advected into the measurement area than is being taken away, resulting in a negative gradient.

The refractive index fluctuations from both temperature variability and velocity fluctuations affect the acoustic forward scatter measurement and is quantified in terms of the dissipation rates of thermal variance and kinetic energy (DiIorio and Farmer 1998). The resulting structure parameters are defined as,

$$C_{n_\theta}^2 = 3.81 a_\theta^2 \epsilon_\theta \epsilon^{-1/3} \tag{2.17}$$

$$C_{n_v}^2 = \frac{1}{c_o^2} 1.97 \epsilon^{2/3} \tag{2.18}$$

$$C_{neff}^2 = C_{n_\theta}^2 + \frac{11}{6} C_{n_v}^2 \tag{2.19}$$

where $a_\theta = \frac{1}{c_o}\frac{\partial c}{\partial \theta} \sim 3.1 \times 10^{-3} (^\circ C)^{-1}$ is the fractional change in sound speed from temperature and $c_o = 1497$ m/s is the average sound speed. It is expected that the temperature contribution will dominate the effective refractive index fluctuations, as discussed by Xu and DiIorio (2011). However, the relative effects of each term to the effective refractive index fluctuations as defined by equation (2.19) will be quantified.

2.3 Model Results

The numerical convection model can be used to derive vertical volume transport and the entrainment of ambient fluid at each depth level over the full rise height of the plume (280 m) under different source conditions during a time when the horizontal cross flow is at a minimum and the plume is vertically upright. These measurements are needed to quantify the virtual source depth so that a comparison with observations can be made at 20 m above. Table 2.1 shows the different experiments

with varying heat transports (50 MW and 80 MW) and source areas at the plume coalescence height (3×3 m^2, 4×4.5 m^2, and 6×6 m^2), both needed to examine the effects of increasing the hydrothermal heat flux contribution on plume characteristics. Decreasing the source area while keeping the overall heat transport constant will result in more heat flux. These values have been chosen to examine the characteristics that could potentially represent the Dante plume (Xu and DiIorio 2011). The source area represents the physical region at which the individual venting locations on one chimney have coalesced into a single plume structure. Above this height, the plume behaves as if it had a single source with a virtual source of depth z_0.

The plume cross section at any given time from the turbulent convection model is never circular, instead it displays an irregular cross-sectional area throughout the plume rise height. Since the model output over the full rise height of the plume is once hourly, a representative cross section, as described by Lavelle et al. (2013), with a vertical velocity bound of $w > 0.03m/s$ (the minimum velocity to which the acoustic scintillation is sensitive) will be used. This representative cross sectional area (A) is generated using the number of computational cells N_{cells} that satisfy the vertical velocity bounding condition as well as the size of the horizontal computational cells: $A = \mathrm{dx\ dy}\ N_{cells}$. From this areal measurement, the effective radius, $R_{eff} = (A/\pi)^{1/2}$ is determined as a function of height. The plume perimeter is then defined as $S_{eff} = 2\pi R_{eff}$ and is calculated at each depth level during periods of minimum cross flow. The vertical volume transport is calculated from summing all

vertical velocities satisfying the bounding condition scaled by the cross sectional area of the grid cell: $W = \Sigma\ w$ dx dy. A linear fit for W can then be applied to estimate the virtual point source depth $z0$ for the plume (Lavelle et al. 2013) which has a strong linear relationship with height above the source. Utilizing W to determine virtual source is more reasonable than the radius, and is used here to determine the virtual source depths for each of the experimental runs in order to compare to observations obtained 20 m above. Table reftable:parameters lists the virtual point source depths for the experiments carried out and they range from 2173 to 2180 m.

In a one-dimensional integral model, a constant entrainment coefficient is typically used, but variations can exist as a function of height. The entrained horizontal flow that is radially oriented across the circumference of the plume boundary (at any single depth), which causes the plume to expand and increase its volume transport with height, is parameterized by the product of the axial vertical flow and the entrainment coefficient. Volume transport along the rise height of the plume is a good indicator of ambient fluid entrainment as the increased fluid volume inside the plume causes the effective radius to expand. To calculate the entrainment, a control volume, and Gauss' theorem is used to require the change in mass be equal to that entering into the sides of the representative circumference (Lavelle et al. 2013),

$$\frac{d}{dz}\int w\ \mathrm{dA} = \frac{dW}{dz} = \int \vec{u}\cdot\vec{n}\ \mathrm{ds} = \alpha_{eff} w_{max} S_{eff} \tag{2.20}$$

The velocity entrained on the outer perimeter is parameterized here in terms of the effective entrainment coefficient and the axial centerline maximum vertical velocity, i.e. $\vec{u} \cdot \vec{n} = \alpha_{eff} w_{max}$.

The entrainment coefficient is calculated from equation (2.20), and the results are shown in Figure 2.2, along with the volume transport W as a function of height for the experimental runs having different Smagorinsky coefficients in the horizontal and vertical directions (see Table 2.1). The hourly data were averaged across four different times when the background horizontal velocities were close to zero. This was done to minimize the effects of the cross flow so that the plume remains close to vertical. The effects of the cross flow on entrainment is reserved for another study. The results show that the entrainment coefficient is not very sensitive to the source conditions as all experimental runs overlap each other throughout the plume rise. Morton et al. (1956) carried out laboratory experiments to determine the entrainment coefficient, and they found an ideal value of 0.093, and proposed this as a useful average value. However, experiments on plumes for different discharge and/or environmental conditions do not support adopting a constant entrainment coefficient.

The model results show that near the source the entrainment coefficient can be as high as 0.25 and then exponentially decays over a 15 m rise height to a value centered about 0.03 which remains for the rest of the plume rise. The entrainment rate from previous plume modeling (Lavelle et al. 2013) showed that the entrainment was on the order of 0.1 near the source and decayed more slowly to 0.03 at a height of

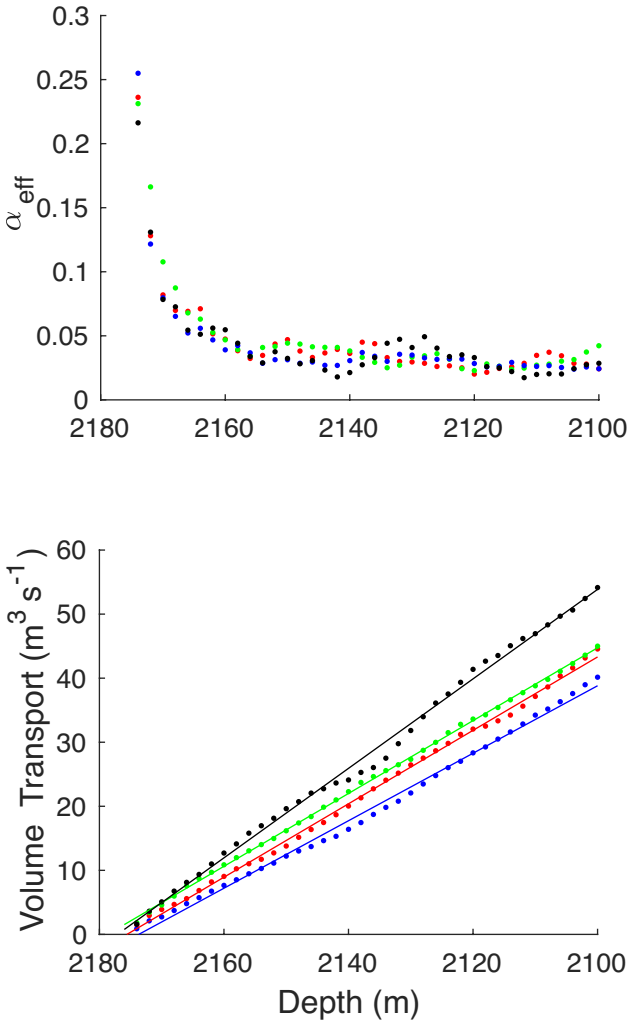

Figure 2.2: Axial plume characteristics for entrainment (top) and vertical volume transport (bottom) for experimental runs having different Smagorinsky coefficients in the horizontal and vertical directions (see Table 1). The virtual point source of the plume is taken at the x-intercept depth of the volume transport.

50 m from the source. This difference may be due to changes implemented with the vertical mixing calculation (which now makes use of a calculated Richardson number). As the turbulence decreases with height above the source it is expected that turbulent entrainment should also decrease. The high value near the source indicates that the vertical rise and the corresponding radius are not directly inverse quantities in this initial rise region. Matulka et al. (2014) presents measured entrainment coefficients showing considerable variability between .3 and 0.6 for variable buoyancy, quantified by the Atwood number (density difference across the interface between the plume and the ambient fluid, scaled by the sum of those densities).

Entrainment processes cause more ambient fluid to be incorporated into the plume, increasing both the radius and vertical volume transport. As source conditions change the volume transport also changes as a function of height as shown in Figure 2.2. As the source area increases (blue to red to green runs) or the heat transport increases (blue to black runs) the volume transport is increased. The plot of volume transport with depth is an important measurement because in Xu and DiIorio (2011), the acoustic measurements were taken at a height of 20 m above the vent chimney. The location of the vent chimney is assumed to be approximately where the virtual point source is located. By extrapolating the volume transport to zero, the corresponding virtual point source for the model is located at the x-intercept. The best fit for $z0$ for each separate run is then used to tune the height above the source from which the C^2_{neff} values are calculated for a better fit with observational data.

Observation and Model Comparisons

In order to validate the modeling results and explain the turbulent characteristics in the fully developed plume, we first compare model path averaged refractive index fluctuations (as calculated by C^2_{neff} in equation 2.19) and model vertical velocities to a time series of these same quantities measured at the Dante site in the Main Endeavour vent Field (Xu and DiIorio 2011). Figure 2.1 displays a time series through multiple tidal cycles of the path averaged vertical velocity and effective refractive index obtained via the acoustic scintillation method within the Dante plume. These observational data were taken at a height of 20 meters above the sulfide mound of Dante. (Xu and DiIorio 2011) showed that there is a relationship between periods of low turbulence and low vertical velocity when the horizontal cross flow is maximal, as more ambient water is entrained into the plume causing it to bend over and cool thus reducing its buoyancy (and thus vertical velocity), while also making the plume more like ambient conditions (with reduced turbulence). When the horizontal cross flow is minimal the plume is upright and the vertical velocity and turbulent properties are increased at 20 m above Dante. A comparison of model results with these observational results will improve confidence in the model's ability to simulate realistic situations. When the turbulent convection model approximates the observed experimental results, the model can then be used to examine physical quantities of interest that are difficult or impractical to obtain through field observation.

Figure 2.3 compares the results of several model runs to see changes in the turbulent effective refractive index (Equation (2.19)) and spatially averaged vertical velocity at 20 m above the virtual source depth, listed in Table 2.1, as a function of source conditions (heat transport, area) and as a function of the vertical Smagorinsky coefficient. The spatial averaging for these results are taken over the cross section and is intended to duplicate the path averaged measurements that is obtained with the acoustic scintillation system (see Figure 2.1). Each subplot on the left can be interpreted as the level of turbulence as a function of time. The model output is over a 24 hour period and takes into account two tidal cycles shown as dotted curves on the top panels. All of the model results display similar behaviors: there are higher levels of turbulence during times of slack ambient currents and there are lower levels of turbulence during times of maximum cross flows; the vertical velocity is maximal at slack water and minimal at maximum cross flows, both consistent with the observational measurements. Also it can be seen that the parameter values for each run all have an affect on the turbulent levels and vertical velocity: increasing the heat transport from 50 to 80 MW (with a constant area) causes an increase in turbulence levels and vertical velocity only when the cross flow is maximum; increasing the cross sectional area (with a constant heat transport of 50 MW) decreases the turbulence levels and vertical velocity particularly during slack water. The greater vertical Smagorinsky coefficient gives much higher turbulence levels than is observed and increases the vertical velocity substantially from the other runs but there is also no well defined tidal cycle presumably because the mixing erodes this characteristic.

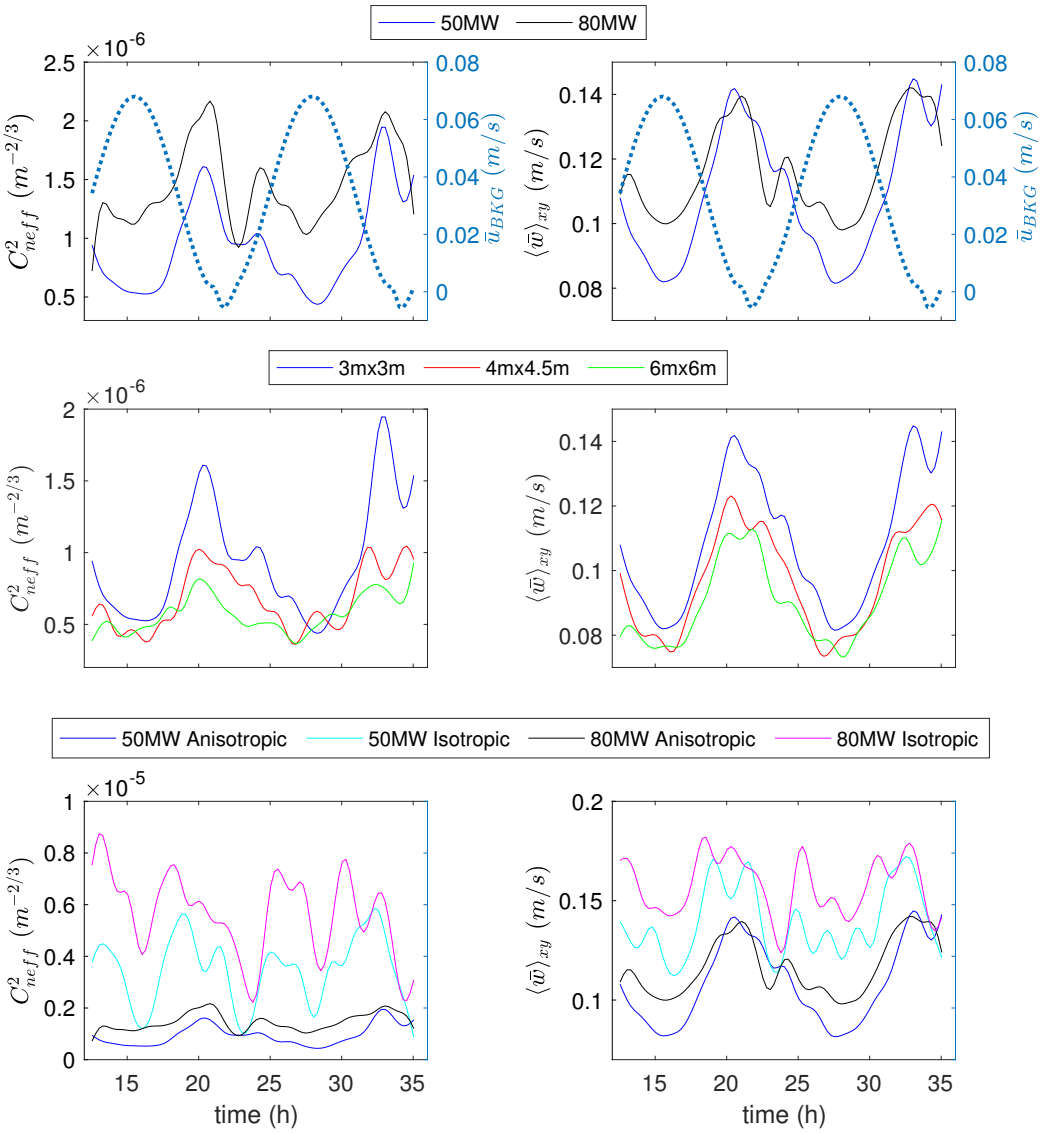

Figure 2.3: Time series of the spatially and temporally averaged refractive index structure parameter (left), and vertical velocity (right) for each model run grouped by different heat transports (top), discharge areas (middle) and vertical Smagorinsky coefficients (bottom). Simulation measurements are taken at 20 m above the virtual point source $z0$ identified in Table 2.1. The horizontal current used in the model is shown as a dotted curve on the top plots.

Comparing each of these model results to the observational results in Figure 2.1, the closest run that gives a good match is Exp 1 (red) with a heat transport of 50 MW over an area of 4×4.5 m^2. The details of this experimental run is then explored to quantify in more detail the turbulent characteristics that leads to the refractive index fluctuation measurement.

Turbulence quantities

The main change implemented in the model is using a variable Richardson number as a factor in the vertical mixing coefficient instead of a constant ratio of Ri/Pr=0.167. This allows for the changing relationship between shear and stratification to affect the vertical mixing and serves as a measure of how stable or unstable the plume is; an unstable Richardson number (Ri < 0.25) indicates a system that is prone to fluid overturns and results in turbulent behaviors. Previously the model used $(1 - \text{Ri/Pr})^{1/2} = 0.91$ to scale the vertical mixing; now this term varies from $0.89 < (1 - \text{Ri/Pr})^{1/2} < 1.03$ for a constant Pr=3 and a Richardson number range of $-0.2 < \text{Ri} < 0.6$ (as will be shown). This will cause a small increase in the vertical mixing throughout the plume; a Pr=1 would alter the vertical mixing by $0.63 - 1.10$ and a Pr=6 reduces the range to $0.95 - 1.02$. Regardless, the intent is to show how the Richardson number varies throughout the plume and its surrounding. If Ri ≥ 3 then $A_V = A_{Vmin}$ in order to keep the vertical mixing a real number.

Figure 2.4 is a plot of the calculated Richardson number during a time when the cross flow was zero (left side) and when it was maximal (right side). There are

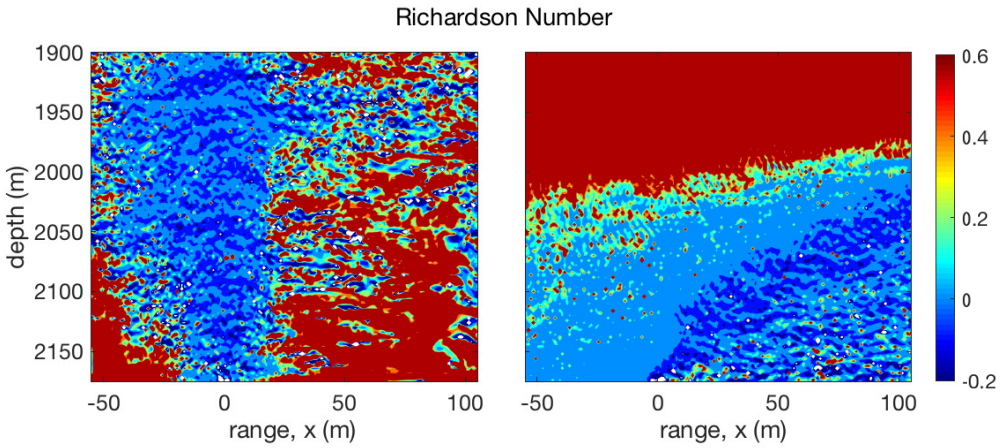

Figure 2.4: A vertical cross section of the Richardson number (Ri) taken on the plane $y = 0$ for model Exp 1, when the horizontal crossflow was slack (left) and when it was maximal (right). Measurements are averaged along the y-axis over three grid cells centered on $y = 0$.

three distinct regions displaying different Richardson number behavior: the interior of the plume, the edge of the plume, and the background ambient water. The interior of the plume (for a vent source centered at the origin on the x-axis) contains the most unstable Richardson number values. The Ri values consistently fall near zero (light blue) with much of it negative (dark blue). Negative Ri numbers indicate the presence of low density fluid beneath higher density fluid, which will enhance the vertical eddy mixing at those locations as the unstable stratification will contribute to fluid overturns and eddy formations. When there is a high background crossflow, the plume is bent and the negative Richardson numbers are distributed throughout the downstream region. These low and negative Richardson numbers indicate that within the plume, shear and buoyancy dominate, and the resulting flow will be

highly turbulent. This high degree of variability indicates that the Richardson number cannot be taken as a constant for realistic plume dynamics.

The plume edge can be seen to have more stable Richardson numbers than those observed in the interior but still displays a degree of instability. During a time of low background crossflow, both sides of the plume edge can be seen to contain packets of eddies that have Richardsons numbers that are either stable (> 0.25 red), at stability (≈ 0.25 green) or unstable (< 0.25 blue tones). These turbulent eddies forming on the edge of the plume are presumably formed because of turbulent entrainment.

Outside the plume within the ambient waters, the Richardson number maintains a constant and stable value above 0.4 (red) for both flow conditions. This indicates that the ambient fluid is very stable because of the realistic stratification that is used in the model which doesn't experience turnover or strong shear turnovers. However, during the large crossflow period, when the plume is bent over, the upstream region changes markedly - the magnitudes of the Richardson numbers are more layered, displaying a band of near stability (0.25, green) on the farthest upstream side of the plume and a broader band close to zero (light blue) along the upstream side of the plume. This behavior is reasonable, as the crossflow increases the shear which causes mixing and decreases the stratification.

The anisotropic eddy viscosity coefficients, as described in equations 2.7 and 2.8, are shown in Figure 2.5 during a time of no cross flow (left) and during a time of maximum cross flow (right) (eddy viscosities A and diffusivities K differ only by a

factor of Pr=3 and hence are not shown). Background levels starting at $10^{-3.3}$ and $10^{-4.3}$ m^2/s for horizontal and vertical mixing respectively are shown as white. The eddy viscosity values show a clear drop off along the axis of the plume with height, with near source values regularly reaching orders of $10^{-2.5}$ m^2/s for the horizontal mixing and $10^{-3.3}$ m^2/s for the vertical mixing. In the far reaches of the plume, the mixing is reduced to orders of 10^{-3} m^2/s and 10^{-4} m^2/s respectively, but many eddies with higher mixing values still exist. The horizontal mixing is always greater than the vertical mixing, as it is less difficult to induce mixing within the same vertical layer than it is to mix different vertical layers. Also the axial variation is less than one order of magnitude in the horizontal and greater than one order of magnitude in the vertical. Under maximum cross flow conditions, the horizontal mixing in the interior of the plume retains similar magnitudes with that of no cross flow, albeit with significant plume bending downstream. In addition, while bent over, there is enhanced horizontal mixing outside the plume region presumably because of increased horizontal shear strain rates quantified by equation (2.10). Vertical mixing outside the plume while bent over is enhanced over a greater vertical cross sectional area than is horizontal mixing and also follows the instability region of the Richardson number in this area: as the Richardson number decreases the mixing increases. The vertical mixing is dominated by the vertical shear strain rate quantified by equation (2.12) and it is expected that this will have the greatest variability while bent downstream.

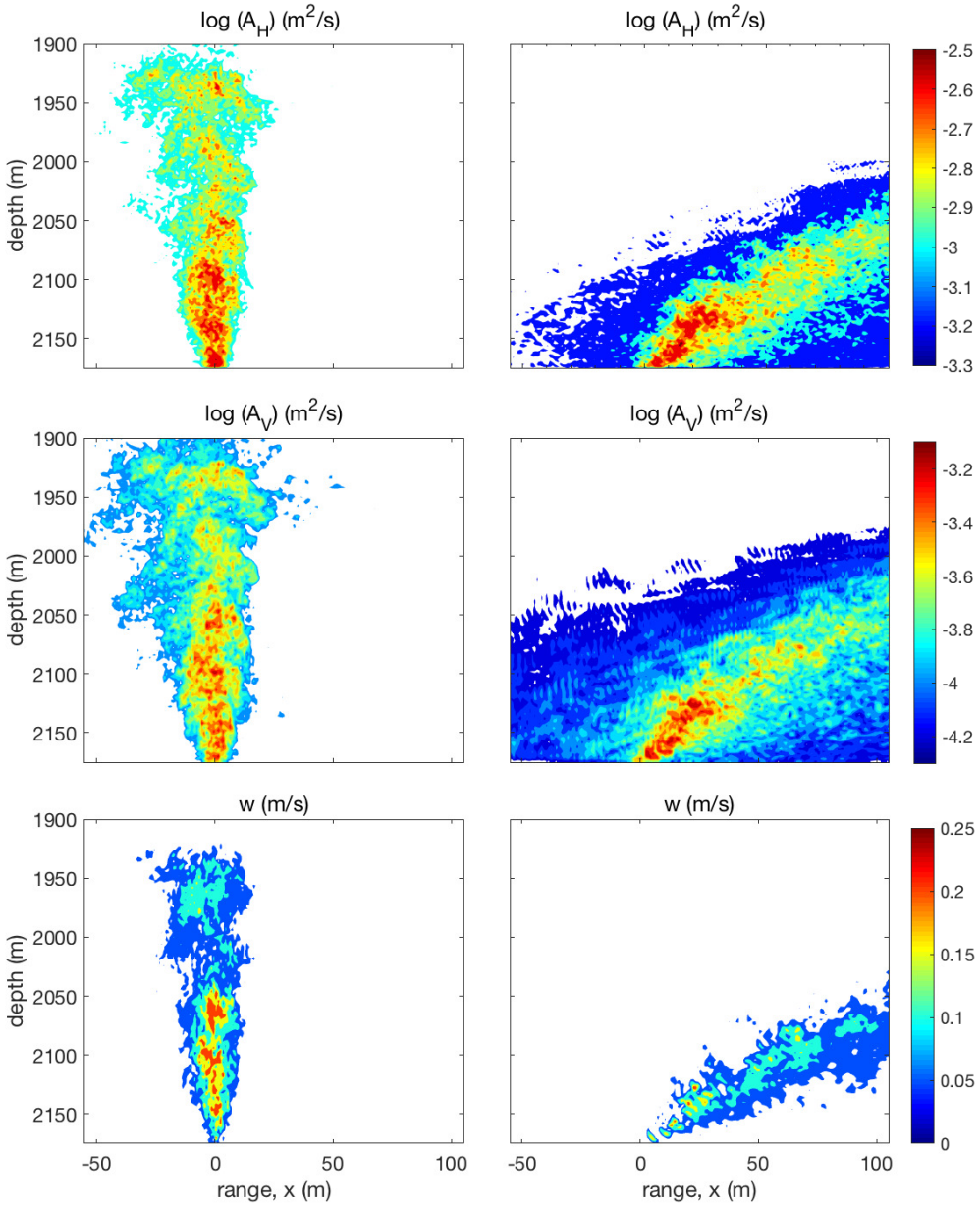

Figure 2.5: A cross sectional view of the eddy viscosity coefficients (A_H, A_V) and vertical velocity (w) taken on the plane $y = 0$ for Exp 1, when the horizontal crossflow is slack (left) and when it is maximal (right). Measurements are averaged along the y-axis over three grid cells centered at $y = 0$.

The other main influence on the mixing is the chosen Smagorinsky coefficients. For all experiments, except Exp 4 and 6, the parameters, $C_{SH}\ell_{SH} \sim 0.17$ and $C_{SV}\ell_{SV} \sim 0.08$ are kept the same as in Lavelle et al. (2013). A constant Smagorinsky coefficient of $C_{SH} = C_{SV} = 0.14$ was also tested to force vertical mixing greater than horizontal mixing (as $C_{SH}\ell_{SH} \sim 0.17$ and $C_{SV}\ell_{SV} \sim 0.28$) and as shown in Figure 2.3, it creates too much mixing because the tidal characteristics of the plume are lost (magenta and cyan curves). Hence the model is very sensitive to the chosen vertical Smagorinsky coefficient. To force near isotropic mixing $A_H \sim A_V$, the vertical Smagorinsky coefficient should need to be set to $C_{SV} \sim 0.085$ for the current model grid. Typically (C_S) for geophysical flows can vary from 0.1 to 0.2 (Sagaut and Meneveau 2006) when considering isotropic mixing values.

Figure 2.5 (lower panels) also shows the vertical velocity in the plume under low (left) and high (right) cross flow conditions. During the period of no horizontal cross flow, there are large vertical velocities through the first 125 m of rise height with magnitudes as large as 0.2 m/s. Over this section of the rise, there is a widening of the plume due to entrainment and increased vertical transport. After 150 m or so, the vertical velocity drops to 0.1 m/s. Under periods of maximum crossflow, there is a strong loss of both rise height and magnitude of vertical velocity brought about by more mixing. Larger velocities are only observed near the source, and plume height is limited to 125 m of rise compared to the 250 m rise during low cross flow. The crossflow induces more entrainment, enhancing mixing and quickly lowering the temperature of the fluid. This results in a lower buoyant force, limiting the rise

height. In addition, by the time a packet achieves the zone of neutral buoyancy, it will be advected horizontally a considerable distance from the source by the cross flow.

From the high frequency data output, 15 minute averages are computed of the vertical velocity field and then the region for spatial averaging using the thresholds described previously are determined. Figure 2.6 shows a vertical cross section of the vertical velocity and plume temperatures during a time of weak and strong crossflows each with their different threshold limits. These plots give a good representation of where the main axis of the plume is. It should be noted that the origin of the source during the cross flow is advected downstream compared to when there is no cross flow. The vertical velocity changes the most during the cross flow with significantly reduced flows throughout the plume because of enhanced entrainment (Devenish et al. 2010).

Turbulent kinetic energy

From the mixing parameters (A_H, A_V), shear strain rates (S_H^2, S_V^2), stratification (N^2), and mean and turbulent transport ($\overline{w}q'^2$), the TKE production from shear, TKE production and dissipation from buoyancy, and the effect of mean and turbulent transport of TKE are calculated. Figure 2.7 shows the vertical cross section of these TKE rates averaged along the y-axis using the spatial averaging threshold described previously. Plots are shown during a time of minimum crossflow (left) and maximum crossflow (right). The shear production, during times of

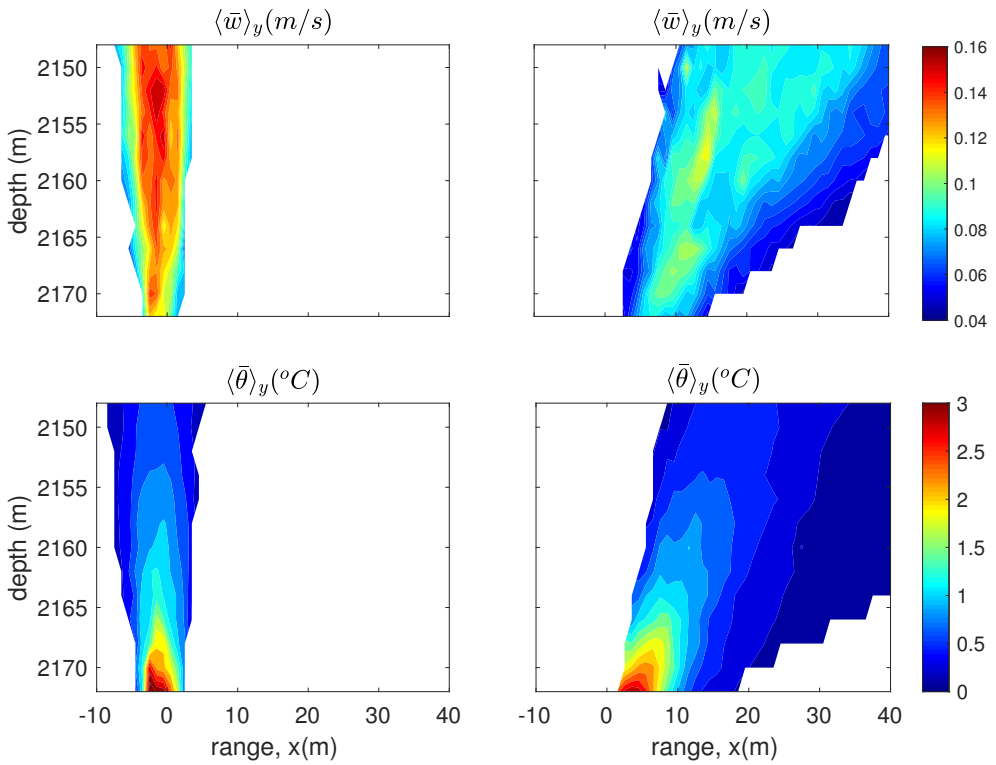

Figure 2.6: A cross sectional view of the 15 minute averaged vertical velocity (top) and plume temperature (bottom) spatially averaged along the y-axis during a time of no cross flow (left) and maximum crossflow (right) for Exp 1. Data above the spatial averaging threshold of $\exp(-1)$ for velocity and $\exp(-1.44)$ for temperature are shown.

minimum crossflow has vertical attenuation along the axis of the plume, with on-axis magnitudes of $10^{-4.5}\mathrm{m}^2/\mathrm{s}^3$ throughout the near source rise height. There is horizontal attenuation over the small off-axis distance and off-axis magnitudes drop to $10^{-5}\mathrm{m}^2/\mathrm{s}^3$ on the e-folding edge of the plume. These values are dominated by the horizontal shear strain rate. During times of maximum horizontal cross flow, there is a large degree of plume widening, shear production magnitudes are maximal along the upstream side of the plume where the vertical shear strain rates are maximal and production magnitudes decrease in the downstream direction to values as low as $10^{-5.5}\mathrm{m}^2/\mathrm{s}^3$. During this time it should be noted that the maximum production does not occur along the main axis of the plume (compare Figure 2.6 with Figure 2.7) but rather where the velocity gradients are maximal on the upstream edge of the plume.

Buoyancy can be either a source (< 0) or a sink (> 0) of turbulent kinetic energy depending on whether work is done with or against gravity respectively. The buoyant production represents the contribution to TKE from a buoyantly unstable system when $N^2 < 0$. During minimum crossflow, buoyancy production is confined to the center of the plume; on the fringes of the plume buoyancy dissipation acts as a sink of TKE (not shown). Near the source, production reaches $10^{-7}\mathrm{m}^2/\mathrm{s}^3$, but this rapidly decreases further from the source. At times of maximum crossflow, the buoyant production is confined to the upstream side of the plume and buoyant dissipation (in gray color scale) to the downstream side. Production of TKE occurs because while the plume is bent over, upstream areas correspond to unstable stratification ($N^2 < 0$) because the isotherms are tilted (see Figure 2.6); in the

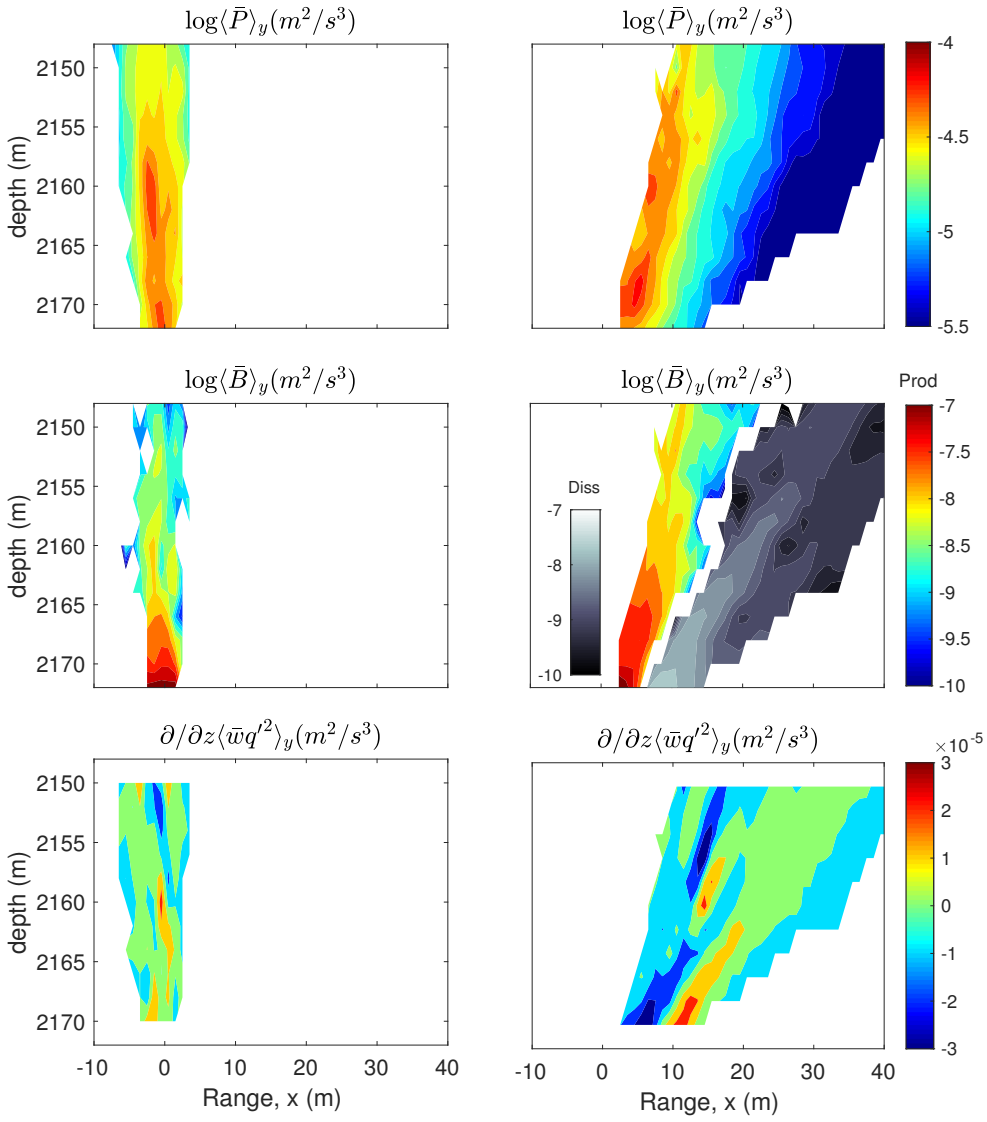

Figure 2.7: A cross sectional view of the turbulent kinetic energy production by shear, $\langle\overline{P}\rangle_y$, buoyancy production (jet colormap) and dissipation (gray colormap), $\langle\overline{B}\rangle_y$, and the mean and turbulent transport of TKE, $\partial/\partial z\langle\overline{w}q'^2\rangle_y$, spatially averaged along the y-direction for Exp 1, when the horizontal crossflow is slack (left) and when it is maximal (right).

downstream direction the buoyant plume becomes stable ($N^2 > 0$) and hence there is dissipation of TKE. The white area separating buoyant production and dissipation is the main axis of the plume and shows how it is tilted downstream. In both flow regimes, the shear production dominates over the buoyant production and dissipation and hence the buoyant contribution to the total kinetic energy is negligible.

Turbulent kinetic energy can also be vertically transported through the plume by the mean and turbulent velocities ($\overline{w} = \langle \overline{w} \rangle_{xy} + w'$). At any given depth level, if there is more TKE transported upward from below and less transported upward from above, then this will act as a source of TKE at that level; if there is more TKE transported upward from above than is transported upward from below then this will act as a sink of TKE at that level. For a hydrothermal plume, deeper depths will generally have higher vertical velocities and contain more TKE. However as can be seen in Figure 2.6, the vertical velocity actually increases away from the source when the cross flow is minimal causing the mean and turbulent transport of TKE to increase with height away from the source; when the cross flow is maximal the mean and turbulent transport of TKE decreases with height above the source (see Figure 2.8, top panels). In terms of production or dissipation of TKE it is the gradient that is important and is shown in Figure 2.7; a negative value corresponds to a source, while a positive value corresponds to a sink. The gradient taken over 4 m depth results in values that are much more variable throughout the plume with sources and sinks varying between $\pm 2 \times 10^{-5} m^2/s^3$ showing much patchiness.

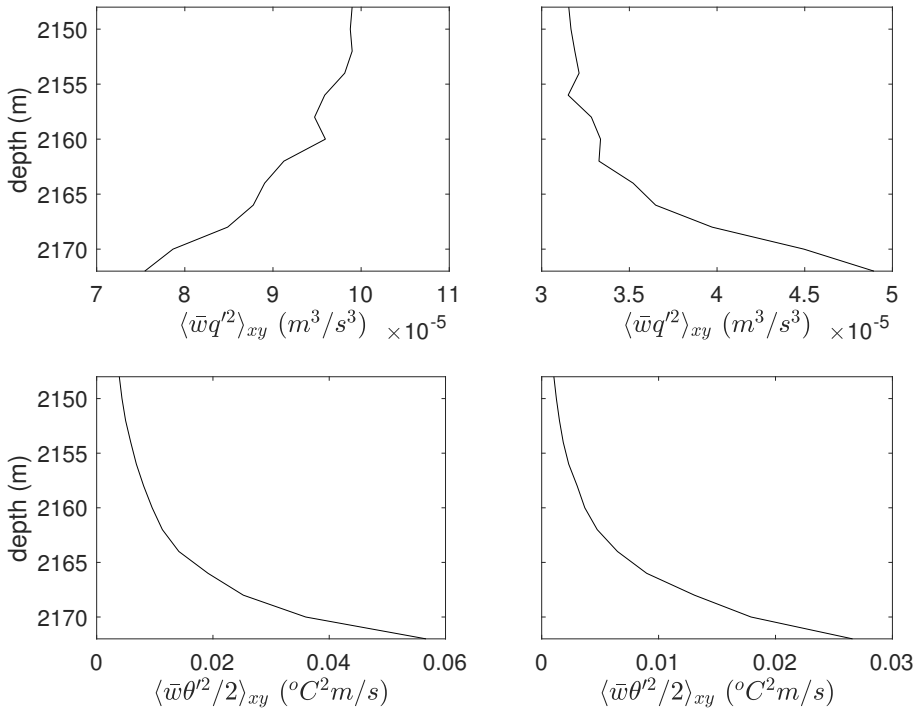

Figure 2.8: Depth dependence of the mean and turbulent transport of turbulent kinetic energy, $\langle \overline{w}q'^2 \rangle_{xy}$ (top), and thermal variance, $\langle \overline{w}\theta'^2 \rangle_{xy}$ (bottom), spatially averaged on the x-y plane, when the horizontal crossflow is slack (left) and when it is maximal (right) for Exp 1.

To examine the temporal variations of the sources and sinks of TKE, measurements are focused at 20 m above the virtual point source and for Exp 1 this corresponds to a depth of 2156 m (see Table 2.1). From Figure 2.7 averaging over the x-axis then shows the temporal variations in Figure 2.9 as dots; the solid line is a two-hour lowpass filter of the data. Buoyancy is negative and corresponds to a source of TKE when averaged over the plume cross section. During maximum flow at 15 and 27 h the buoyancy source is reduced and during slack water at 22 and 34 h the buoyancy source is maximal reaching values -2×10^{-9} m^2/s^3. However the magnitude is much less than the production by shear. The shear production term also shows strong tidal cycle variations with values ranging from 1 to $3{\times}10^{-5}$ m^2/s^3 with maximal values during slack water when the plume is upright, and is the dominate source of TKE. The mean and turbulent transport of TKE shows no discernible tidal cycle and values oscillate about zero. From equation 2.15 the TKE dissipation rate is evaluated at 20 m above the virtual source assuming this steady state balance. In general the dissipation is balanced by the shear production and any small gains or losses by the mean and turbulent transport term are also dissipated.

Thermal variance

From the mixing parameters (K_H, K_V), square of the thermal gradients (Θ_H^2, Θ_V^2), and the mean and turbulent transport ($\overline{w}\theta'^2$), the sources and sinks of thermal variance are computed. Figure 2.10 shows the vertical cross section of the rates of production of thermal variance. Plots are shown during a time of minimum crossflow

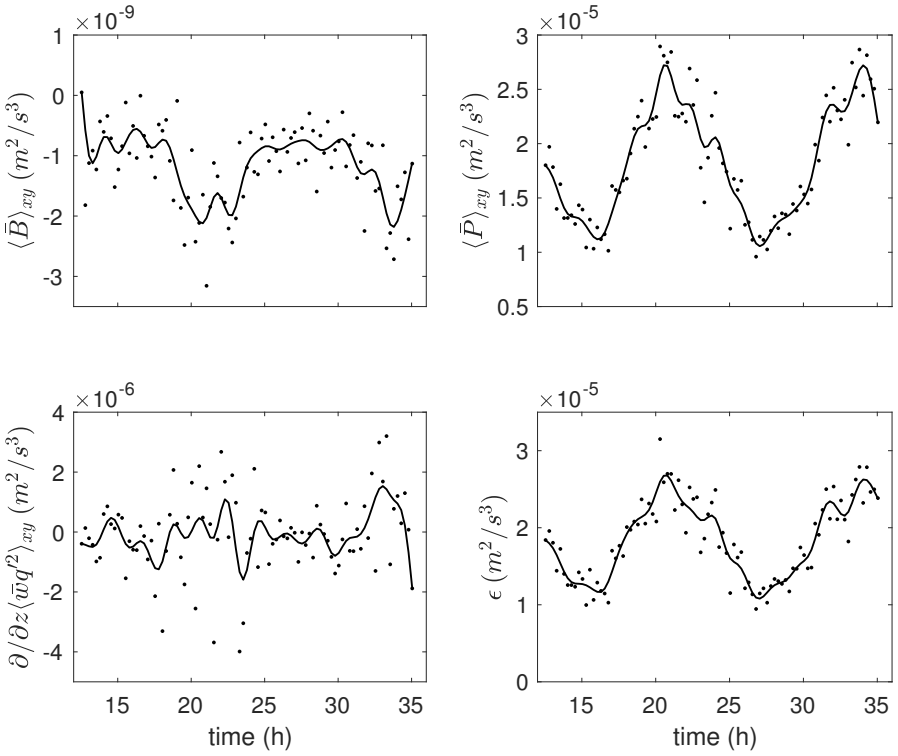

Figure 2.9: Spatially and temporally averaged measurements of the turbulent kinetic energy buoyancy production, shear production, mean and turbulent transport of TKE, and the resulting dissipation rate (ϵ), all taken at 20m above the theoretical point source of $z0 = 2176$ m. Results are for Exp 1.

(left) and maximum crossflow (right). The heat flux production, during times of minimum crossflow has a strong vertical attenuation along the axis of the plume, with axial magnitudes ranging from 10^{-3} to 10^{-4} $^{o}C^{2}/s$. There is strong horizontal attenuation over the off-axis distance and off-axis magnitudes drop to 10^{-4} $^{o}C^{2}/s$ on the exp(-1.44) edge of the plume. These values are dominated by both the horizontal and vertical thermal gradients as can be seen in Figure 2.6. During times of maximum horizontal cross flow, the production of thermal variance is spread out over the down stream direction to values as low as 10^{-6} $^{o}C^{2}/s$. During this time it should be noted that the maximum production also does not occur along the main axis of the plume (compare Figure 2.6 with Figure 2.10) but rather where the thermal gradients are maximal on the upstream edge of the plume.

Thermal variance can also be vertically advected through the plume by the mean and turbulent velocities. It is expected that deeper depths will generally have higher thermal variance and this will be advected by the mean and turbulent vertical velocity. Figure 2.8 (bottom panels) show that the horizontally averaged values decrease with height above the source. The gradient along the plume is always negative indicating that this term acts as a source of thermal variance when averaged over the cross section. The gradient is taken over 4 m depth and Figure 2.10 shows that it is mostly negative throughout the plume vertical cross section which corresponds to a source of thermal variance production. Only during the maximum cross flow does the mean and turbulent transport term give positive values on the

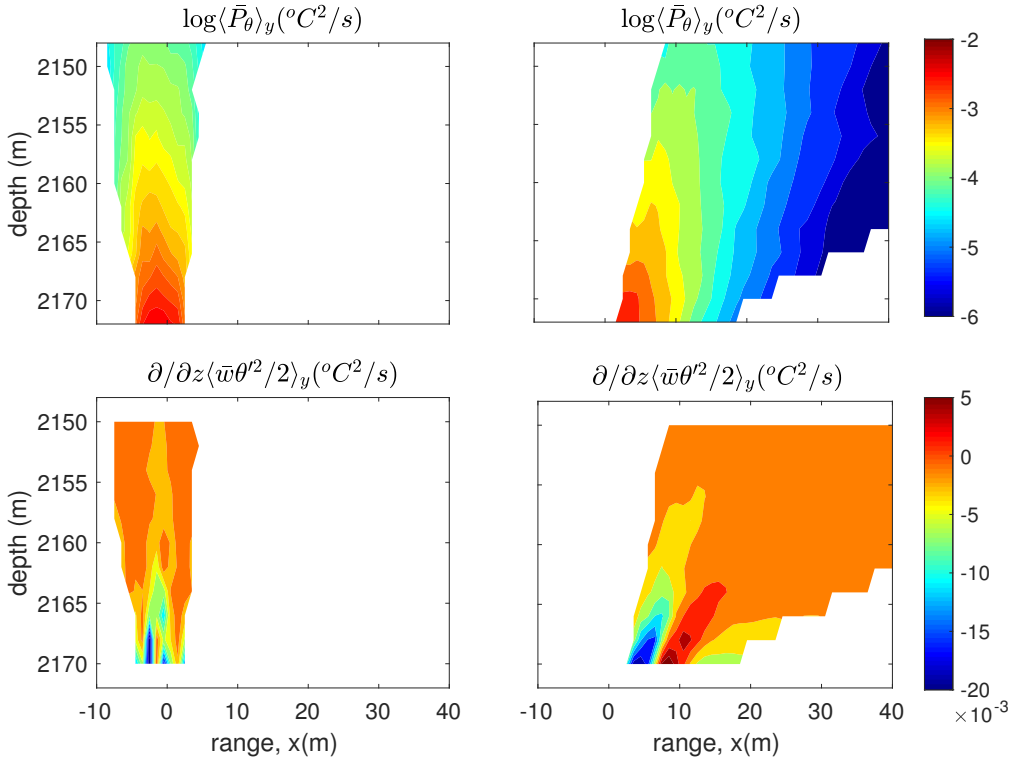

Figure 2.10: A cross sectional view of the thermal variance production by heat fluxes acting on temperature gradients, $\langle\overline{P_\theta}\rangle_y$ (top), and the mean and turbulent transport of thermal variance, $\partial/\partial z\langle\overline{w}\theta'^2\rangle_y$ (bottom), spatially averaged along the y-direction for Exp 1, when the horizontal crossflow is slack (left) and when it is maximal (right).

downstream side of the source which is mirrored by strong negative values on the upstream side of the plume axis.

The temporal variations of the sources and sinks of thermal variance at 20 m above the virtual source, obtained by averaging the quantities in Figure 2.10 over the x-axis at the depth of 2156 m, is shown in Figure 2.11; as before the solid line is a two-hour lowpass filter of the 15 min result. The heat flux production term shows strong tidal cycle variations with values ranging from 0.5 to 2×10^{-4} $^{o}C^{2}/s$ with maximal values during slack water when the plume is upright. The mean and turbulent transport of thermal variance also shows tidally varying values ranging from -0.6 to -0.2×10^{-3} $^{o}C^{2}/s$ and is an order of magnitude larger than the production by heat fluxes acting on the thermal gradients. From equation 2.16 the thermal dissipation rate at 20 m above the virtual source is balanced by the mean and turbulent transport of thermal variance and any small modulations by the heat flux production term is assumed to be dissipated.

Refractive index fluctuations

One of goals of this paper is to find an experimental run that best fits with observations of turbulent refractive index fluctuations that were made with an acoustic scintillation flow meter as shown in Figure 2.1. Equation (2.19) quantifies the level of the effective refractive index in terms of both temperature fluctuations and velocity fluctuations, which are not easily accessible via experimental means as they rely on the dissipation rates of TKE and thermal variance (see Equations (2.17)

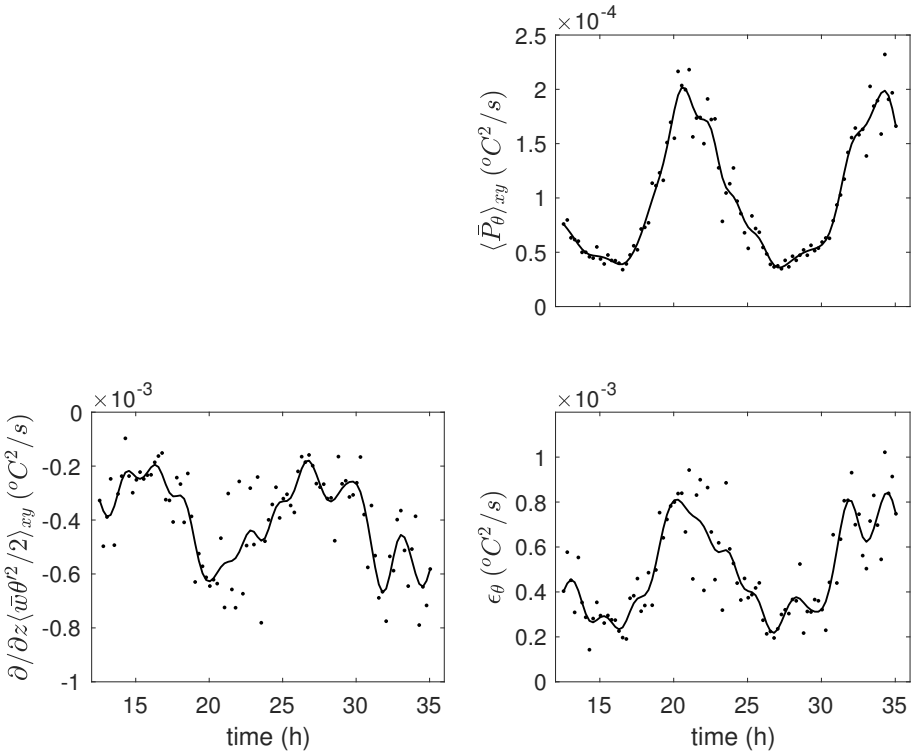

Figure 2.11: Spatially and temporally averaged measurements of the turbulent thermal variance production by heat fluxes, mean and turbulent transport of thermal variance, and the resulting dissipation rate (ϵ_θ), all taken at 20m above the theoretical point source of $z0 = 2176$ m. Results are for Exp 1.

and (2.18)). The large eddy simulation of a hydrothermal plume in a realistic deep sea environment with an ambient cross flow and stratification that has been developed is ideally suited to document these turbulent characteristics as previously discussed. Figure 2.12 shows that the thermal component of the refractive index fluctuations dominates over the turbulent velocity effects by three orders of magnitude and this is because the thermal dissipation rate is two orders of magnitude greater than the dissipation rate of TKE. This confirms that the major contribution to acoustic forward scatter is temperature fluctuations as previously suggested by Xu and DiIorio (2011). Because the turbulence quantities are all dependent on the cross flow, the refractive index structure parameters also show tidal oscillations in accordance to the data analyzed at the Dante plume. By calculating C^2_{neff} in terms of its contributing energy dissipation rates, ϵ and ϵ_θ, as a function of plume source conditions and model parameters, a comparison to experimental measurements as previously shown in Figure 2.3 can be made.

The other parameter obtained by the acoustic scintillation is the path averaged vertical velocity. In choosing Exp 1 the speed of the horizontally averaged vertical velocity approaches a maximum speed of 0.12 m/s which is consistent with the initial measurements made with the acoustic scintillation system. However higher values exceeding 0.2 m/s are observed later in time (see Figure 2.1) but without a concomitant increase in turbulence levels. This modeling study shows that by changing the source conditions and/or the vertical Smagorinsky coefficient, an increase in vertical velocity is also associated with an increase in turbulence

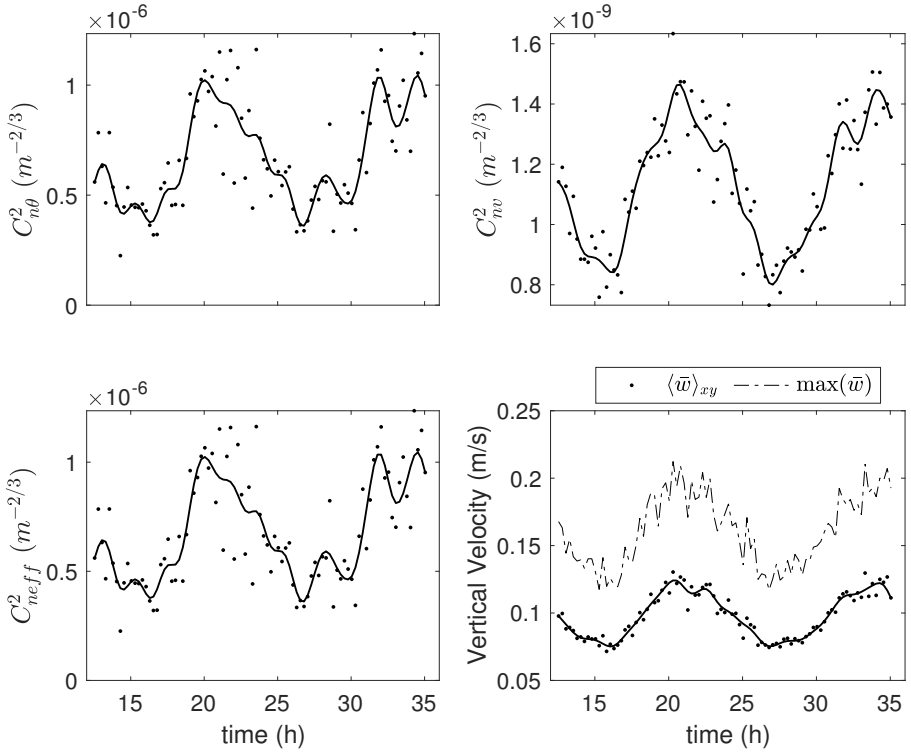

Figure 2.12: The refractive index structure parameter determined from temperature variability, $C^2_{n\theta}$, (Equation (2.17)) is compared to that determined from turbulent velocity, C^2_{nv}, (Equation (2.18)). The effective refractive index structure parameter, C^2_{neff}, (Equation (2.19)) is compared to observed measurements shown in Figure 1. The spatially and temporally averaged vertical velocity is compared to the maximum vertical velocity (dashed line).

quantities. Without averaging, the maximum temporally averaged vertical velocity at 20 m above the virtual source does in fact show speeds approaching these high vertical velocities indicating that the model results are very sensitive to the spatial averaging approach taken. Nevertheless, Exp 1 is a good compromise and comparison to the observational quantities.

Figure 2.13 shows the comparison between the modeled plume characteristics and a canonical average of the acoustic scintillation data measured by Xu and Di Iorio (2012) from the start of September 24th to October 1st at 8:00AM. During times of high background cross flow, the modeled refractive index approaches the canonical mean. As cross flow decreases, the modeled magnitude increases, generally falling within two standard deviations of the canonical mean. Modeled average vertical velocity falls within one standard deviation of the mean. Both quantities obtained from the model output are sensitive to the averaging method used.

2.4 Summary and Conclusions

This research documents for the first time the dissipation quantities for turbulent kinetic energy (TKE) and thermal variance of a hydrothermal vent plume in a stratified, tidally varying cross flow using a large eddy turbulent convective model. Sources and sinks of TKE and thermal variance are quantified and discussed, and assuming steady state for the turbulent budget equations, the dissipation values are calculated. The advantage of the model is that these quantities are almost impossible to measure in a deep sea hydrothermal vent environment. Model results

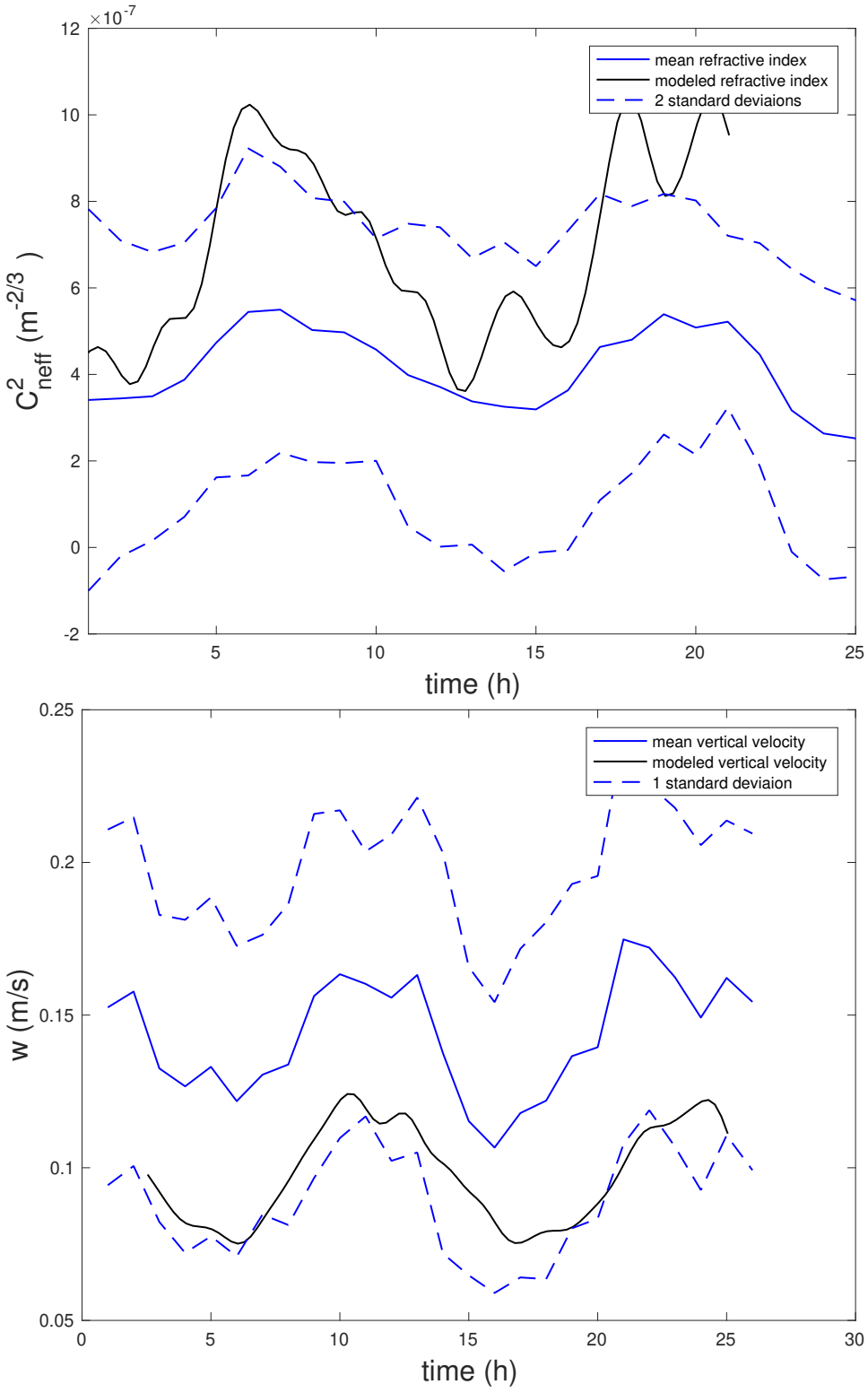

Figure 2.13: Mean values of refractive index and vertical velocity taken from the canonical average of acoustic scintillation data taken from Xu and Di Iorio (2012) over a 7 day time period from September 24 to October 1 is shown in solid blue. Modeled refractive index and vertical velocity from experiment 1 is shown in black.

and field observations of refractive index fluctuations and vertical velocity made with a novel acoustic scintillation flow meter together point to a best set of model parameters. A number of model experiments, having different source conditions (heat transport and area) with differing Smagorinsky coefficients in the vertical, was carried out for comparison to observed refractive index fluctuations and vertical velocity obtained at 20 m above the Dante sulfide structure in the Main Endeavour vent field. It was found that a heat transport of 50 MW over an area of 4×4.5 m^2 with Smagorinsky coefficients modified to include Ri dependence give the best comparison between model and observations. This is consistent with the 43 MW of heat transport obtained by Xu and DiIorio (2012) using a 1D integral model.

The horizontal and vertical eddy viscosities parameterized with their respective shear strain rates show maximum values within the first 100 m of rise presumably where the shear is maximal, and they diminish with distance away from the source but still retain packets of high mixing values dispersed within the plume. It was found that the Richardson number used to quantify the vertical mixing is most effective on the upstream side of the plume when bent over by the cross flow which causes stable stratification and hence reduced mixing values. The eddy viscosity values obtained by Gao et al. (2019) for their large eddy simulations with a heat flux of 0.5 ^{o}K m/s show maximal values within the central portion of the plume with values as high as 0.03m^2/s when averaged over the plume. The 50 MW experiment corresponds to a heat flux source of approximately 0.7 ^{o}K m/s which results in much smaller vertical and horizontal mixing values (2×10^{-3} m^2/s and

2×10^{-4} m^2/s respectively), the difference is presumably in the parameterization scheme used (Prandtl-Kolmogorov which depends on the turbulent kinetic energy whereas the model described here uses an anisotropic mixing, Smagorinsky parameterization that depends on the horizontal and vertical shear strain rates and different coefficients for the horizontal and vertical directions).

The inclusion of mean and turbulent transport increases the dissipation rate of thermal variance in a significant way, from 2×10^{-4} ^{o}C^2/s when just considering the heat fluxes from thermal gradients to 8×10^{-4} ^{o}C^2/s when balancing this advective effect. These high thermal variance production terms, dominate the effective refractive index fluctuations parameterized by the thermal structure function $C^2_{n\theta}$, thus confirming its dominant contribution to acoustic forward scatter.

For dissipation of TKE it was found that buoyancy production was negligible as a source or sink, being three orders of magnitude smaller than the production by shear, which is a surprising result given the unstable nature of the hydrothermal vent plume. Mean and turbulent transport contributions modulate the TKE balnce in a small way but could have the potential to reach magnitudes comparable to the shear production in some regions of the plume.

2.5 Acknowledgements

This work was partially supported under the NSF CAREER grant OCE0449578 and the NSF OTIC grant OCE1334124. We gratefully acknowledge J. W. Lavelle for valuable comments and for providing the original underlying code (Lavelle et al.

2013) which we modifed as described herein. The authors would also like to thank Guangyu Xu for also providing valuable input on the manuscript.

CHAPTER 3

INFLUENCE OF SOURCE CONDITIONS ON PLUME CHARACTERISTICS

3.1 Introduction

In Chapter 2, we examined the turbulent characteristics of a single hydrothermal vent plume representative of the black smoker at Dante within the Main Endeavour vent field. The model run for experiment 1 was chosen for detailed studies of the turbulent characteristics as the vertical velocity and refractive index fluctuations showed a reasonably good comparison with observations. Here we will examine detailed effects of source conditions (heat transport, source area, and differing vertical Smagorinsky coefficients) on the turbulent characteristics of the plume for the six experimental runs shown in Table 2.1. Experiment 3 will serve as a baseline for each initial condition comparison. The equations and methodology for the modeling experiment and method of analysis is laid out in the methods section of the Chapter 2 paper, and the analysis of model output is consistent with the analysis described in depth in that chapter.

Many vents have different source conditions: both heat output and chimney size can vary widely from plume to plume. It is important to understand how these conditions influence the hydrothermal vent plume characteristics, as these affect how the hydrothermal plumes interact with their surroundings, such as the determination

of rise height and transport mechanisms. The interactions between the plume and the surrounding ambient fluid (particularly through entrainment) have been seen to be intricately tied to the vortex dynamics of the plume (Sreenivas and Prasad 2000). These interactions are also dependent on the source conditions and distribution of vent orifices long the chimney, as multiple coalescing plumes display unique entrainment behaviour (Cenedese and Linden 2014). This entrainment activity creates inflow velocities, which have been seen to be sources of plume turbulence (Wu 2017). These plume characteristics from localized high temperature venting are capable of causing circulation on scales many orders of magnitude larger than the vent field size (Helfrich and Speer 1995). It is therefore desirable to analyze how the turbulent plume characteristics respond to conditions at the venting source and horizontal flows, as well as determining how sensitive the computational model is to changing model and source parameters.

This chapter is comprised of three sections corresponding to each comparison. For each of these sections, we will examine the turbulent kinetic energy (TKE) and thermal variance production rates obtained from the model output as described in Chapter 2. Turbulent kinetic energy production terms measured from the model output include shear production, buoyancy, and vertical advection; thermal variance terms include production by heat fluxes acting on thermal gradients, and vertical advection. The dissipation rates inferred by a steady state balance with production is then calculated. The vertical velocity of the plume will also be discussed because it is the primary variable that controls vertical transport. As shown in Chapter 2, the

refractive index fluctuations are dominated from the calculated thermal variance dissipation and so will not be shown.

3.2 Variation of the Vertical Smagorinsky Coefficient

The first comparison made is between model runs having $C_{SV} = 0.14$ and $C_{SV} = 0.04$ (comparing experiments 4 and 5 with experiment 3). In the previous chapter the $C_{SV} = 0.14$ assumption was discarded as it caused the refractive index fluctuations to display unrealistic behaviour when compared to observations. Here the effects of the $C_{SV} = 0.14$ assumption will be examined on the turbulent production quantities of interest.

Turbulent Kinetic Energy

Figure 3.1 shows the dependency of TKE terms and the resulting dissipation rate on the vertical Smagorinsky coefficient with comparisons made to experiment 3. The increase in the vertical Smagorinsky coefficient can be seen to increase the shear production of turbulent kinetic energy (top panels). This increase in magnitude is especially evident during times of low background crossflow where shear production reaches its largest magnitudes. This is because the increased value of C_{SV} results in a larger value for A_V and higher shears when the plume is upright ($P = A_H S_H^2 + A_V S_V^2$). When compared to experiment 3, the larger vertical Smagorinsky coefficient results in large production values compared to the 1-1 reference line. Both experiments 4 and 6 converge at higher values during times of

low crossflow and diverge during maximum flow when shear production is minimum. This implies that the heat flux change has a more pronounced effect during maximum cross flows. When compared to experiment 3, the 50 MW (experiment 4) correlation coefficient is high compared to the 80 MW (experiment 6) correlation coefficient. Both experiment 4 and 6 approach the value of experiment 3 for brief periods when the cross flow is accelerating.

Negative buoyancy values act as sources of TKE since they occur where $N^2 < 0$, and the plume is under unstable stratification. The vertical Smagorinsky coefficient can create large variations in buoyancy changes. This is due to the dependance of buoyancy on K_V which increases as $K_V = A_V Pr^{-1}$. In the scatter plot, the buoyancy magnitudes with the larger vertical Smagorinsky coefficient are predominantly below the 1-1 reference line when compared with experiment 3. The slope is nearly vertical, indicating a very low amount of variation in experiment 3 compared to experiments 4 and 6. The correlation coefficient is moderately high particularly for the 50MW (experiment 4) case showing they both have tidal variations.

The magnitude of TKE advection is also strongly affected by the chosen vertical Smagorinsky coefficient, where values for experiments 4 and 6 are greater by a factor of 10 (third row panels). The 50 MW $C_{SV} = 0.04$ case is mostly clustered about zero, while the $C_{SV} = 0.14$ cases are less than zero. This implies that vertical advection always acts as a source term for turbulent kinetic energy. This is likely due to the increase in both the TKE (q^2) and the cross sectionally averaged vertical

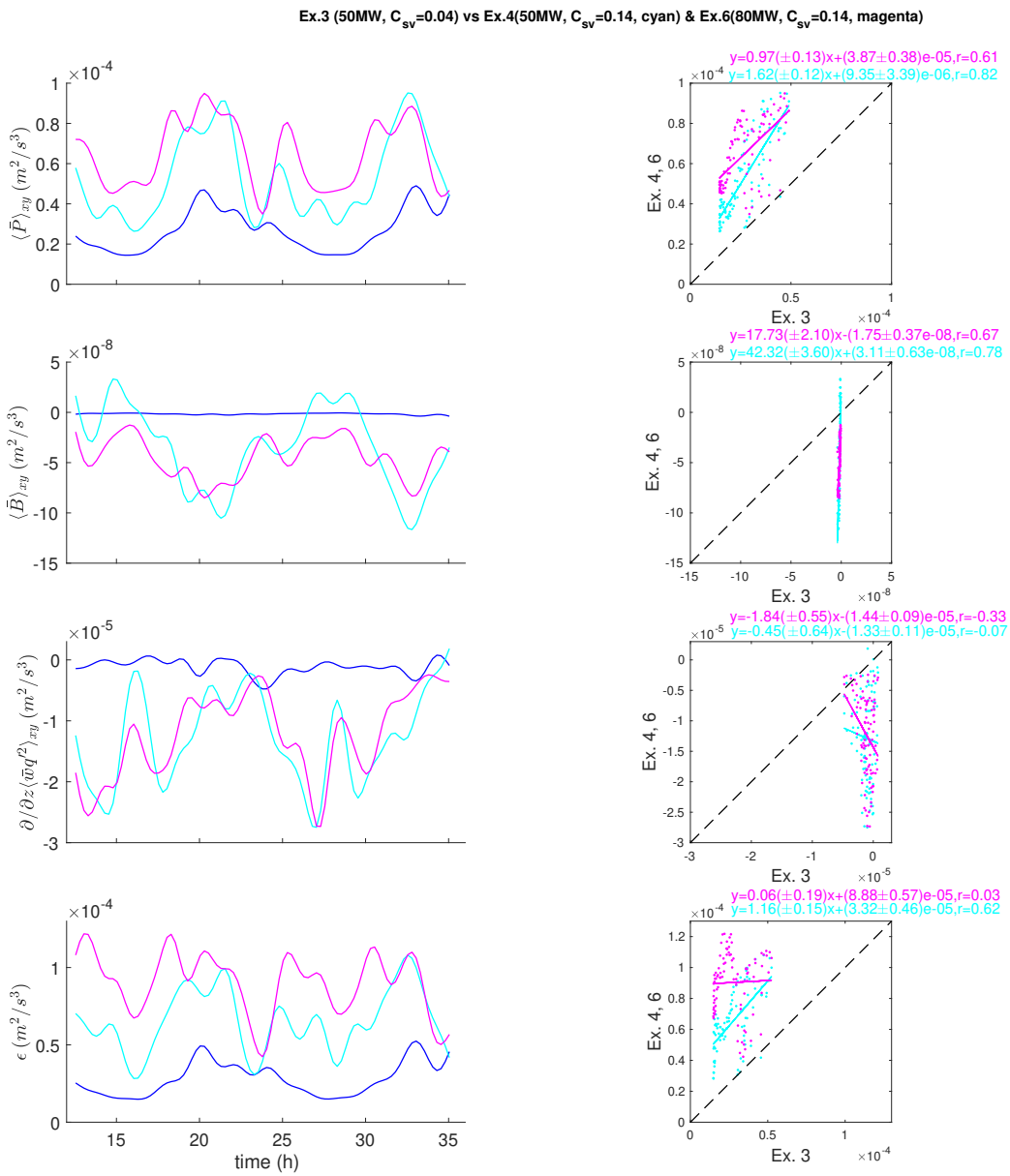

Figure 3.1: Variations in the TKE terms due to changes in the vertical Smagorinsky coefficient are shown. Time series of magnitudes are shown over 30 hours, and comparative plots are shown for experiments 4 and 6. Experiment 3 (50 MW, $3x3m^2$, $C_{SV} = 0.04$) is shown in blue. Experiment 4 (50 MW, $3x3m^2$, $C_{SV} = 0.14$) is shown in cyan. Experiment 6 (80 MW, $3x3m^2$, $C_{SV} = 0.14$) is shown in magenta. The top row displays shear production, the second row displays buoyancy, the third row displays advection gradient, and the bottom row displays TKE dissipation rate.

velocity ($\overline{w}$), causing the production to have a steeper slope as a function of depth. The larger vertical Smagorinsky coefficient experiments (4 and 6) have larger magnitudes of advection during times of largest crossflow (contrary to buoyancy and shear production terms), whereas there is no clear tidal cycle evident for experiment 3. As a result, the scatter plots show very low correlation, indicating no relationship with experiment 3.

Interestingly, for $C_{SV} = 0.14$ shear production and advection are closer in magnitude than they are for the $C_{SV} = 0.04$ experiment. This means that $C_{SV} = 0.14$ advection of turbulent kinetic energy will have an affect on the calculated $C_{SV} = 0.14$ TKE dissipation rate especially during maximum flows, but for the most part dissipation is predominantly balanced by shear production. When compared to experiment 3 the divergence in magnitudes for experiments 4 and 6 during maximum crossflows and have larger values, as can be seen by the placement of the scatter relative to the 1-1 reference line. Experiment 4 shows a moderate correlation, and the slope is near 1, indicating that as the magnitudes of ϵ increase they do so to the same degree, implying a sensitivity to the crossflow. For experiment 6, there is no significant correlation with experiment 3.

Thermal Variance Terms

Figure 3.2 shows the the dependency of thermal variance production rates and the calculated dissipation rate on the vertical Smagorinsky coefficient. The production of thermal variance (top row panels) shows differences that are especially pronounced

during times of low background crossflow where thermal variance production reaches its highest magnitudes. This difference is due to the dependance of P_θ on the vertical mixing coefficients K_V and temperature gradients via $K_V\theta_V^2 + K_H\theta_H^2$ with larger gradients occurring when the plume is upright. The comparison with experiment 3 shows the scatter above the 1-1 reference line indicating significantly larger values during times of low background crossflow. Both experiments 4 and 6 can be seen to converge at these larger magnitudes during times of low crossflow and diverge at smaller magnitudes with the 50 MW $C_{SV} = 0.14$ being more like the 50 MW $C_{SV} = 0.04$ case. When compared to experiment 3, the moderately high correlation implies a dependance on the crossflow.

For advection (middle panels), the magnitudes of the $C_{SV} = 0.14$ case are much larger, up to three times larger than the $C_{SV} = 0.04$ experiment. The scatter set comparison shows no significant correlation with experiment 3, and no tidal cycle is prevalent. Magnitudes are always negative, implying a source of thermal variance. The high values are attributed to increased θ'^2 and $\overline{w}$ as a result of higher mixing and a steeper profile.

The dissipation rate of thermal variance (bottom panels) is balanced by the vertical mean and turbulent transport with small modulations from heat flux production. For $C_{SV} = 0.14$ there is no clear dependence on the background crossflow. The scatter sets show very little correlation with the $C_{SV} = 0.14$ result implying that they show no discernible tidal cycle. This is particularly evident

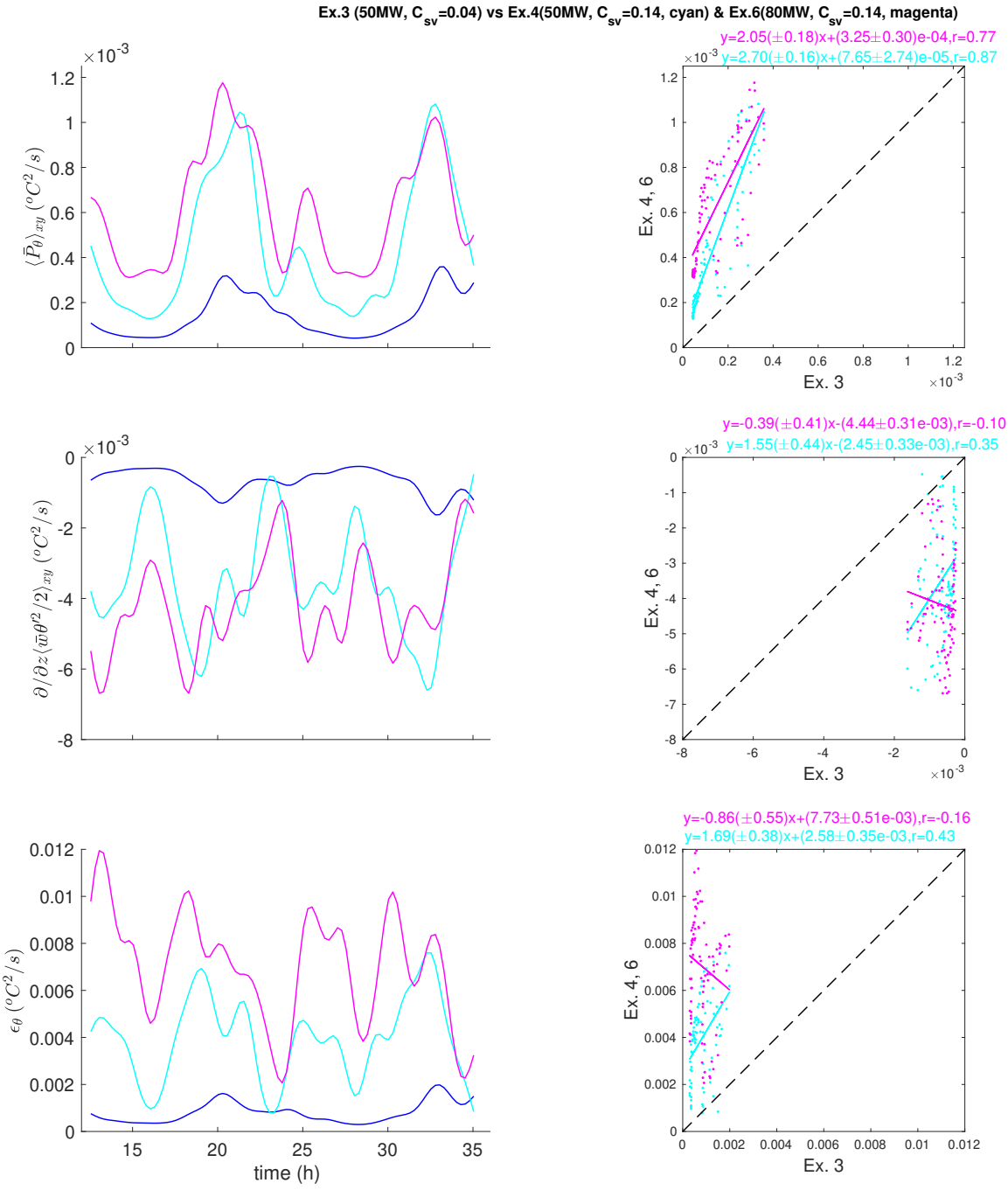

Figure 3.2: Variations in the thermal variance terms due to changes in the vertical Smagorinsky coefficient are shown. Time series of magnitudes are shown over 30 hours, and comparative plots are shown for experiments 4 and 6. Experiment 3 (50 MW, $3x3m^2$, $C_{SV} = 0.04$) is shown in blue. Experiment 4 (50 MW, $3x3m^2$, $C_{SV} = 0.14$) is shown in cyan. Experiment 6 (80 MW, $3x3m^2$, $C_{SV} = 0.14$) is shown in magenta. The top row displays production of thermal variance, the middle row displays the advection gradient, and the bottom row displays thermal variance dissipation rate.

during times of highest crossflow, where experiment 3 displays its lowest magnitudes while experiment 6 has its highest magnitude.

Vertical Velocity

Figure 3.3 shows the dependency of the vertical velocity averaged over time and horizontal cross section ($\langle \overline{w} \rangle_{xy}$) on vertical Smagorinsky coefficient. The $C_{SV} = 0.14$ experiments display larger velocities throughout the time series, as well as a much lower response to the background crossflow. The strong vertical mixing and hence turbulence levels result in a lack of sensitivity to the crossflow compared to the $C_{SV} = 0.04$ experiment. The comparison to experiment 3 shows that both slopes are less than one, which indicates that as the vertical velocity magnitude for experiment 3 increases, the velocities for experiments 4 and 6 increase to a lesser degree. The low correlation also indicates that the $C_{SV} = 0.14$ case has little dependance on the crossflows. This is presumably due to the variability that arises when the cross flow accelerates causing values to approach experiment 3 values. The increased Smagorinsky coefficient clearly results in larger magnitudes of vertical velocity at slack water, which are not unreasonable, but the reduction at times of maximum crossflow is not evident in these experiments.

3.3 Heat Transport

The hydrothermal fluid injected into the deep ocean is a large source of energy, particularly when scaled up to all mid ocean ridges. Two values for hydrothermal

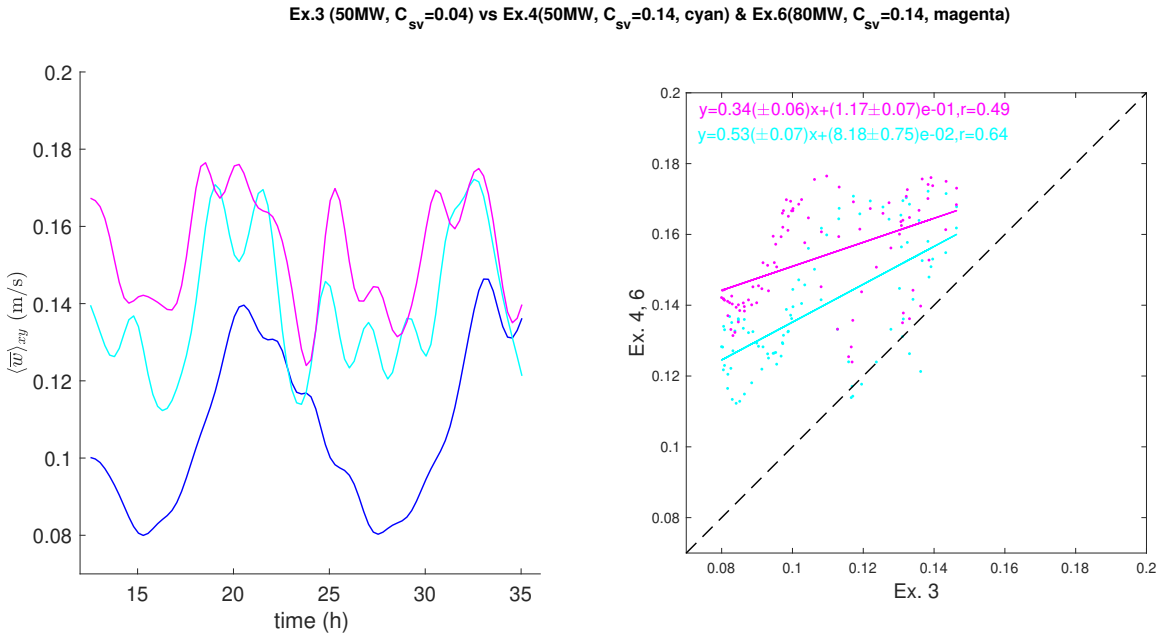

Figure 3.3: Variations in vertical velocity due to changes in the vertical Smagorinsky coefficient are shown. Experiment 3 (50 MW, $3x3m^2$, $C_{SV} = 0.04$) is shown in blue. Experiment 4 (50 MW, $3x3m^2$, $C_{SV} = 0.14$) is shown in cyan. Experiment 6 (80 MW, $3x3m^2$, $C_{SV} = 0.14$) is shown in magenta. Time series of magnitudes are shown over 30 hours, and comparative plots are shown for experiments 4 and 6.

heat transport and their influence on hydrothermal plume turbulence and vertical velocity characteristics are examined. In this section, a comparison is made between 50 MW (experiment 3) and 80 MW (experiment 5), for each of the turbulent plume quantities of interest. Both of these experiments have a cross sectional area of 3x3 m^2.

Turbulent Kinetic Energy

In Figure 3.4, the variation of TKE characteristics with increase in heat flux (5.6 MW/m^2 vs. 8.9 MW/m^2) over a constant area is examined. The shear production (top panels) in experiment 3 (50 MW) and experiment 5 (80 MW) display temporal variability due to background crossflow, but there is a slight loss of variability with the 80 MW case. This indicates that the increased heat flux results in a reduced sensitivity to the tidal crossflow. The difference in magnitudes are especially clear when magnitudes are at their lowest during times of largest crossflow. The scatter set shows the increased heat flux displays both a lower tidal variability, and similar overall magnitudes to the lower heat flux. The correlation coefficient between experiments 3 and 5 is fairly high for the shear production of TKE, indicating both display tidal variations.

Both experiment 3 and 5 display some temporal variability in the buoyancy (second row panels) due to the background crossflow. The 50 MW case varies between -0.8e-9m^2/s^3 and -3.75e-9m^2/s^3, while the 80 MW case varies between -0.8e-9m^2/s^3 and -3.25e-9m^2/s^3. Though they display similar magnitude ranges, the

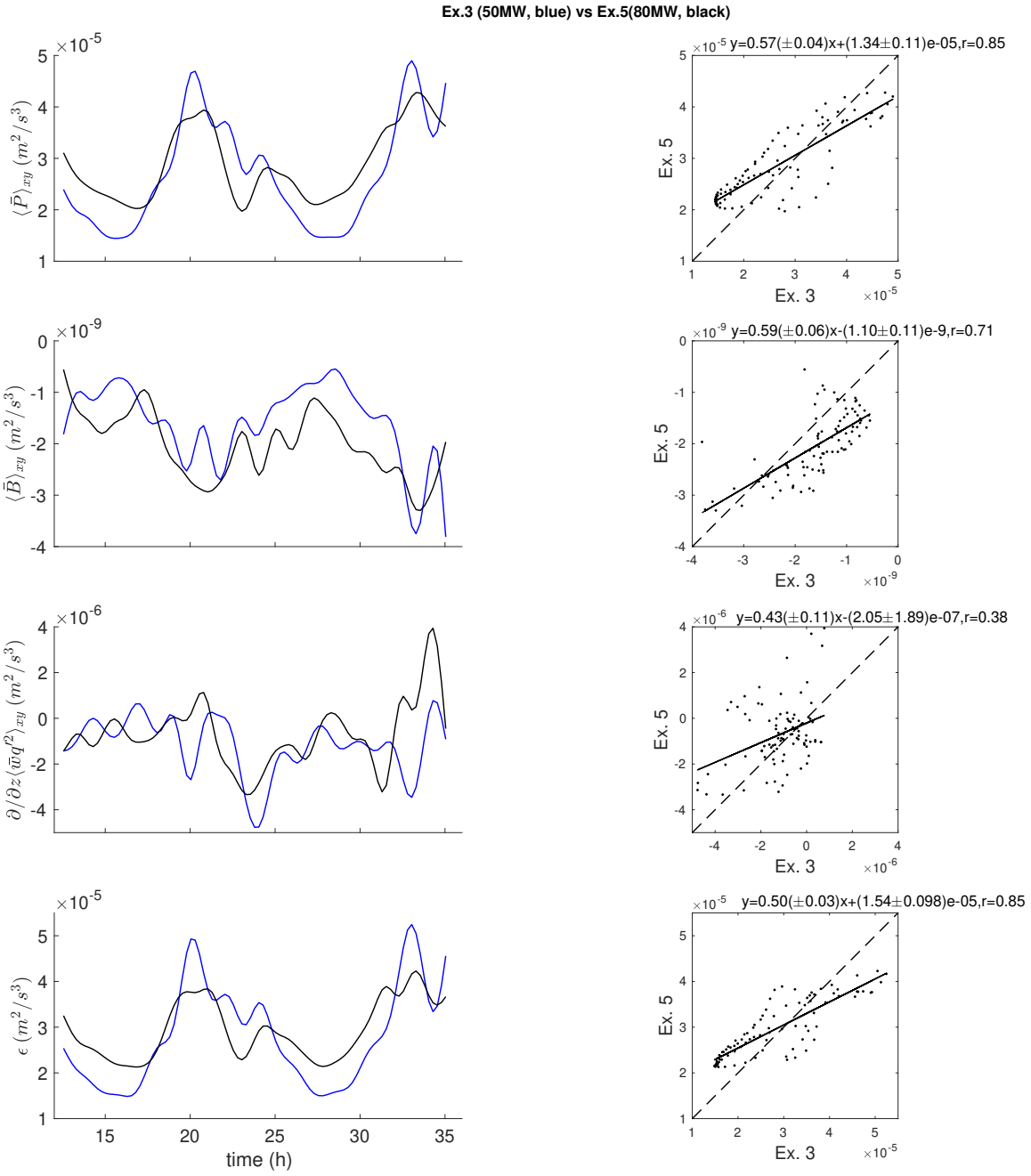

Figure 3.4: Variations in the TKE terms due to changes in the heat flux are shown. Time series of magnitudes are shown over 30 hours, and comparative plots are shown for experiment 5. Experiment 3 (50 MW, $3x3m^2$, $C_{SV} = 0.04$) is shown in blue. Experiment 5 (80 MW, $3x3m^2$, $C_{SV} = 0.04$) is shown in black. The top row displays shear production, the second row displays buoyancy, the third row displays advection gradient, and the bottom row displays TKE dissipation rate.

increased heat flux case is seen to have larger magnitudes during most times throughout the time series as most of the scatter points fall below the 1-1 line. Unlike the shear production, the scatter of buoyancy lies predominantly below the 1-1 line, indicating some variation in magnitude. Most of the scatter lies under the 1-1 reference line, indicating that the increased heat flux generally results in higher values, particularly at times of strong crossflow. At times of low crossflow, where buoyancy is strongest, the fitted line crossed the 1-1 reference line, indicating that lower heat flux magnitudes dominate at these times.

For vertical advection, neither experiment 3 nor experiment 5 display clear temporal variability (third row panels) with the variations in background crossflow. The similarity of magnitude ranges suggests that the increasing heat flux has little influence on the advection gradient of turbulent kinetic energy. The scatter set comparison is poorly correlated, indicating no variations with crossflow.

The calculated TKE dissipation rate (bottom panels) for both experiments is dominated by the shear production of TKE. The 50 MW case varies between 1.5e-5m^2/s^3 and 4.75e-5m^2/s^3, while the 80 MW case can be seen to vary between 2e-5m^2/s^3 and 4e-5m^2/s^3. The comparison between experiment 3 and 5 is similar to that of the shear production, with increased heat flux resulting in larger magnitudes at high crossflow conditions, and lower magnitudes under smaller crossflow conditions. This indicates that an increase in heat flux results in a smaller response to the background crossflow.

Thermal Variance

Figure 3.5 shows the variation of thermal variance production terms with increase in heat fluxes. Both the 50 MW case and the 80 MW case display strong temporal variability in the production of thermal variance (top panels) in response to the background crossflow. Increasing heat flux can be observed to increase both the maximum and minimum values. This is likely caused both by the increase in shear due to buoyant rise resulting in a larger eddy viscosity, as well as stronger thermal gradients produced by the larger temperature gradients resulting from increased heat flux. When compared to experiment 3, the increased heat flux results in large values above the 1-1 reference line. This indicates that the higher heat flux does result in a slight increase in production magnitudes. The slope is very nearly 1, indicating that the experiments both have the same response to background crossflow, increasing or decreasing to the same degree. The correlation coefficient here is quite large, suggesting they both have tidal variations.

The vertical advection of thermal variance in the 50 MW case shows more of a temporal variability due to the background crossflow. The increase in heat flux results in a loss of variability with the background crossflow. An increase in thermal variance is expected in the 80 MW case, along with larger average vertical velocities during times of low background crossflow resulting in both a larger vertical transport gradient, but this is not observed everywhere as the best fit line converges to the 1-1 reference line at high magnitudes. However the slope of the best fit line is less than

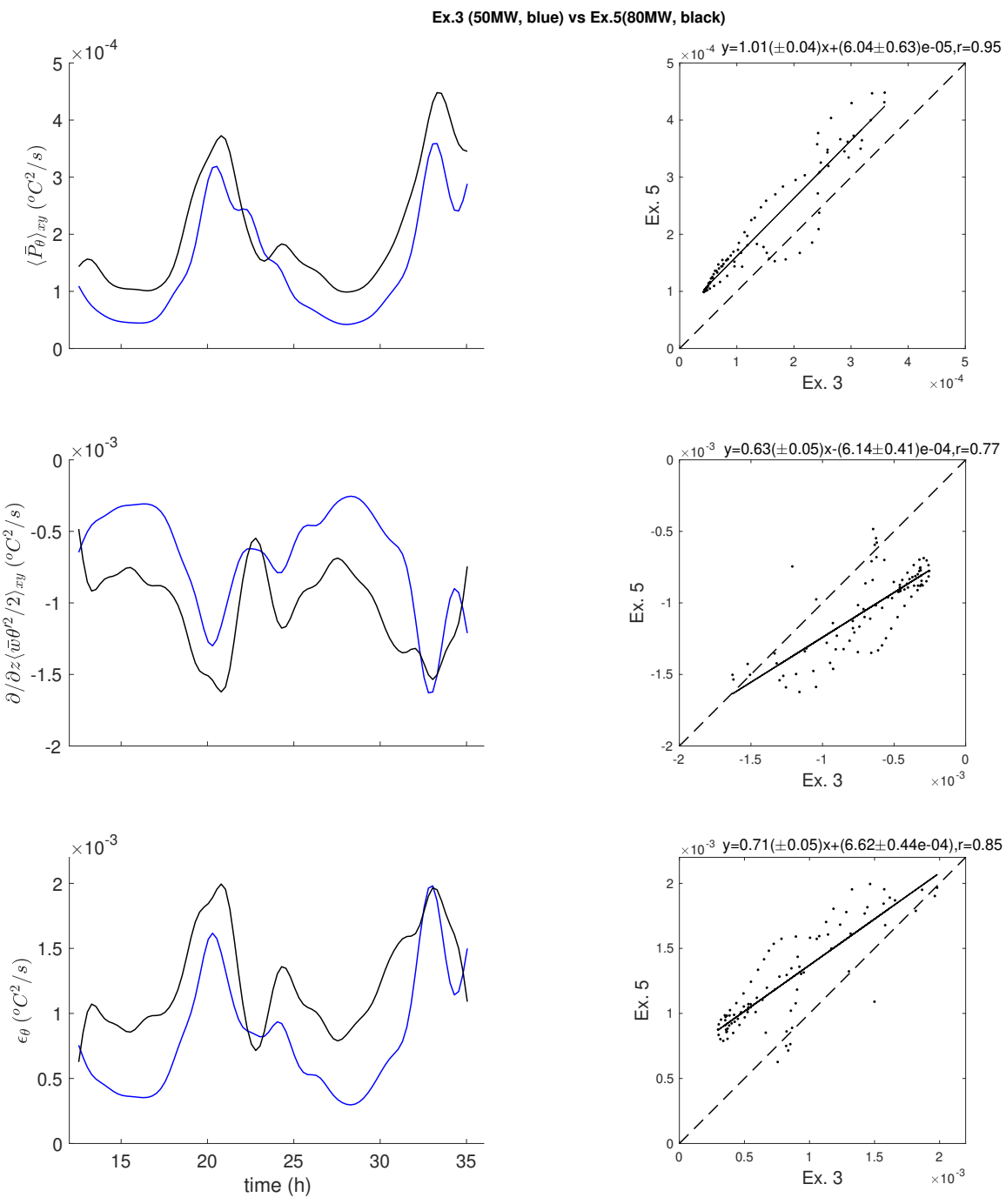

Figure 3.5: Variations in the thermal variance terms due to changes in the heat flux are shown. Time series of magnitudes are shown over 30 hours, and comparative plots are shown for experiment 5. Experiment 3 (50 MW, $3x3m^2$, $C_{SV} = 0.04$) is shown in blue. Experiment 5 (80 MW, $3x3m^2$, $C_{SV} = 0.04$) is shown in black. The top row displays production of thermal variance, the middle row displays the advection gradient, and the bottom row displays thermal variance dissipation rate.

one, so there is a larger sensitivity to the maximum flow and increasing advection of thermal variance. Compared to experiment 3, an increase in heat flux can be seen to result in larger magnitudes, particularly where the crossflow is at its strongest.

The calculated dissipation rates (bottom panels) closely follow the advective production and are only weakly modulated by the heat flux production. The 50 MW case varies between 0.4e-3$°C^2/s$ and 1.6e-3$°C^2/s$, while the 80 MW case varies between 0.6e-3$°C^2/s$ and 2e-3$°C^2/s$. Increasing heat flux can be seen to remove some of the tidal variability observed in the thermal variance dissipation as the scatter set plot shows a slope of less than one. However this correlation is high, confirming that both times series are sensitive to the crossflows. The increase in heat flux results in larger magnitudes of thermal variance dissipation, as evidenced by the placement above the 1-1 reference line. The fitted line converges with the reference line at times of lowest crossflow, where dissipation magnitudes are at their largest and diverge at times of large crossflow implying that the thermal variance dissipation rate is increased more notably with an increase in heat flux during this time.

Vertical Velocity

Figure 3.6 compares the temporally and spatially averaged vertical velocity as a result of heat flux change with a constant source area. During times of large crossflow $\langle \overline{w} \rangle_{xy}$ is increased to higher values compared to the 50 MW case. This increase implies that the plume has an increased resistance of the vertical velocity to high crossflow conditions because the variability is smaller. This is likely due to the

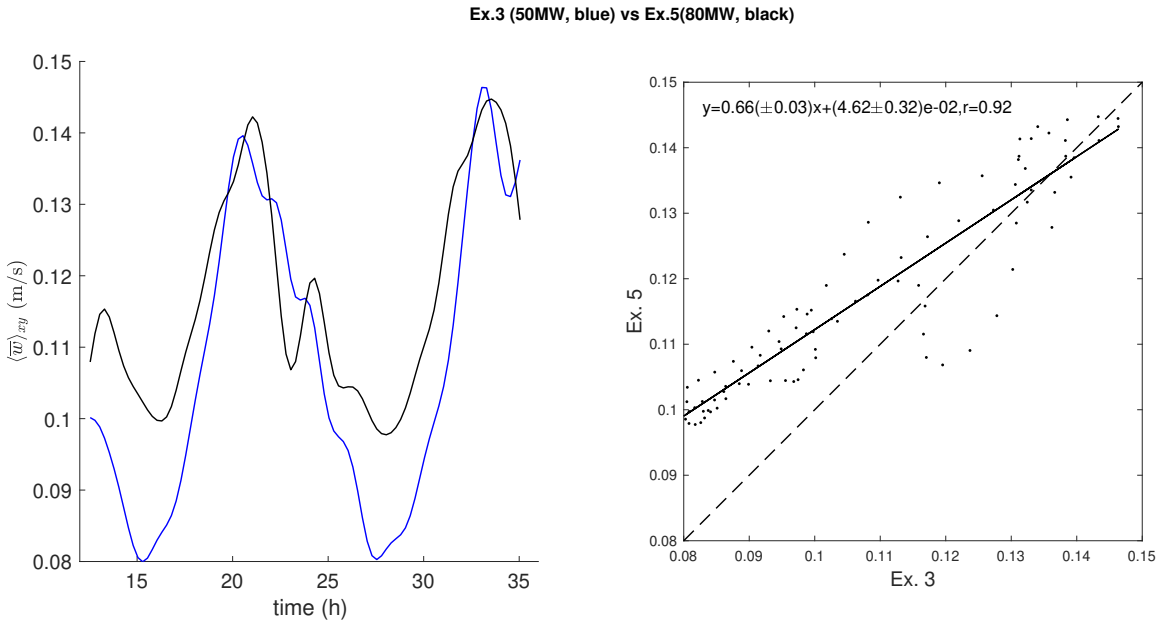

Figure 3.6: Variations in vertical velocity due to changes in the heat flux are shown. Experiment 3 (50 MW, $3x3m^2$, $C_{SV} = 0.04$) is shown in blue. Experiment 5 (80 MW, $3x3m^2$, $C_{SV} = 0.04$) is shown in black. Time series of magnitudes are shown over 30 hours, and comparative plots are shown for experiment 5.

larger temperatures retaining stronger buoyancy even under strong crossflow. The entrainment and cooling of the plume decreases the vertical velocities, but temperatures are able to sustain greater levels of vertical velocity than those for the 50 MW case. Compared to experiment 3, the increase in heat flux causes larger velocity magnitudes. The scatter set shows a high correlation associated with the crossflow and a slope of less than one that diverges from the 1-1 reference line during maximum cross flows and converges to the reference line at slack water.

3.4 Source Area

As the turbulent convection model does not deal with topographical interactions, and does not account for an ocean bottom, there must be a region that is selected as the source area for hydrothermal effluent. This area represents a fully coalesced plume (from vent chimneys where multiple orifices exist) that has already achieved some representative radius at the start of the modeling. This can be assumed, as the coalesced plume from multiple sources is identical to a single plume originating from a virtual point source (Kaye and Linden 2004) In this section, comparisons of 3x3 m^2 (experiment 3) to 4x4.5 m^2 and 6x6 m^2 (experiment 1 and 2 respectively) will be made. These source area increases correspond to a heat flux decrease of 5.6, 2.8 and 1.4 MW/m^2 respectively.

Turbulent Kinetic Energy

The variation of turbulent characteristics with increase in source area is shown in Figure 3.7. The time series of shear production (top panels) shows that increasing source the area results in a decrease of shear production, particularly evident at times of low background crossflow where magnitudes are largest. Compared to experiment 3, increasing source area results in smaller values with respect to the 1-1 reference line. Experiments 1 and 2 converge onto the 1-1 reference line at low magnitudes (when crossflow is at its strongest), and diverge at high magnitudes. This indicates that the source area change has a more pronounced effect during the

low crossflows. The correlation coefficients are high, displaying that the experiments have clear tidal variations.

Buoyancy for each case (second row panels) differs by a small amount during periods of low background crossflow when the magnitudes are maximum. However according to the scatter plots there are only a few times when the buoyancy is less than the 3x3 m^2 case; most of the data lies above the 1-1 reference line and no discernible differences between each of the runs can be seen since the slope intercepts show no substantial difference. However the moderately high correlation coefficient also implies that buoyancy for each case is sensitive to the tidal time series. The increase in source area can be seen to reduce the maximum values of buoyant production that occurs within the plume at slack water. This is expected as the heat output is spread over a larger area, lowering the initial temperatures of the plume. Compared to experiment 3, both experiment 2 and 1 can be seen to have lower magnitudes (from placement above the 1-1 reference line) and a smaller tidal variation as indicated by the moderate correlation coefficient. Experiments 2 and 1 converge with the 1-1 line at low magnitudes, indicating that buoyancy for all cases reaches the same magnitudes at times of large background crossflow.

The magnitude of the vertical advection of TKE for each case (third row panels) varies about zero without a clear response to background crossflow. The increase in source area does not show any appreciable change in magnitude. The scatter comparison with experiment 3 shows that the larger source area experiments

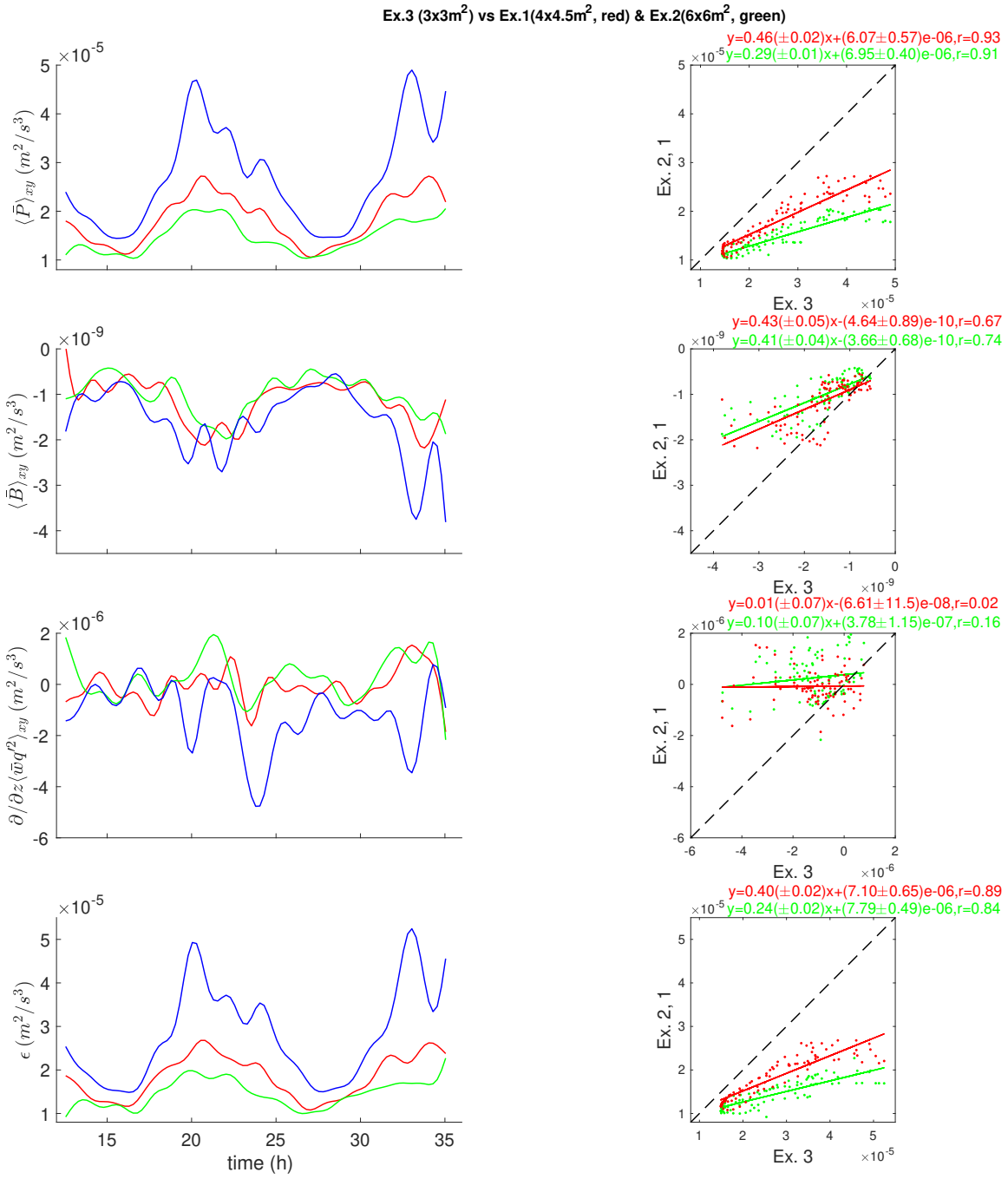

Figure 3.7: Variations in the TKE terms due to changes in the source area are shown. Experiment 1 (50 MW, $4x4.5m^2$, $C_{SV} = 0.04$) is shown in red. Experiment 2 (50 MW, $6x6m^2$, $C_{SV} = 0.04$) is shown in green. Experiment 3 (50 MW, $3x3m^2$, $C_{SV} = 0.04$) is shown in blue. Time series of magnitudes are shown over 30 hours, and comparative plots are shown for experiments 2 and 1. The top row displays shear production, the second row displays buoyancy, the third row displays advection gradient, and the bottom row displays TKE dissipation rate.

(2 and 1) show a smaller range of magnitudes. The scatter set shows no significant correlation with experiment 3.

The calculated dissipation (bottom panels) is primarily balanced by the shear production as previously shown. Similarly to the shear production comparison, it can clearly be seen that an increase in source area reduces the quantities that occur within the plume. Both maximum and minimum magnitudes are reduced with increasing area, but the difference is most pronounced during times of low background crossflow where magnitudes are at their largest. The high correlation coefficient for each experimental run shows that there is a clear response to tidal crossflow.

Thermal Variance

The variation of thermal variance characteristics with increase in source area with a constant heat transport (or decrease in heat flux) is examined in Figure 3.8. The top row panels show the production of thermal variance. Increase in source are can be seen to reduce the magnitudes of thermal variance production at large magnitudes when the crossflow is at its weakest, while magnitudes at times of large crossflow are not changed. The comparison with experiment 3 shows the scatter below the 1-1 reference line for both experiment 2 and 1, indicating smaller values. Experiments 2 and 1 diverge from the reference line during minimum crossflow and converge with the 1-1 reference line at lower magnitudes at maximum crossflow. This suggests that the production term for all cases reaches the same magnitudes at times

of large background crossflow. A strong tidal variance is observed from the high correlation coefficient.

The vertical advection of thermal variance (middle panels) shows that an increase in source area reduces the variability associated with the crossflow (as the distribution is moderately correlated). Differences in magnitude is most evident during times of low crossflow, where magnitudes are at their highest. This can be seen in the scatter plot, where the comparisons of experiments 2 and 1 both converge with the 1-1 reference line at the lowest magnitudes, diverging at larger magnitudes. Compared to experiment 3, increasing the source area results in lower magnitude as evidenced by the placement of scatter above the reference line.

As has been previously examined, the dissipation rate of thermal variance (bottom panels) is primarily balanced by the advective production, with some modulation by the heat flux production. As a result, it can clearly be seen that an increase in source area reduces the maximum dissipation magnitudes that occur within the plume during times of low background crossflow. At maximum crossflow, the dissipation converges to a minimum threshold of 0.4e-3$^{\circ}C^2/s$. The strong correlation with experiment 3 indicates that the tidal modulation is strong. Comparison with Figure 3.5 shows a difference in how the dissipation of thermal variance responds to differing heat fluxes due to a change in source area.

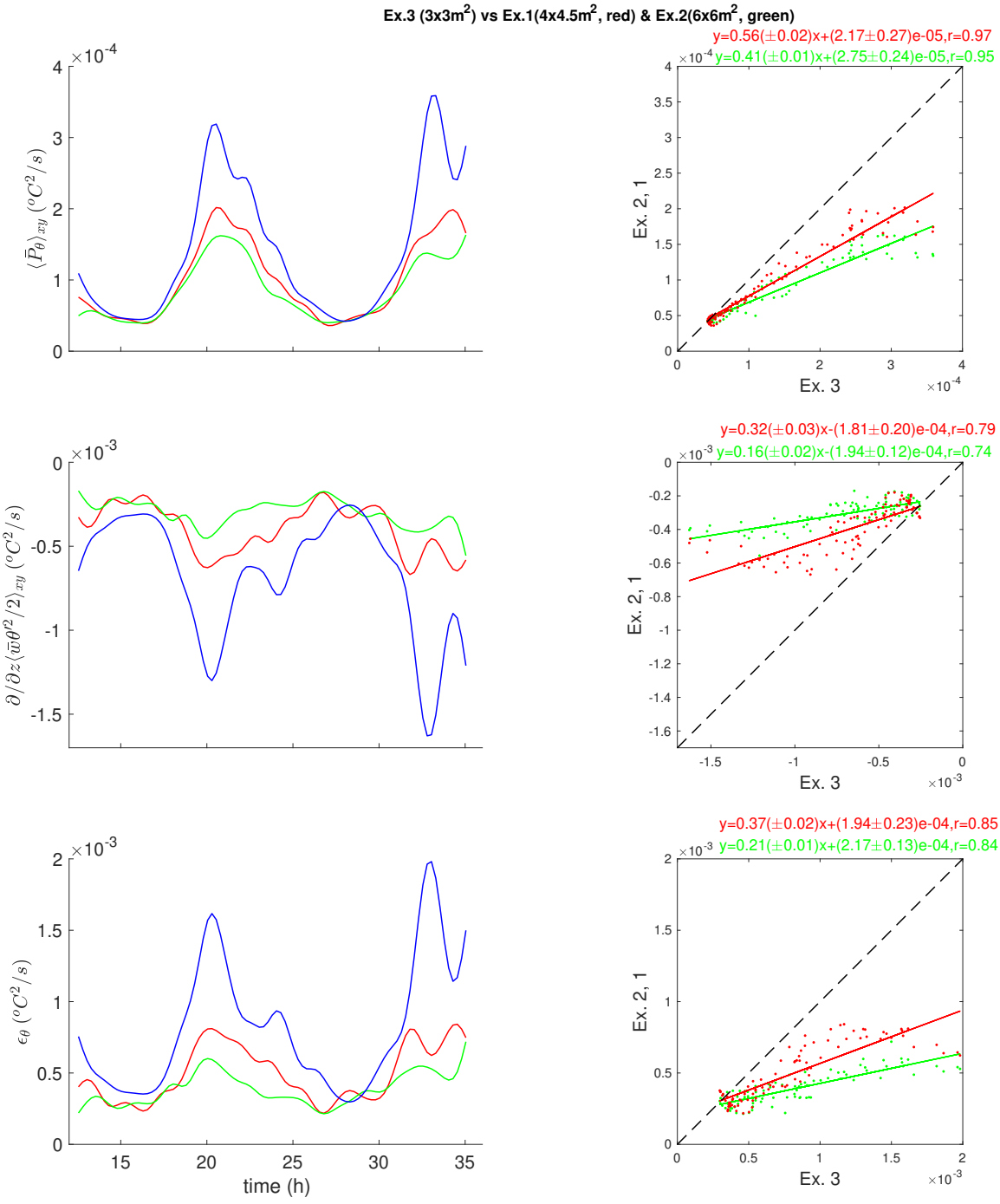

Figure 3.8: Variations in the thermal variance terms due to changes in the source area are shown. Time series of magnitudes are shown over 30 hours, and comparative plots are shown for experiments 2 and 1. Experiment 1 (50 MW, $4x4.5m^2$, $C_{SV} = 0.04$) is shown in red. Experiment 2 (50 MW, $6x6m^2$, $C_{SV} = 0.04$) is shown in green. Experiment 3 (50 MW, $3x3m^2$, $C_{SV} = 0.04$) is shown in blue. The top row displays production of thermal variance, the middle row displays the advection gradient, and the bottom row displays thermal variance dissipation rate.

Vertical Velocity

In Figure 3.9 the variation of the vertical velocity ($\langle\overline{w}\rangle_{xy}$) with increase in source area is examined. As with the thermal dissipation rate, an increase in source area reduces the maximum velocity magnitudes that occur within the plume. Velocities at low crossflow conditions display larger differences dependent on source area than the velocities observed at high background crossflows. Comparison to experiment 3 shows that experiment 2 and 1 converge at lower vertical velocity magnitudes, with those values for experiment 3 during maximum crossflow and diverge at times of low background crossflow. The scatter distribution is located below the 1-1 reference line showing that the smaller source area (experiment 3) has greater variability compared to experiments 1 and 2.

3.5 Discussion and Interpretation of Results

An important question to address when considering the temporal changes in plume characteristics with horizontal cross flow is how much of the apparent variation at a given height is due to plume bending. In other words: does the plume retain similar magnitudes of turbulence characteristics at the same distance along the axis under both conditions of flow?

To test this, the turbulent values need to be determined at a given distance from the source along the plume axis, rather than simply at a given height. The actual height above the bottom of the model domain that corresponds to the same

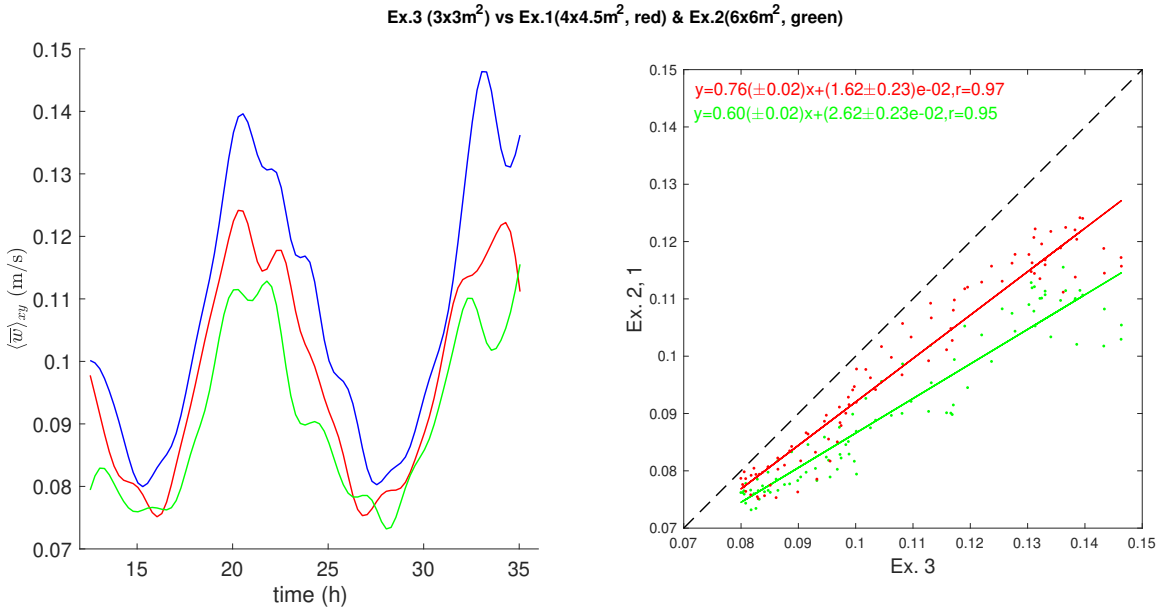

Figure 3.9: Variations in vertical velocity due to changes in the source area are shown. Experiment 1 (50 MW, $4x4.5m^2$, $C_{SV} = 0.04$) is shown in red. Experiment 2 (50 MW, $6x6m^2$, $C_{SV} = 0.04$) is shown in green. Experiment 3 (50 MW, $3x3m^2$, $C_{SV} = 0.04$) is shown in blue. Time series of magnitudes are shown over 30 hours, and comparative plots are shown for experiment 2 and 1.

axial distance will depend on the strength of the crossflow and the degree to which the plume is observed to bend. This relationship is a result of the complicated interaction of buoyancy and momentum at the source, stratification, and the strength of crossflow, and is further complicated by the crossflow being time variant. To get an idea of what sort of plume bending is occurring, the plume center can be approximated by the time averaged temperature profile where the center of the plume corresponds to the highest temperature magnitude. From examination of the temperature cross section shown in Figure 2.6, the angle of plume bending during times of high background cross flow is determined to be 30° from upright. Since the source area for this case is a 4x4.5 m^2 area centered about zero, and the 20 m above source was calculated from the virtual point source (z_0=2176), the angle was calculated in relation to this value of z_0. This results in the along axis distance of 20 m from the virtual point source being located at a height of approximately 17 m above the virtual source depth.

Another point worth considering is the plane over which the spatial average is taken. To obtain a turbulent characteristic relative to the axial position in the plume, it is desired to take the spatial average over the cross sectional area perpendicular to the axis. In this study, the averages are taken over the x-y plane at a constant depth. This approximation works best at lower crossflows and nearer to the source area where the angle of the plume bending is small. Considering that the angle of the 15 minute time average of temperature was shown to describe a plume

bending angle of 30°, this approximation should be sufficient to build a picture of what degree of temporal variability is due to plume bending.

Another potential influence on the temporal variation is the plume widening. As crossflows increase, the plume can be seen to be spread out over a much wider spatial area. This results in a larger number of small magnitude regions being spatially averaged to determine the mean at a given height. This is a useful method to determine the average turbulent quantity occurring through a plume cross section at a given depth, but for an along axis calculation of turbulent plume behavour it is less suited. Tidal modulation observed is due to the plume entrainment lowering the turbulent characteristics at a given depth and there is a large amount of plume widening in the x dimension, but considering an axial coordinate and a spatial average over the perpendicular to axis, the widening is not so severe. This suggests that an axis focused examination of plume characteristics would obtain spatially averaged values (at high crossflows) that do not experience as much of a decrease, since they are not averaging in as many low magnitude areas. Figure 3.10 shows the refractive index values through time for depths of 20m, 18m, and 16m above the virtual point source (using the 2hr lowpass filter). Here it can be seen that at large crossflows, the depth consistent with a 20m along axis distance displays magnitudes higher that those observed at 20m above the virtual point source. This indicates that examination of the average plume characteristics along the axis results in less tidal variation.

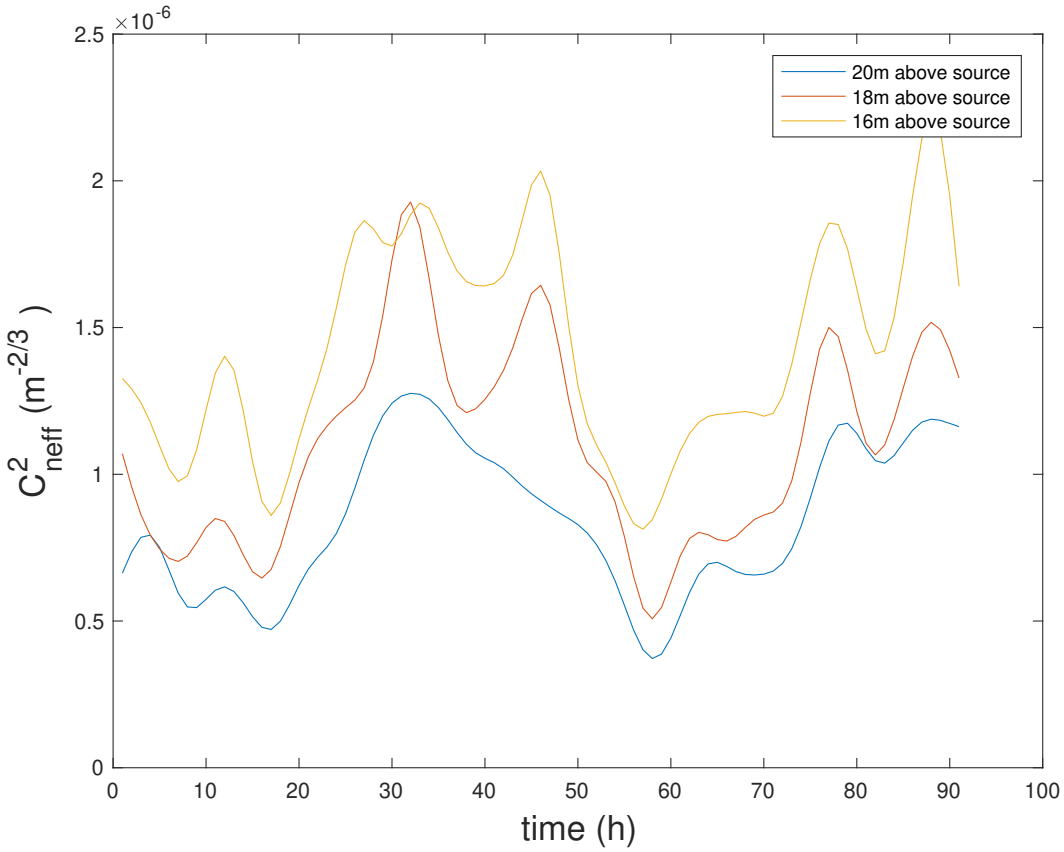

Figure 3.10: Modeled refractive index calculations for heights above the virtual point source of 16m, 18m and 20m.

3.6 Summary and Conclusions

In general, The $C_{SV} = 0.14$ experiments result in turbulent characteristics that are both larger in magnitude and much more resistant to any sort of crossflow to the point of not displaying a clear tidal signal. Although the maximum vertical velocities are in line with observations, they show no dependency on the tidal flow. As a result, it is concluded that this is an unrealistic model for the hydrothermal plume, and as such, the $C_{SV} = 0.14$ assumption is not valid.

From this full comparison of the time series of vertical velocity and turbulent dissipation, the general effects of increasing heat flux (by increasing heat transport) on plume behaviour was characterized. The increase in heat flux resulted in the plume becoming more resistant to the background crossflow, reducing the tidal variability in thermal dissipation by maintaining larger values even under high cross flow conditions. The TKE dissipation rate also showed reduced variability for increased heat flux. Some characteristics displayed variation in the maximum magnitudes (either an increase or decrease with increased heat flux) but this behavior was not as ubiquitous.

From the results presented it is shown that increasing the source area results in two main effects on TKE and thermal variance dissipation. The first is an overall reduction in magnitude. As source area is increased, plume characteristics display weakened signals particularly at times of low background crossflow. This is as would be expected, as the energy and heat injected by the hydrothermal source is

distributed over a wider area. The second is a resistance of the dissipation to the background crossflow. An interesting relationship can be seen between the different of source areas. The doubling of source area from $3\times3\text{m}^2$ to $4\times4.4\text{m}^2$ can be seen to have a larger influence on the plume characteristics than the doubling of source area from $4\times4.4\text{m}^2$ to $6\times6\text{m}^2$. This indicates that the relationship between increasing source area and dissipation may have a nonlinear component. This is further touched upon in the proposed future work section in Chapter 5.

The effects of increasing heat flux by either changing the the source area or the heat transport (and the differences they give when a cross flow exists) hae yet to be comprehensively explored. The research presented here suggests a complex interplay between these two effects that are more involved than simply changing the heat flux of the hydrothermal vent. Clearly the problem cannot simply be reduced to the examination of the source heat flux. More fully exploring these concepts and how they relate to each other may give more information as to how source parameters will condition hydrothermal plume turbulent characteristics.

The interplay between source area and source heat transport can be considered in the context of diffuse and focused sources of hydrothermal flow. As source areas increase for a given energy flux, the plume will approach more diffuse venting flow, which have been seen to present significantly different behaviours (such as rise height, entrainment, and susceptibility to crossflow) than are seen in small area focused flows (Rona and Trivett 1992).

CHAPTER 4

A HYDRODYNAMIC MODEL OF THE ENDEAVOUR RIDGE SEGMENT

4.1 Introduction

The mechanisms of individual hydrothermal flow influence and energy transfer are important as outlined in the previous chapters, but of equal interest are the effects that hydrothermal venting has on a larger scale. Hydrothermal vents don't exist in isolation, but are grouped into larger fields which incorporate both high temperature focused flow and lower temperature diffuse flow. Even though diffuse flow displays significantly lower temperature than focused venting, it is thought to contribute a greater overall amount of heat and mass to the bottom ocean due to its greater spatial coverage (Beaulieu and Szafranski 2018). Examination of how these vent fields generate and modify fluid flow is the focus of this research project.

Hydrothermal effluent has a unique signature in the water column, containing levels of heat and chemicals typically extremely scarce in the bottom ocean. Hydrothermal effluent interactions with currents and tracer tracking are thus of particular interest. These tracking methods have been used to locate or suggest the presence of undiscovered hydrothermal vent locations (Lupton and Craig 1981; Beaulieu et al. 2015). Research has been carried out to determine the extent to which particles from chemical laden plumes settle out of the rising effluent (Dymond

and Roth 1987). As with the exploration of current influences, modeling work has been carried out to predict the extent and spread patterns of particles that originate in the vent, both for tracers and Lagrangian particles (Yu et al. 2012; Chan and Lee 2016). In particular, these methods have been seen to be useful in the tracking of vent larvae, which depend on the hydrothermally modified currents to disperse and colonize new systems (Thomson et al. 2003; Xu et al. 2018).

At the Endeavour ridge segment, plumes have been observed for many years since their discovery in the early 1980s (Baker and Massoth 1987). Interesting venting regions are studied throughout the ocean, and the understanding of these fields and their interactions with currents provides context and insight into hydrothermal influences on circulation. Studies such as those carried out at Axial seamount (Xu and Lavelle 2017) and Lost City (Kelley et al. 2001), as well as the seminal work of Thomson et al. (1990), Thomson et al. (2003), Thomson et al. (2005), and Thomson et al. (2009) contribute to the foundation of the work carried out here as well as context to the ultimate placement of the results into the broader body of hydrothermal research.

Hydrothermal vent plumes and their interactions with regional currents have long been topics of interest. These plumes are known to have far reaching effects and influence flow patterns up to mesoscale basin flow (Lupton 1995; Helfrich and Speer 1995). Specifically, localized high temperature venting has been seen to be capable of causing circulation on scales many orders of magnitude higher than the vent field size (Helfrich and Speer 1995). Within ridge systems, these influences depend on the

current patterns that come about due to external forcings and topographical influence. Study of these currents and flows provides a large body of background work foundational to the understanding of hydrothermal influence (Lavelle and Cannon 2001; Thurnherr et al. 2002; Berdeal et al. 2006). In order to separate the influences that are due primarily to hydrothermal venting systems, numerical modeling methods of multiple fields within a ridge system have been used to examine hydrothermal contributions to fluid flow within these regions (Thomson et al. 2005) (Thomson et al. 2009). Research of observational and modeling methods continues to be of interest in determining specific hydrothermal impact, particularly in regions where the transport of plume effluent is of interest (Xu and Di Iorio 2012) (Xu et al. 2017).

In particular, we are interested in a seabreeze-like effect occurring between venting fields (Thomson et al. 2003). It has been hypothesized that fluid entrainment into hydrothermal plumes at depth causes a flow of water toward the vent field (see Figure 4.1). The hydrothermal activity then transports the fluid upward, where it then spreads out at the buoyantly neutral zone. When there are two vent fields constrained within a ridge valley, there is a region between the plumes where fluid is flowing away in both directions. The fluid cannot be replaced by horizontal flow due to the ridge walls, indicating that it must be replaced along the ridge valley. This suggests that there could be hydrothermally induced circulation cells driven by adjacent vent fields, where ambient bottom fluid is entrained into the plume, rises, spreads out horizontally, and then is recirculated downward, as shown

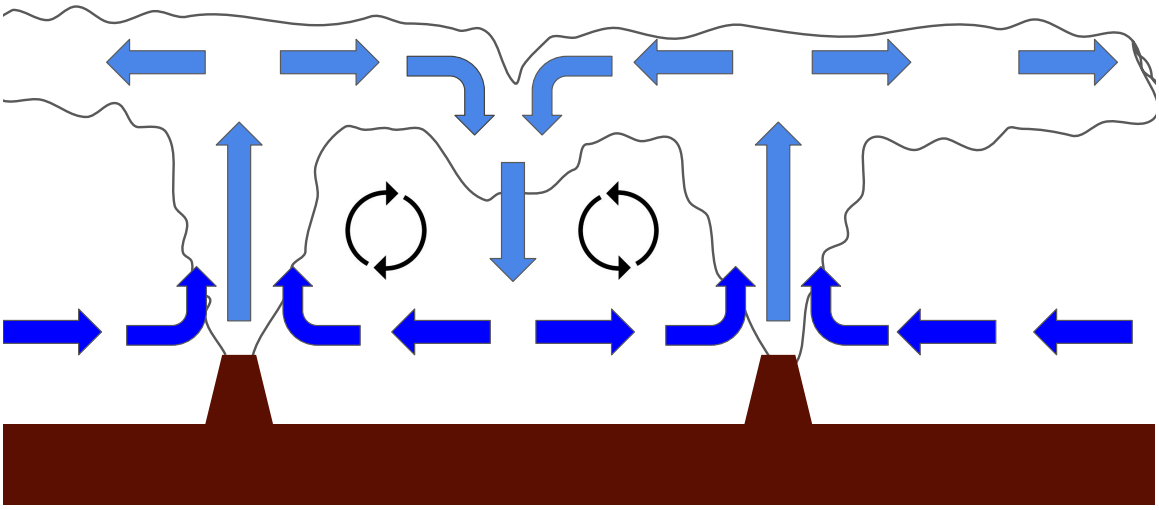

Figure 4.1: Hydrothermal circulation cells: a schematic

schematically in Figure 4.1. This seabreeze-like effect would contribute to large scale circulation through the area via plume entrainment and rise. This kind of fluid circulation cell would have a large impact on our understanding of vertical oceanic fluid flux as well as how chemicals and organisms are transported through the region.

Computational modeling provides the opportunity to investigate the complex physical interactions that give rise to fluid flows within the Endeavour Ridge Segment. Modeling methods have several distinct advantages over other types of study: the data can be more representative than lab or idealized experiments, the regions interrogated are much larger and provide a more robust array of data than observations (such as moorings or towed CTD casts) can give, and the results may

even suggest regions where targeted observations could be made in order to confirm model predictions.

The Endeavor Ridge segment is located 300 km off the coast of Washington state in the Northeast Pacific at depths greater than 2000 meters (see Figure 1.2). Two crests of rock flank the ridge valley, which contains five distinct hydrothermal venting fields spaced approximately 2 to 3 kilometers apart. This region is well characterized, so it provides the ideal location for testing a high resolution ridge scale model.

The Endeavour ridge segment is particularly well suited to the purposes of this study due to the heavy prevalence of moored equipment and detailed observation within the region. Ocean Networks Canada operates the cabled observatory at the Endeavour segment. Multiple instruments stream real time data at various venting sites, and moored water column instruments provide information on regional currents, temperatures, and pressures at multiple depth levels. This data provides a unique opportunity for comparison with modeling data. For the purpose of this project, the moorings located at the northern and southern ends of the valley with current meters placed 5m, 50m, 125m, and 200m above the seafloor gives a measure of regional currents and sea surface height (measured from pressure), and allows for comparison to modeled results.

The vent fields located within the valley of the Endeavour Ridge are approximately 100m in diameter, and vent via both high temperature focused flow and low temperature diffuse flow. Depending on the location, depth, and

temperature of the venting source, hydrothermal plumes may be bound by the ridge walls. Deeper plumes reach neutral buoyancy below the ridges, while plumes from shallower vent fields or higher temperature venting can achieve a rise height above the ridges and escape the system. Fluid flows within the Endeavour Ridge system have temporally varying tidal currents on the order of 10 cm/s aligned along the valley imposed upon a background near steady 5cm/s flow directed to the South West (Allen and Thomson 1993; Lavelle and Cannon 2001). It has also been postulated that a steady background flow along the valley is the direct result of entrainment of ambient seawater into the hydrothermal vent plumes (Thomson et al. 2003).

The effects of hydrothermal activity together with the surrounding topography creates an intricate network of spatially complex and temporally variable patterns of transport around a hydrothermal plume (Xu et al. 2017). These topographical interactions can also play a significant part in how hydrothermal vents influence chemical and biological processes, with ridges constraining or inhibiting transport of particulates such as vent larvae (Xu et al. 2018). Thus, it is of critical importance to appropriately represent the bathymetry in high resolution over the large valley region of the Endeavour segment to appropriately account for these topographic contributions to regional current flow. The modeling described here differs from previous models of Endeavour in that high bathymetric resolution and tidal forcings are used to drive fluid movements.

The overall objectives for this research are broken into four key questions: 1) What are the magnitude and direction of hydrothermal contributions to flows

throughout the Endeavour Ridge? 2) What circulation is brought about by the hydrothermal venting? 3) At what depths and locations throughout the ridge system do circulation cells (if observed) occur? 4) Does the inclusion of tidal forcing over the high resolution Endeavour Ridge system interact with the bathymetry to result in topographical steering? Through this research, the cumulative effect of multiple hydrothermal venting fields in a ridge valley will help determine what flow patterns the venting sites create both individually and communally. The focus is to understand the influence of tidal forcing, regional winds, seafloor discharge, and detailed bathymetry on current and flow within the Endeavour Ridge segment (Juan De Fuca Ridge). The synergistic effects that arise due to the presence of multiple venting fields working in tandem to modify the fluid flow throughout the ridge valley will be of particular importance.

Section 4.2 describes the model methods, and describes the way in which the hydrodynamic model was created and initialized. Section 4.3 shows model results and compares multiple cases of varying vent activity at hydrothermal fields located in the valley and the flow patterns that arise. Section 4.4 discusses a nested model approach and the preliminary results and significance of this nested model output.

4.2 Methods

A high-resolution, computational model was developed using the Finite Volume Community Ocean Model version 3.2 (FVCOM) (Chen et al. 2006) to examine how the presence of hydrothermal venting (both diffuse and focused flows) affect regional

currents. FVCOM was selected for this purpose because it can appropriately capture the variable bathymetry, can include discharge on the seafloor, and has many preprocessing and analysis tools developed by the FVCOM user community. FVCOM is an unstructured grid, finite volume, free surface three-dimensional model. It computes fluxes between triangular control volumes in order to solve the integral forms of the governing equations of motion, heat, salt, and mass. Finite volume allows for a good representation of the conservation of mass and momentum, which is particularly useful in examining hydrothermal injection. FVCOM utilizes a triangular structure within each layer to capture a spatially variant topography, such as the topographically complex ridges of Endeavour Ridge valley. Another desirable trait of FVCOM is its modular nature. There are many different modules available to FVCOM, and as such it is highly adaptable to the task at hand.

An area large enough to set up the large scale flows which force fluid along and over the ridge was chosen, incorporating a high enough resolution to observe hydrothermal effects within the ridge valley. A triangular mesh was built using the Surface-water Modeling System (SMS) (Aquaveo 2020) which is a useful software package for constructing a variable triangular mesh. We defined the boundary as a large stretched oval shape encompassing as much of the ridge system as possible. The spacing between nodal points on the boundary was set to 60 meters. Then the interior triangles within the ridge valley were selected visually and manually increased in resolution to a spacing of approximately 20 meters (see Figure 4.2). This creates a large domain having a high resolution within the region of most

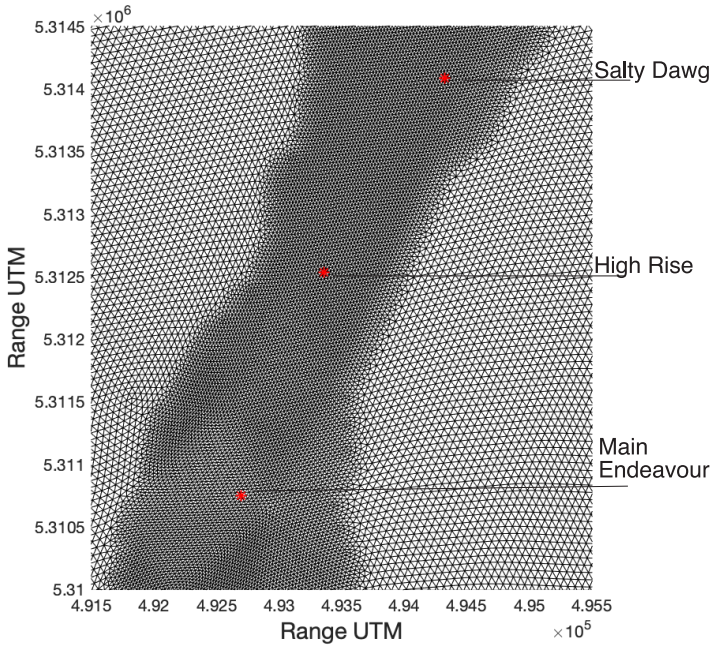

Figure 4.2: FVCOM mesh is shown centered on the three middle venting fields within the Endeavour Ridge Segment. These venting fields are (from south to north): MEF, High Rise, Salty Dawg.

interest, without utilizing an inordinate amount of computational time. There were a total of 152,157 nodes and 302,408 triangular elements in the mesh. Bathymetry with a 30m resolution were taken from Kelley et al. (2015), and mapped onto the mesh through the SMS scatter set interpolation tools (see Figure 4.3). This mesh resolution is sufficient to resolve some of the vent field features without needing more computational resources.

A terrain following sigma coordinate system was chosen for the vertical spacing. A 10m vertical resolution over the first 30 m above bottom is then increased incrementally by 15, 20, 30, 40, 50 and 60 m resolution until 400 m above bottom is

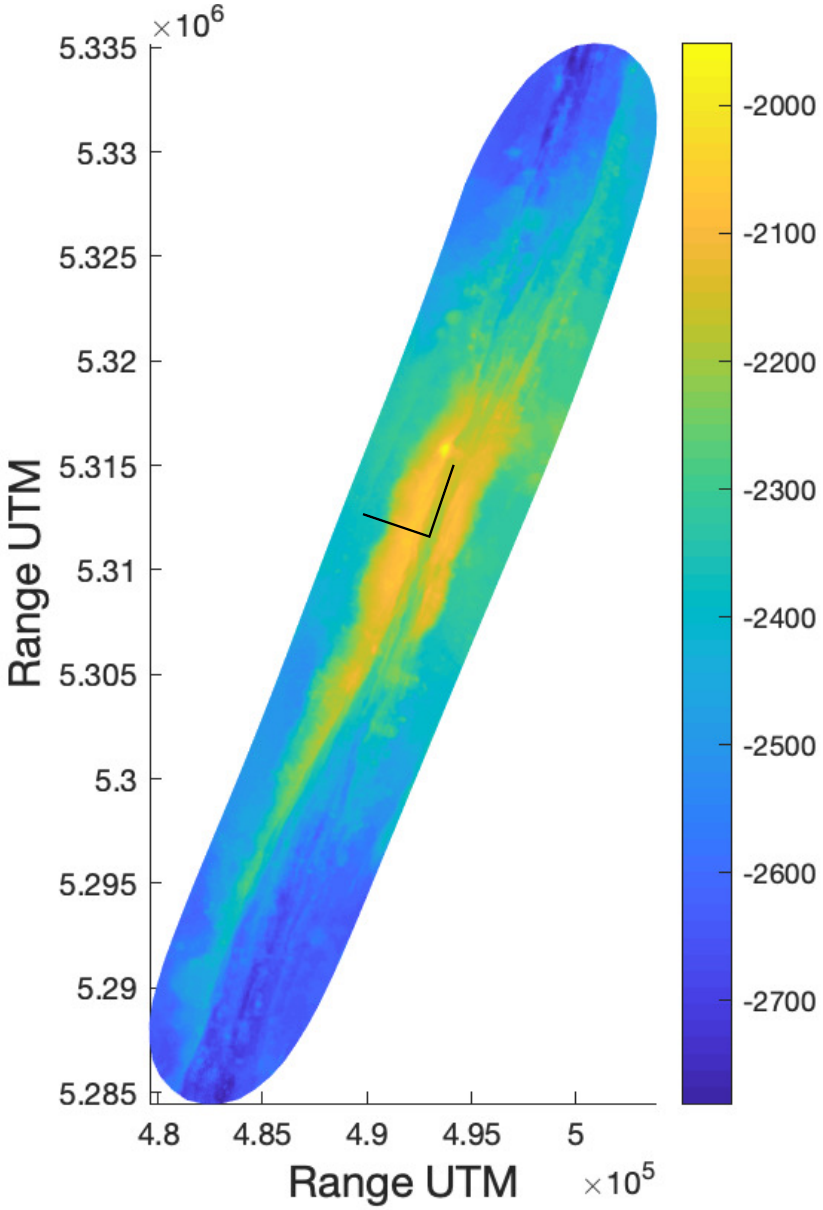

Figure 4.3: The full FVCOM domain bathymetry is presented. Axies are shown for along and cross valley directions where northward (along valley) and westward (cross valley) flows are positive

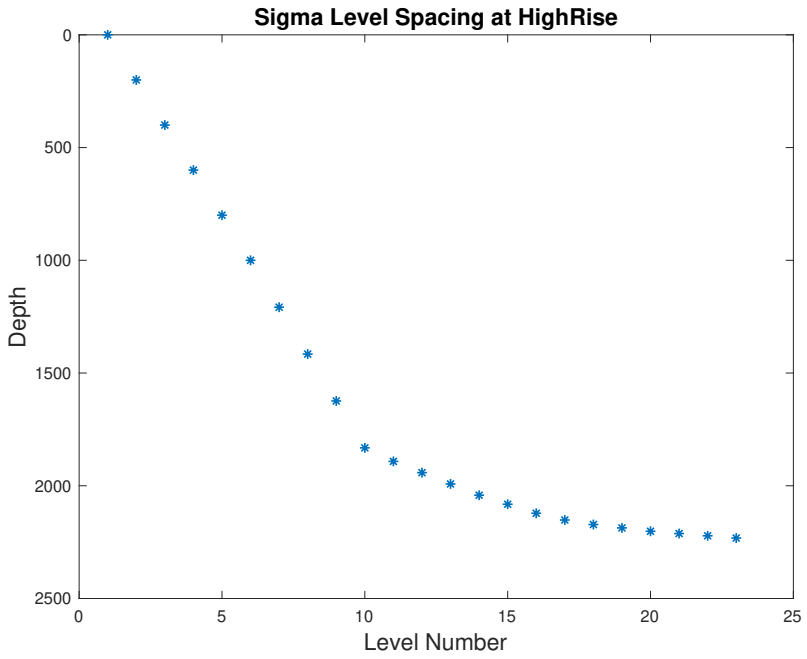

Figure 4.4: The sigma levels are shown near the location of High Rise

reached. At shallower surfaces the resolution is further decreased to 200 m. The sigma level terrain following coordinate was another valuable facet of the FVCOM program (see Figure 4.4). This vertical coordinate system allows for levels to be specified in relation to the bottom topography, while maintaining the same number of levels throughout the water column. This allows us to use a high resolution near the bottom (the area of interest), without the need to resolve the entire water column in high detail.

Tidal sea surface heights were used along the boundary to generate flows throughout the domain. The Tidal Model Driver (TMD) software (Padman and Erofeeva 2004) was used to generate a spectral tidal forcing file for each of the open

Table 4.1: Tidal boundary forcing at sample boundary node

tide	amplitude (meters)	phase (degrees)
S2	0.883	240.8
M2	0.258	270.5
N2	0.183	216.0
K2	0.067	263.6
K1	0.415	242.9
P1	0.257	227.7
O1	0.129	240.6
Q1	0.045	221.1

boundary nodes. This forcing file incorporates the amplitude and phase of tidal constituents chosen to emulate the tidal heights experienced at every boundary point at any given time. Within the ridge, the main drivers of the oscillatory currents are due primarily to K1, O1, M2, S2 tides (Thomson et al. 1990). The TMD and FVCOM spectral tidal forcing allows eight tidal constituents: S2, M2, N2, K2, K1, P1, O1, and Q1, and the amplitude and phase for each are shown in Table 4.1 for a node on the open boundary. It should be noted that by using the tidal constituents to force the model, the start times are relative. To avoid unwanted reflected signals from outgoing surface gravity waves at the open boundary, we utilize a sponge file coefficient of 0.08 over a distance of 750 meters from the boundary.

Wind forcing is chosen to be spatially constant and temporally varying. This is due to the low spatial resolution of wind forcing data that is available for the region of the Endeavour Ridge Segment. Data was taken from the National Centers for Environmental Protection (NCEP) Reanalysis database (Kalnay et al. 1996) for the year of 2018. This year was chosen due to the relative completeness of the

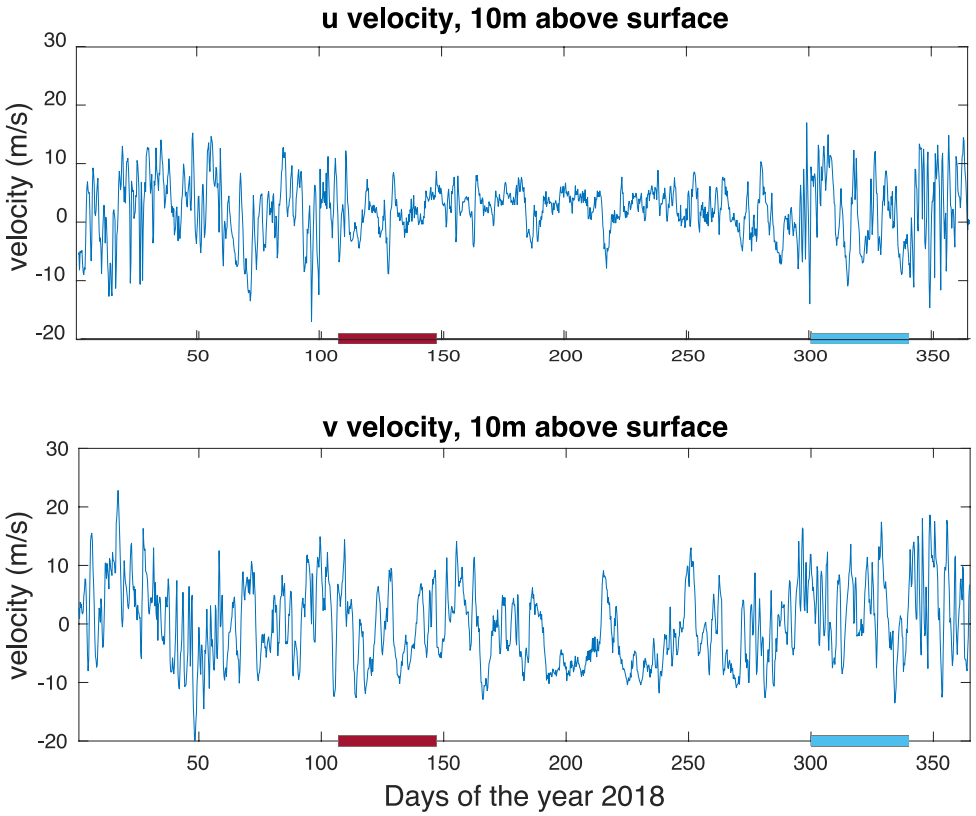

Figure 4.5: A yearly time series for the eastward (u) and northward (v) wind velocities at the Endeavour Ridge, using oceanographic wind conventions. The 40 day winter time series spans days 300-340 (October 28th - December 7th), while the summer winds span days 107-147 (April 17th - May27th)

temporal data set. From this dataset, two 40 day time series of 10m elevation wind were extracted for summer and winter. This was done to see if winds have any effects on the currents. Figure 4.5 shows the North-South and the East-West velocities for 2018 using oceanographic wind conventions. These time series show that there is more variability during the winter, with wind speeds up to 15 m/s.

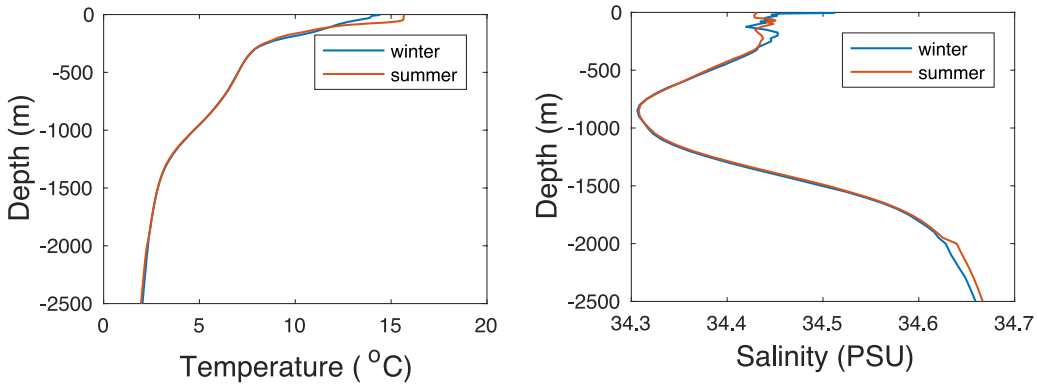

Figure 4.6: Temperature and salinity profiles for the Endeavour Ridge Region obtained from the WOA online database, corresponding to Summer and Winter time.

Within the domain of our model, a realistic set of initial conditions for temperature and salinity profiles for the region were obtained from the World Ocean Atlas (WOA) (Boyer et al. 2013) online database. The data from WOA is comprehensive, but when compared to the resolution of our FVCOM mesh, the available resolution is very coarse. Therefore, only one profile of each temperature and salinity was used to represent the stratification throughout the region for winter and summer runs (see Figure 4.6). These profiles were then interpolated to the sigma levels of the model at each node.

The ground water module within FVCOM was used to simulate the hydrothermal contributions of venting regions. This module requires the input temperature and volume flux to produce fluid sources at specified nodes. To represent each vent field, a set of seven nodes was selected to cover a roughly circular area of

approximately 40m in diameter. The heat transport and maximum temperature observed for each field was obtained from the InterRidge database (Beaulieu and Szafranski 2018). This InterRidge database also provides the maximum temperature observed at each vent field. In order to account for both focused and diffuse flow, an outflow temperature of 1/10th the maximum temperature was selected. The total volumetric transport of each vent field based on the temperature anomaly and the estimated heat transport for the hydrothermal field is given by:

$$V = Q/(\delta T \rho C_p) \tag{4.1}$$

where Q is the heat transport at the venting site, δT is the temperature difference between the source and the ambient fluid (having a background temperature of $2°C$), C_p is the heat capacity, and ρ is the fluid density, such that $\rho C_p = 4 \times 10^6 J/(m^{3\circ}C)$ is constant. The calculated volumetric transport was then divided by the total number of nodes in the field to obtain a volumetric flux at each of the 7 vent field nodes. Doubled venting uses the same volumetric flow and increases the fluid temperature by a factor of two, effectively doubling the heat transport by the venting fields. See Table 4.2 for a summary of values used for each vent field.

The external time step was set to 0.1 seconds, and the internal time step was set to 0.3 seconds. The model has a 10 day ramp-up period to setup tidal forcing throughout the region. The model starts data output after the 10 day ramp up, and writes data on an interval of 20 minutes. Velocities within the Endeavour ridge valley

Table 4.2: Vent field venting parameters

	Mothra	MEF	High Rise	Salty Dawg	Sasquatch
Heat Transport (Q)	300MW	650MW	390MW	100MW	50MW
Volumetric Flow per node	$0.36m^3/s$	$0.61m^3/s$	$0.43m^3/s$	$0.11m^3/s$	$0.07m^3/s$
Venting temperature	$32°C$	$40°C$	$34°C$	$33°C$	$29°C$
Doubled Heat Transport (Q)	600MW	1300MW	780MW	200MW	100MW
Volumetric Flow per node	$0.36m^3/s$	$0.61m^3/s$	$0.43m^3/s$	$0.11m^3/s$	$0.07m^3/s$
Doubled Venting temperature	$64°C$	$80°C$	$68°C$	$66°C$	$60°C$

are examined as along and cross valley velocities. To obtain these values, the East-North velocities were rotated through 71 degrees in order to line up with the valley (see coordinate axes in Figure 4.3). The along valley velocities correspond to the new x coordinate, positive in the northeast direction. The cross valley velocities correspond to the new y coordinate, positive in the North-west direction.

Several model runs were carried out using the forcing described previously, and consist of several different trials to allow for comparison in order to determine the effects of hydrothermal venting on flow circulation within the ridge valley, as well as how these influences differ under different venting patterns. The runs carried out are as follows: 1) no venting reference case, 2) normal venting under winter winds, 3) normal venting under summer winds, and 4) doubled venting under winter winds. Each of these model runs are summarized in Table 4.3. The no venting run serves as a baseline comparison to the other venting runs in order to extract all the effects that were due to the vent field influence. This is done by removing the calculated flows within the no venting case from those in the venting case.

Table 4.3: FVCOM model runs

	Venting Regime	Winds
Exp 1	No Venting	Winter winds
Exp 2	Normal Venting	Winter winds
Exp 3	Normal Venting	Summer winds
Exp 4	Doubled Venting	Winter Winds

4.3 Results

The FVCOM simulations of the Endeavour ridge system with the no venting case is described first in order to characterize a baseline for the flows through the Endeavour Ridge valley. Residual velocity anomalies are then examined for the other cases, in order to characterize the velocity behaviour that results from hydrothermal flow modulation. In each section, a series of horizontal flows at constant characteristic depths (as shown in 4.7) is investigated: 2173m is within the valley but blocked by a sill in the north end; 2100m is within the axial valley above the northern sill; 1800m is above the ridge flanks; and 1300 is above the depth of neutral buoyancy. Then the along and cross valley velocities on the axial valley transect is examined. Finally a focused analysis at the High Rise vent field will be examined superimposed over the temperatures at that location.

The model displayed a loss of temperature at the open boundary as can be seen in Figure 4.8. In order to display a more realistic picture of the temperature near the hydrothermal vent fields, this loss is corrected. At each time step, a discrepancy profile was calculated for temperature by taking the difference of the

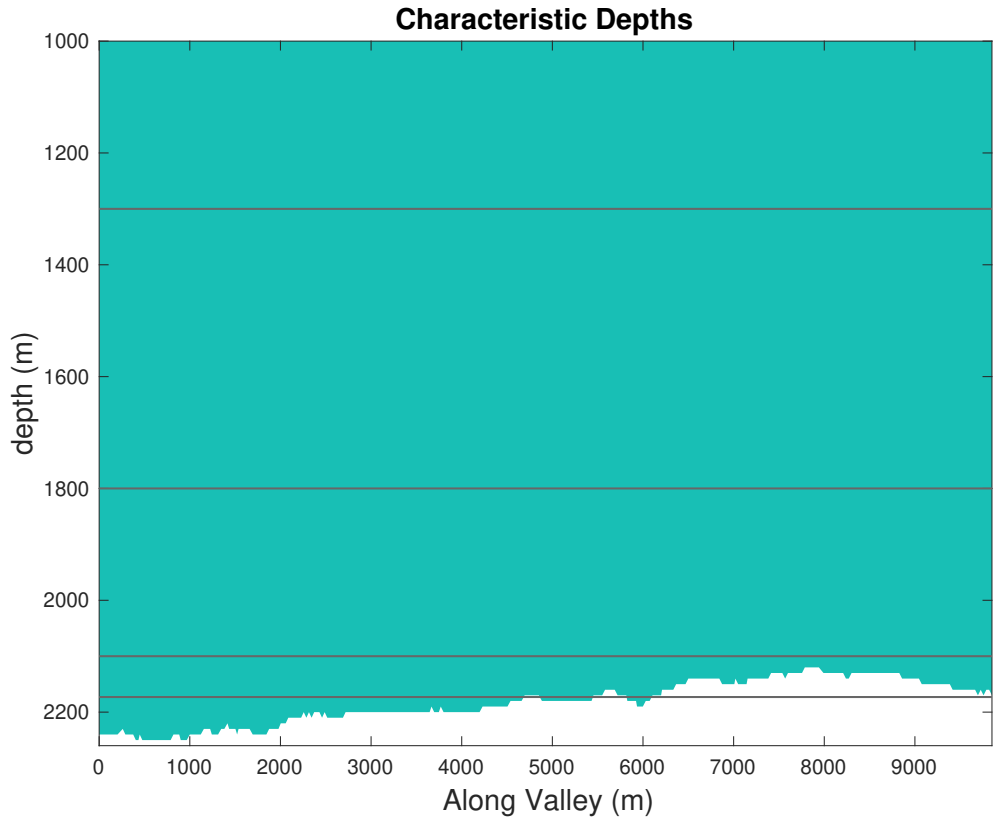

Figure 4.7: Characteristic depths were chosen for the examination of the cross sectional flow patterns. The lines represent the cross-sectional depths that are used to examine the constant depth residual horizontal velocities. These depths are located at 2173m, 2100m, 1800m, and 1300m.

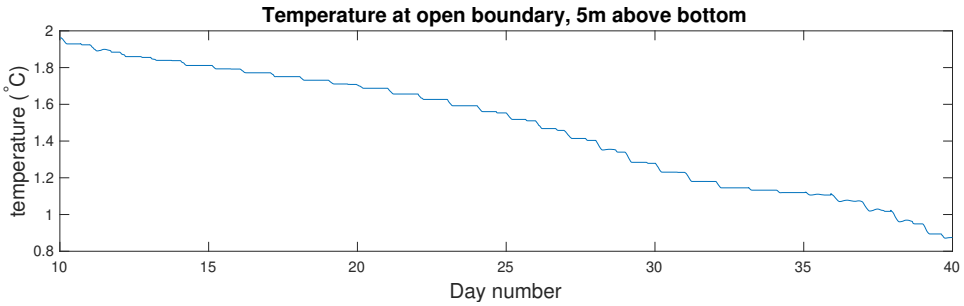

Figure 4.8: Time series of bottom temperature near the model boundary. The diminishing temperature is indicative of a heat loss to the boundary

initialization profile and the calculated temperature profile at a location near the boundary. This discrepancy profile represents the temperature that has been lost to boundary leakage at each depth. Then a 30 day average of this profile is taken, in order to provide the average discrepancy between modeled and initialized temperatures. This profile was then used to correct the temperatures at each depth within the domain at each node. Figure 4.9 shows the 30 day average discrepancy profiles for a node inside and outside the ridge valley.

Figure 4.10 shows the tides that result from spectral forcing along the boundary. As the tidal constituents were calculated from a reference day zero, they do not represent a specific time. However the tidal signal was compared to the sea surface heights for the SouthWest valley mooring for the year of 2018, and the best fit was found to be over the 30 day period shown. As can be seen, the model displays appropriate tidal behaviour for the region, even though there is not a perfect match due to differences in the phases of the tides in the model and those observed.

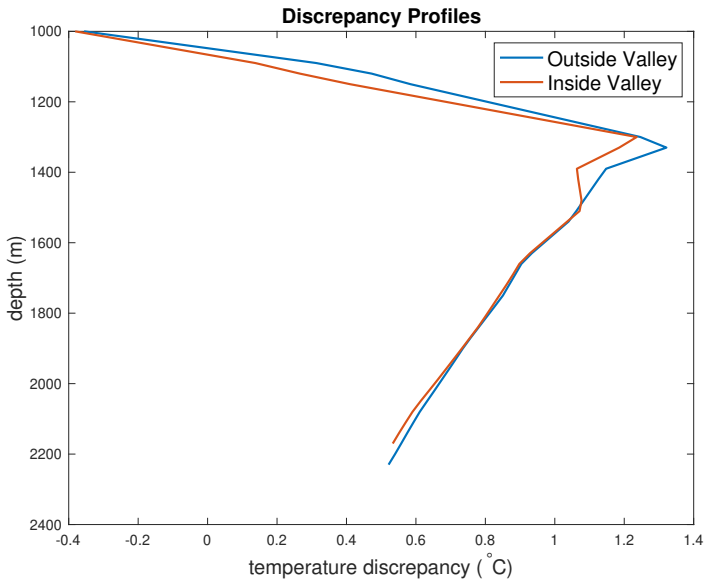

Figure 4.9: Discrepancy profiles averaged over 30 days, presented for both a point near the boundary and a point inside of the ridge valley

Flow Patterns: No Venting

Figure 4.11 shows the large scale residual flow (30 day average) in the Endeavour segment region as a function of depth. At 2173m depth, flows enter the axial valley from the south with speeds of approximately 5cm/s towards the northeast, with some flow visible on the northern end, but those flows are blocked by the sill northeast of the High Rise vent field. Above the valley but below the ridges at 2100m depth a more clear flow pattern can be seen to develop. Inflow velocities at both the northern and southern ends of the axial valley seem to converge in the central valley at High Rise and starts to be deflected ridgeward. Above the ridges at 1800m depth flows from the south are deflected eastward and flows from the North

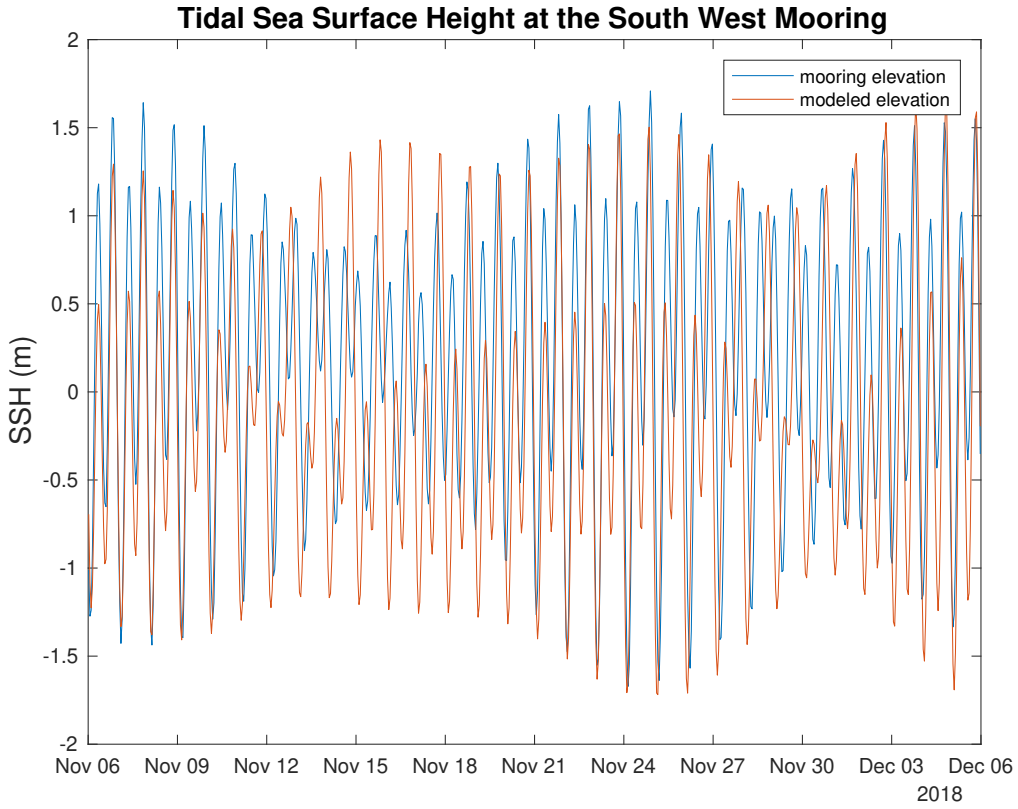

Figure 4.10: A sea surface height comparison near the Sourth West Mooring. Model results are shown compared to mooring data.

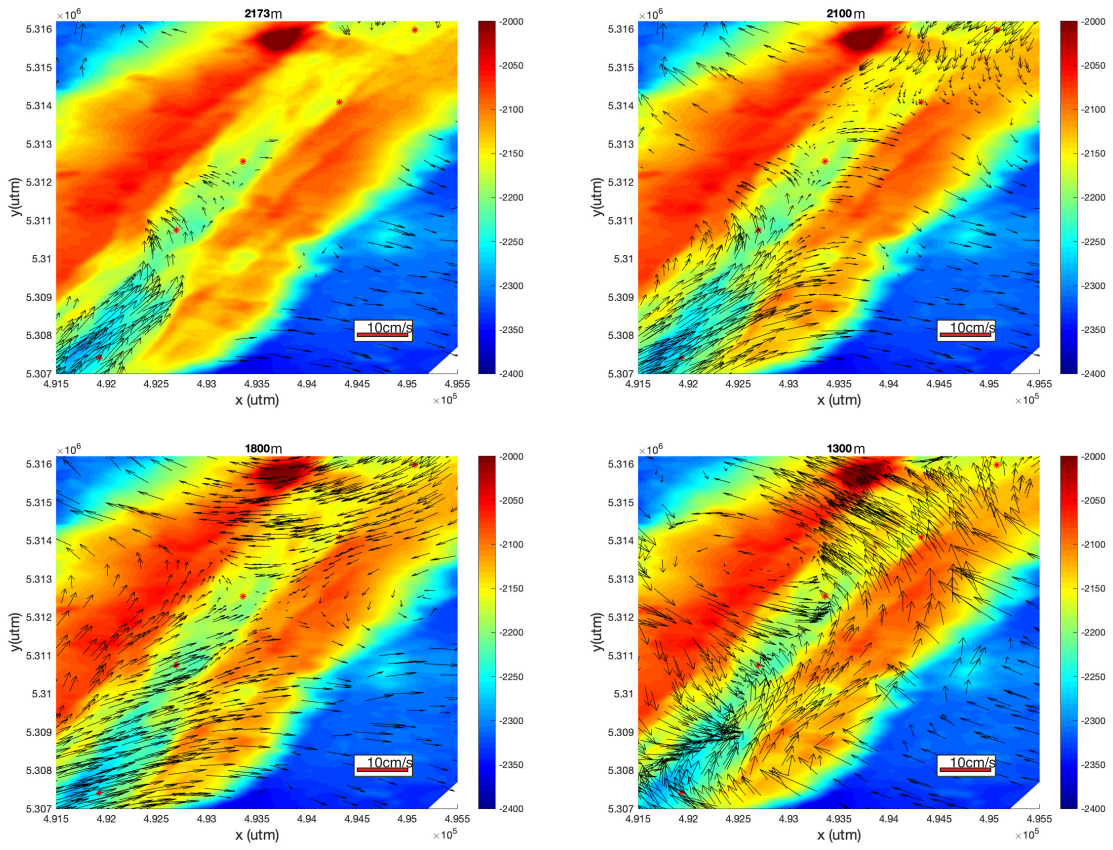

Figure 4.11: Depth dependent flow patterns throughout the ridge valley. Four different depths are displayed to characterize the flow under no venting conditions and winter winds.

are deflected westward. This residual flow is presumably caused by topographically steered flows. At 1300m depth, this cross ridge flow can be seen to result in a cyclonic circulation over the ridge system.

The along valley transects of velocities aligned with along, cross, and vertical directions are displayed in Figure 4.12. The transect of along valley velocities shows strong residual inflow magnitudes at the northern and southern ends of the ridge

valley that diminish as flows reach the central valley. This direction of flow persists above the ridge crest until at approximately 1200 m depth there is a reversal in the direction of flow on the northern end. This indicates the formation of a circulation cell that extends above the ridge system as the vertical velocities on the northern part are predominantly upward. The velocity magnitudes remain fairly consistent with height within the axial valley approaching speeds of 10cm/s in the southern end above the ridge. The decrease in magnitudes in the central valley is likely due to the interactions between converging water masses from the north and south.

Cross valley velocities along the axial valley are primarily focused above the ridge. The northern section has westward flows that are maximal at approximately 1250m depth and the southern section has eastward flows that are maximal at 1500m depth. This discrepancy in depth may be because the northern section is shallower compared to the southern section. Vertical velocities along the transect approach magnitudes as high as 4cm/s. There is strong upwelling observed in the southern region, followed by downwelling above. The vertical velocity also shows a two layer structure separated at approximately 1700 and 1200m depth that may correspond to the layering seen in both the along and cross flows.

The near bottom flow near the High Rise vent field will be examined in more detail because of its location in the central valley where residual flow conditions are weak due to the convergence of northern and southern flows. The residual flow vectors in the along-axis vertical plane with temperature contours at High Rise under no venting conditions is shown in Figure 4.13. The isotherms along the valley are

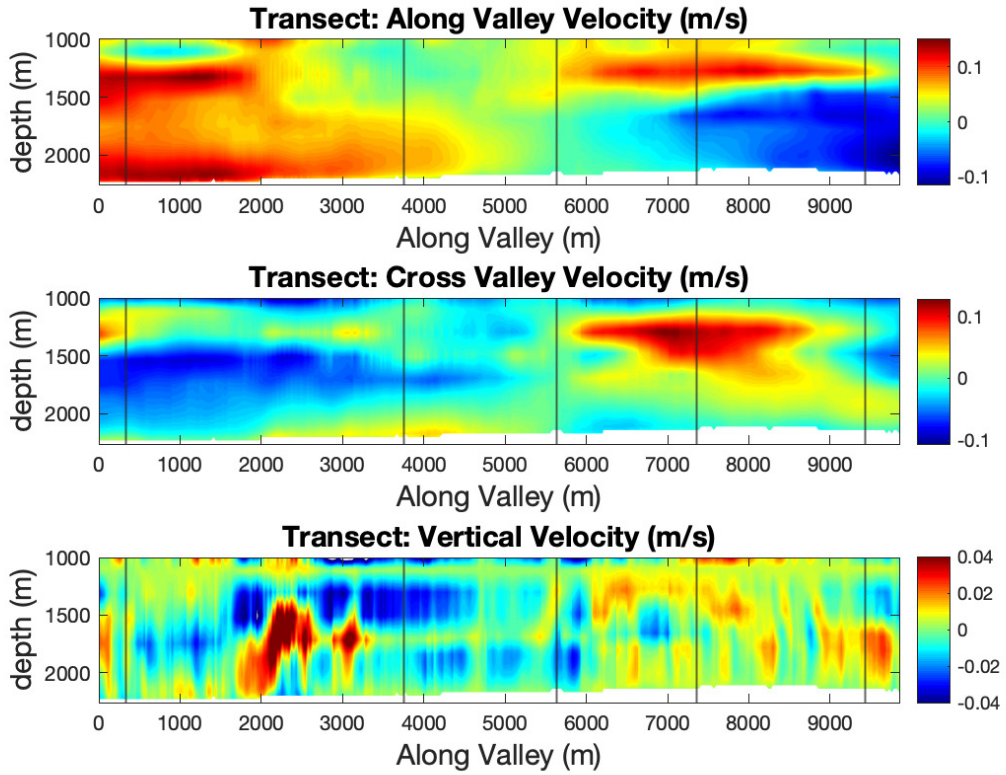

Figure 4.12: Residual velocities within the ridge valley transect intersecting the center of all five venting fields (vertical lines). The transects run from South to North and display along valley velocity (top figure), cross valley velocity (middle row), and vertical velocity (bottom row). Along axis velocities are positive towards the North-East, cross axis velocities are positive toward the West, and vertical velocities are positive upward. This transect represents velocities calculated under conditions of no venting.

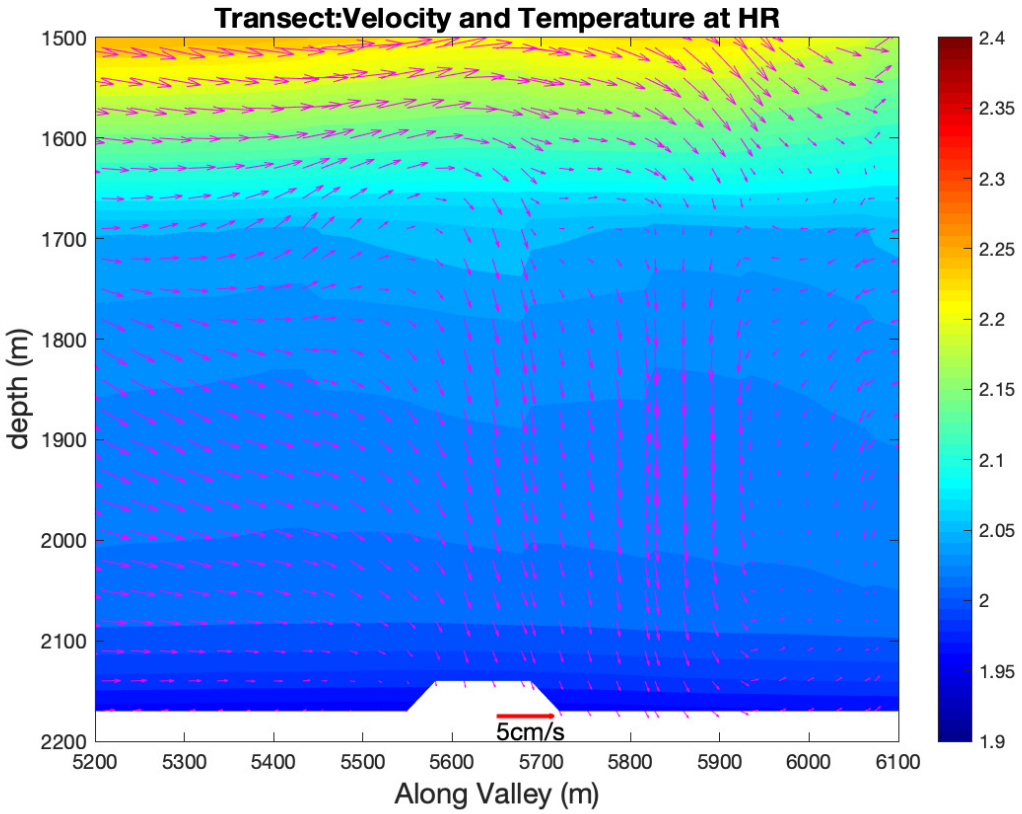

Figure 4.13: Along valley circulation patterns at High Rise are calculated under conditions of winter wind and no venting. The transect runs from the south end of the valley to the north, and is shown superimposed over temperature ($^{\circ}C$)

horizontal for the most part except where the vertical flows are downward over the High Rise field causing a sloping of the isotherms.

Figure 4.14 shows the cross ridge transect of the cross axis vertical velocities over the High Rise venting field. Here the topographically forced flows are forced over the ridges out of the valley for all depths. Within the valley, flows downwell.

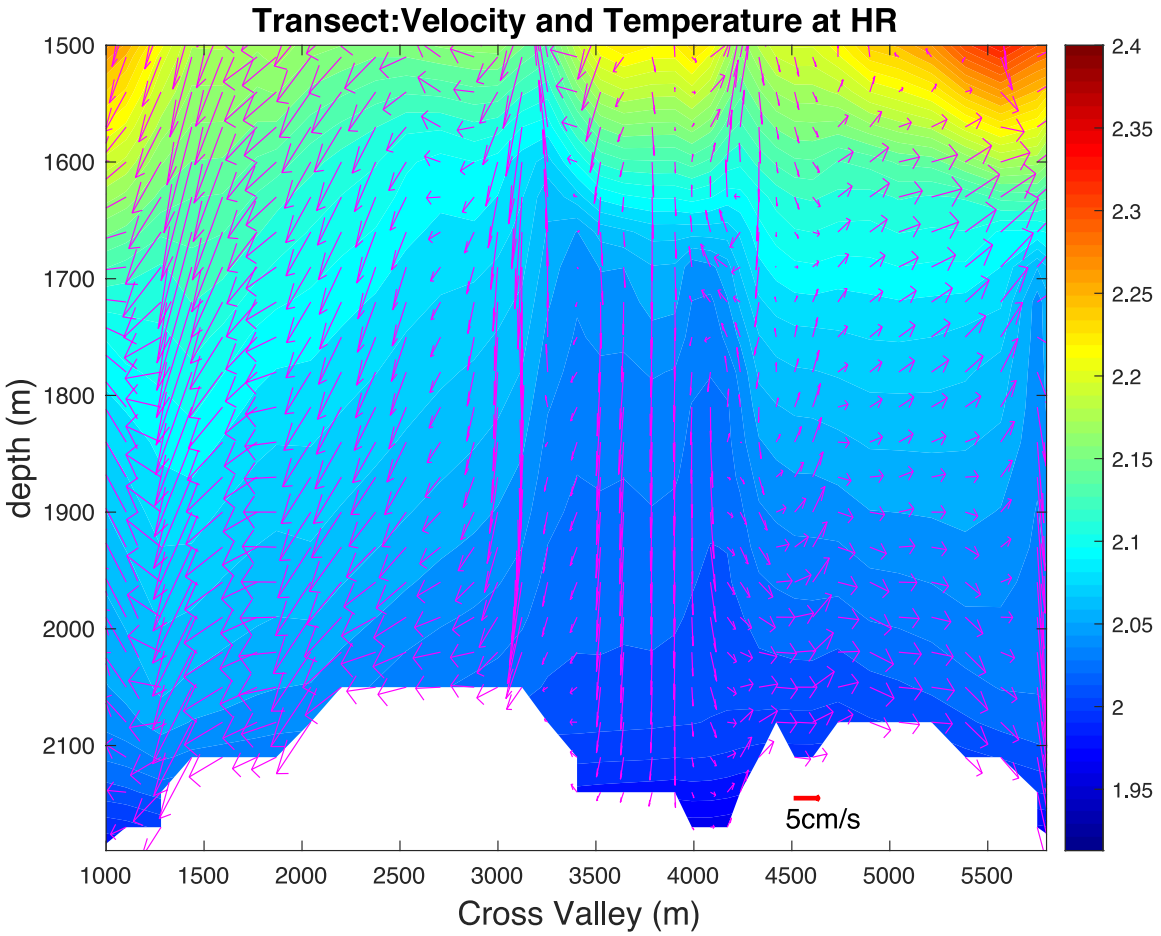

Figure 4.14: Cross valley circulation patterns arising at High Rise are calculated under conditions of winter wind and no venting. The transect runs from West to East perpendicular to the axial valley, shown superimposed over temperature contours ($^{\circ}C$)

Venting Anomalies: Differences between Venting and No Venting

This section compares the velocities from the winter normal venting case to the no venting winter case. The velocities shown are the differences of 30 day averaged residual velocities calculated at each element on the mesh. Since the venting causes subtle changes, differences are shown.

Figure 4.15 shows the horizontal velocities that result from hydrothermal venting under conditions of winter winds. They are shown at the four standard depth levels defined in Figure 4.7 . The hydrothermal vent fields are marked by red asterisks within the domain. Deeper than the northern sill at 2173m, hydrothermal venting causes velocities up to 3 cm/s. Larger flows to the east can be seen to occur just south of High Rise, the central vent field. At 2100m depth above the northern sill, the inflow velocity is enhanced by 3 cm/s at the northern entrance of the ridge valley. In addition, on the south end of the eastern ridge, flows of 3cm/s can are directed over the ridge to the east. Just above the ridge depth at 1800m depth, the velocity anomaly is directed toward the south and is not bound by the ridges, and so is not focused within the valley. Well above the ridge system at 1300m depth strong cross ridge flows of larger than 3cm/s develop, presumably a result of the vent induced flows interacting with regional currents and topographical forcing. From these flow patterns, the velocity anomalies can be seen to indicate that there is an increased flow from the presence of vent fields within the valley, that is further topographically forced through the region.

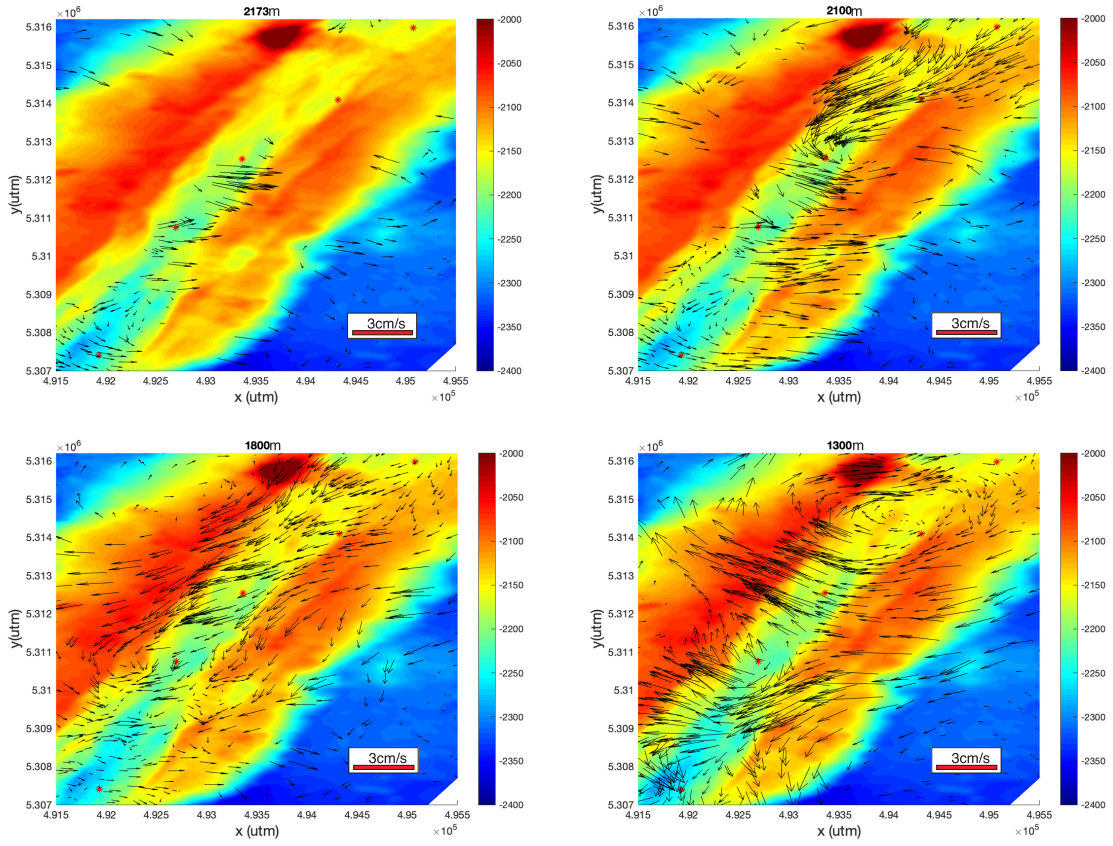

Figure 4.15: Depth dependent flow anomalies are displayed throughout the ridge valley. Anomalies are calculated as the difference between the standard venting and the no venting cases. The hydrothermal vent fields are marked by red asterisks within the domain.

Figure 4.16 shows the along valley transect of the velocity anomalies along, across and in the vertical direction. The transect passes through each of the ventfields, the locations of which are represented by vertical black lines. The along valley velocity is enhanced southward for much of the near bottom flows in the northern section of the axial valley, with isolated pockets of northward flow. On the three southern vent fields (with the largest heat fluxes), there are increased near bottom northward velocities. This indicates that the presence of the vent fields creates a flow toward the field. The crossflow along the transect displays a patchy behaviour, with the strongest change in velocities occurring at a depth of 1300m near to the center of the vent field. This corresponds to the large horizontal flows that were seen to circulate over the ridges at this depth in Figure 4.15 above. Vertical velocities display interesting behaviour, especially above the three southern vent fields. Where these vent fields are located, the velocity anomaly can be seen to reach 4 cm/s with a clear signal. In addition, between these vent fields is typified by an increase in negative vertical velocities. Together, these effects suggest that the inclusion of multiple adjacent hydrothermal venting fields sets up a circulation pattern where fluid is entrained and transported vertically and then fluid between the vent fields is replaced by fluid from above. This is as would be expected, as the ridges precent the inflow of off axis fluid flowing in at depth.

Hydrothermally induced circulation cells that occur near the High Rise venting field are examined in Figure 4.17 with anomalous flows overlaid over temperature contours and the actual velocity vectors shown on the bottom graph. It

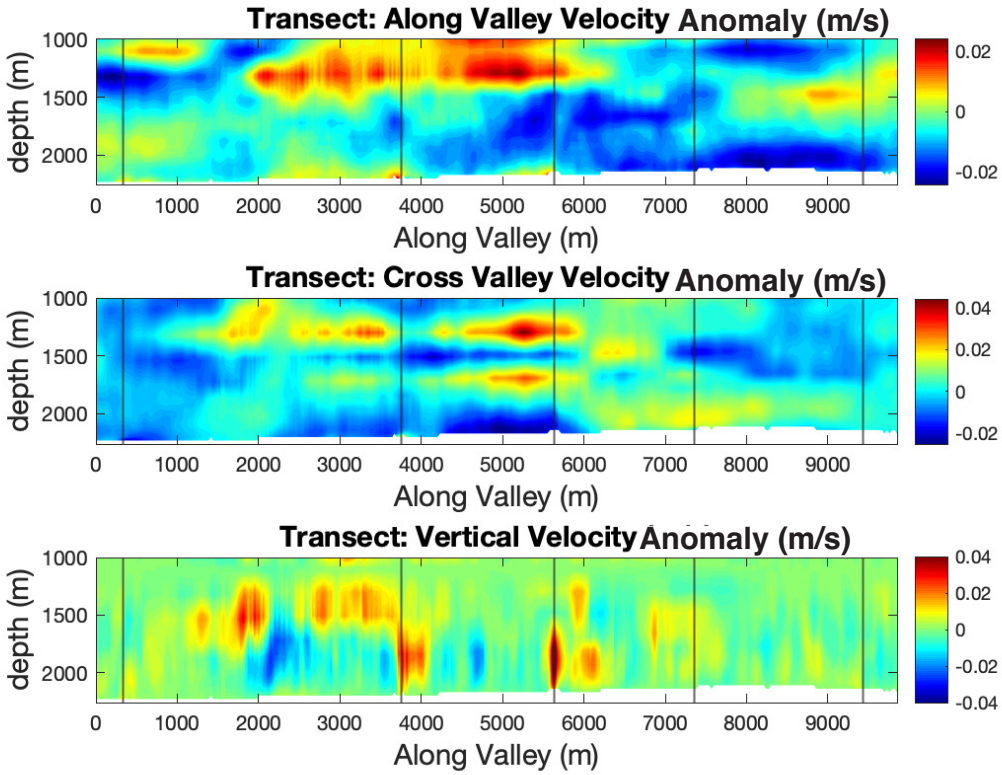

Figure 4.16: Residual velocity anomalies from venting and no venting experiments within the ridge valley transect intersecting the center of all five venting fields. The transects run from South to North and display anomalies for the along valley velocity (top figure), cross valley velocity (middle row), and vertical velocity (bottom row) components. Along velocities are positive to the right (towards the North-East), cross velocities are positive into the figure (toward the West), and vertical velocities are positive upward. Vent field locations are marked by horizontal lines.

can be seen that there is a circulation cell in the south focused near the valley bottom. Water at the bottom moves toward the hydrothermal vent field and is than carried upward and then the flow is deflected southward at 1700-1800 m depth. The temperature when compared to Figure 4.13 shows the 2°C layer expanded through the water column.

Figure 4.18 shows the anomalous cross valley flows along the transect perpendicular to the ridge valley and centered on the High Rise vent field. These velocities are a result of the inclusion of the venting interacting with the topographic steered flows. The most striking feature is the enhanced vertical velocities above the vent field. When compared to Figure 4.14, the temperatures show increased magnitudes above the vent field above 2°C through the water column.

Venting Anomalies: Differences between Doubled Venting and No Venting

Figure 4.19 shows the horizontal velocities that result from doubled hydrothermal venting under conditions of winter winds. The deepest depth of 2173m shows the continued presence of 3cm/s induced velocity anomalies in the central valley region, similar to those seen in the standard venting anomaly case from Figure 4.15. Above the northern sill at 2100m depth, stronger flows can be seen to develop in the northern section of the ridge valley. These velocities reach magnitudes greater than 3cm/s. Primarily the flows can be seen to enter from the north and flow through the ridge valley, and then deflect eastward over the side of the ridge. Just above the

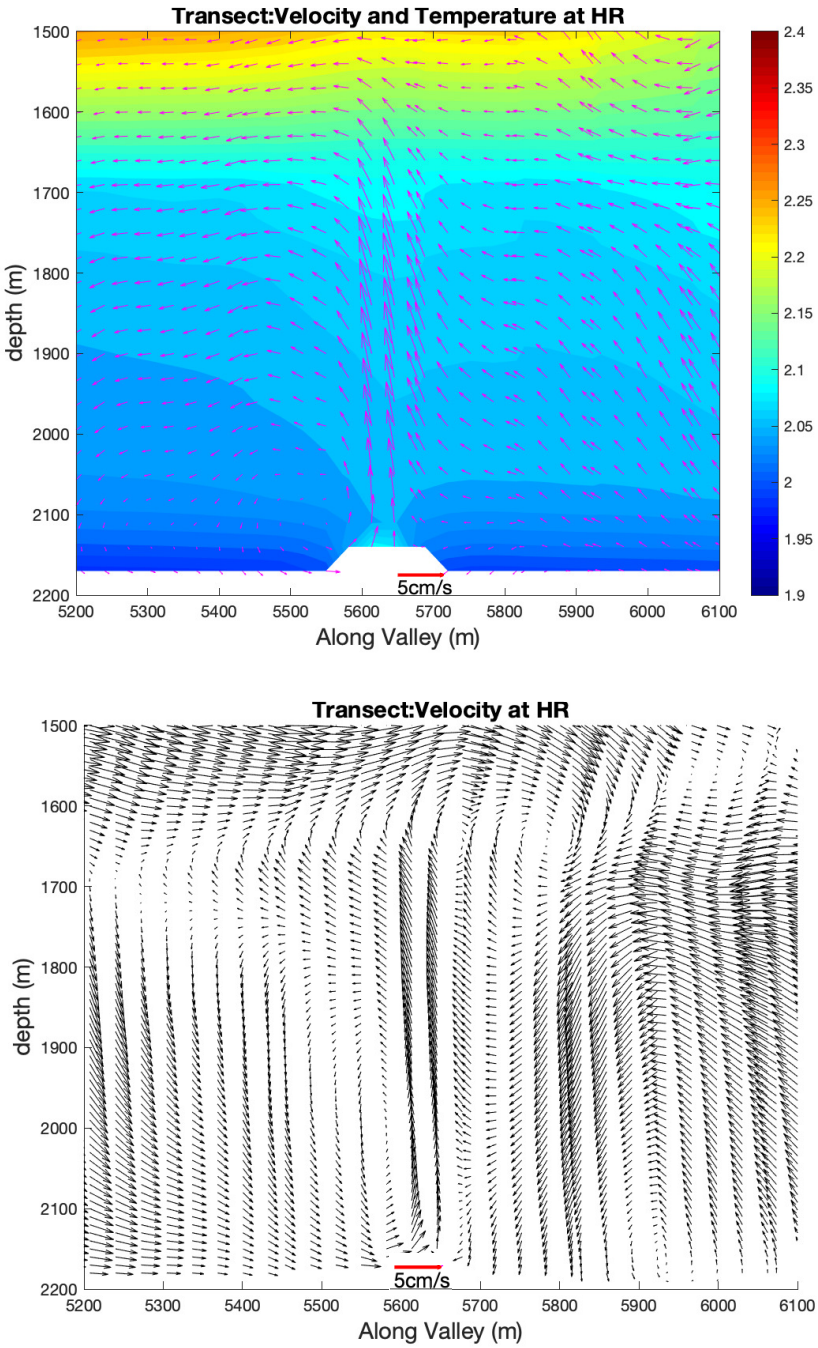

Figure 4.17: (Top) Along valley circulation anomalies at High Rise are calculated as a difference between the standard venting and no venting cases.The transect runs from the south end of the valley to the north, and is shown superimposed over temperature. (Bottom) The full (non-anomalous) velocities in the venting case are shown in black and white.

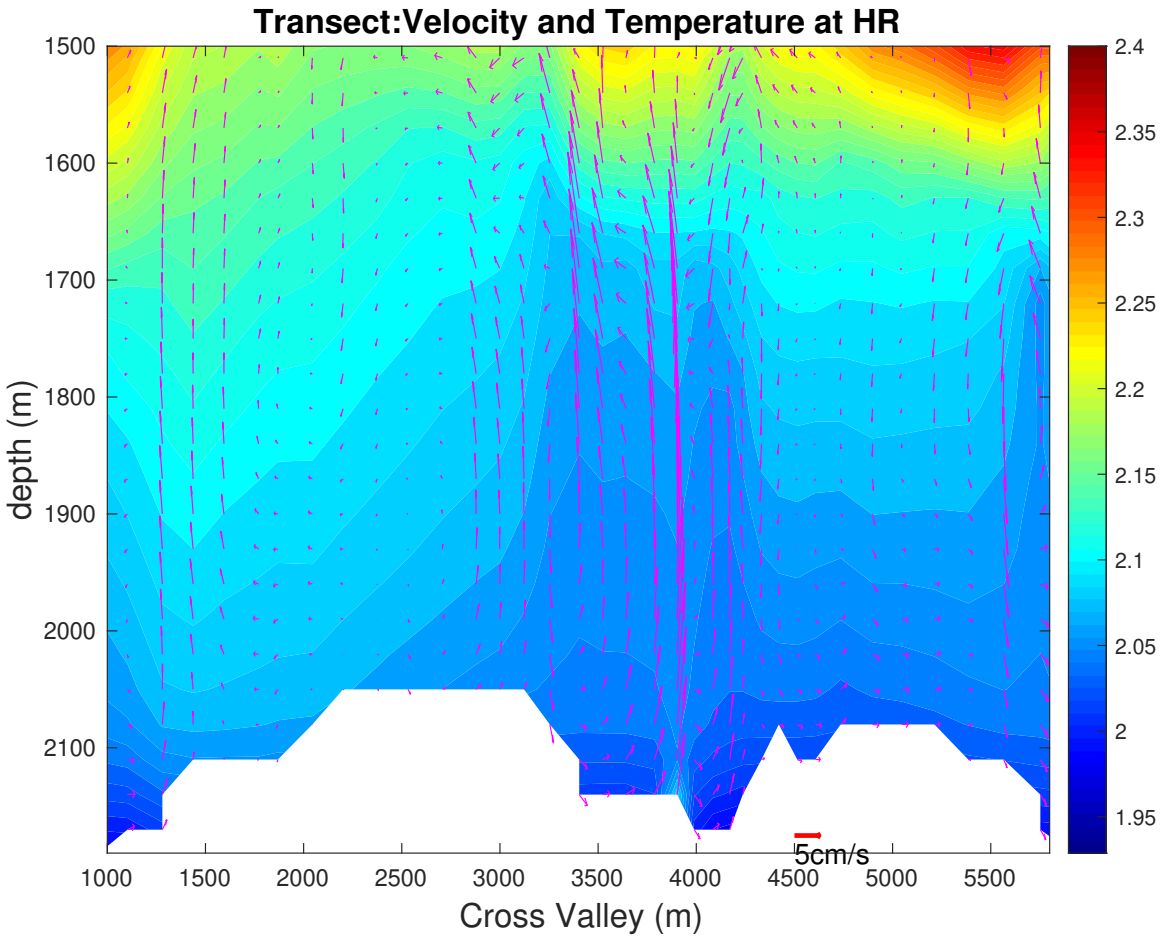

Figure 4.18: Cross valley circulation anomalies arising at High Rise are c alculated as a difference between standard venting and no venting cases. The transect runs from West to East perpendicular to the axial valley, shown superimposed over temperature ($^{\circ}C$)

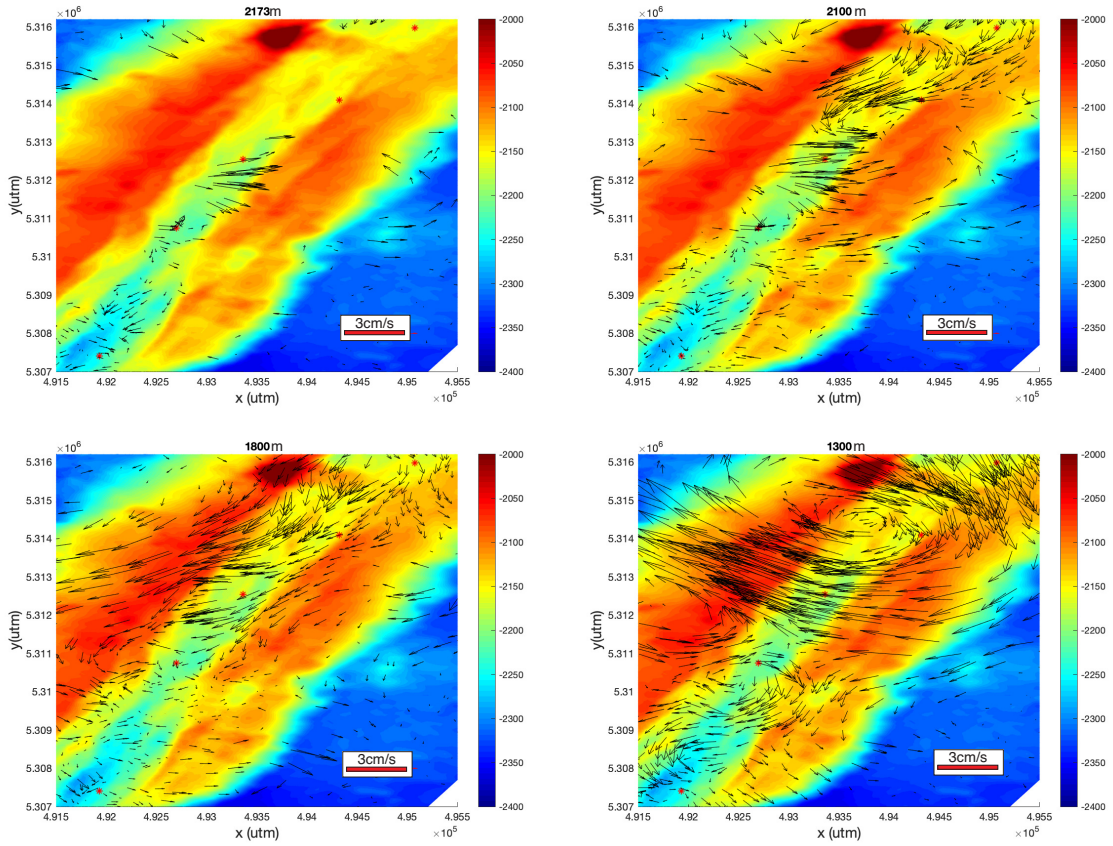

Figure 4.19: Depth dependent flow anomalies are displayed throughout the ridge valley. Anomalies are calculated as the difference between the doubled venting and the no venting cases. The hydrothermal vent fields are marked by red asterisks within the domain.

ridges at 1800m depth, the velocity anomaly shows a strong along valley flow towards the south and is distributed over the whole ridge like it was under standard venting conditions. Above the ridges at 1300 meters depth strong crossflows can be seen. These velocity anomalies can be seen to result in a large counter clockwise circulation pattern centered over the mid valley with a reduction in westward flows in the southern region.

Figure 4.20 shows the transect of velocity anomalies along the Endeavour ridge valley. The along valley velocity anomaly displays typically small negative values within the central transect of the valley between Main Endeavour and High Rise vent fields. This indicates that the Doubled venting results in an increased southward flow through the valley. In addition, near to the vent fields on the south side of the valley are increased horizontal velocity anomalies, indicating that hydrothermal venting is entraining the near bottom water at these regions. This is similar to what was shown in Figure 4.16, but here the magnitudes are larger. Crossflow velocities through the valley transect display a spatially diverse pattern with values varying about zero. Vertical velocity anomaly along the transect displays a large increase in velocity directly over the hydrothermal vent fields, particularly over the southmost three fields. These values are similar to these observed from the venting anomaly, but are of a greater magnitude and spatial region.

Figure 4.21 shows the velocity anomaly at the High Rise vent field. This region is typified by very large vertical velocities above the vent field as a result of the doubled heat flux for this case. This enhanced venting brings about very strong circulation cells on either side of the plume. The southern cell stretches from 1700m depth back to the bottom bathymetry, and reaches a horizontal width of 350 m. The northern circulation cell is centered higher up in the water column, cycling between 1500 and 1800m depth, and reaching a diameter of 300m horizontally. The temperature when compared to Figure 4.13 shows the 2.1°C layer expanded through the water column.

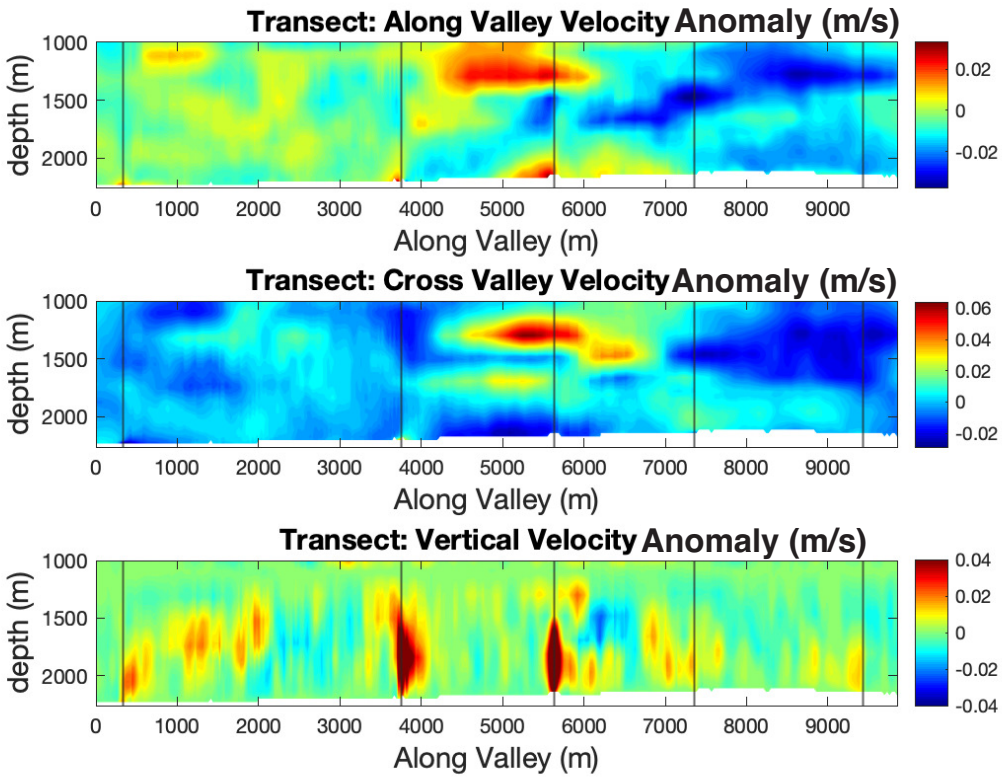

Figure 4.20: Residual velocity anomalies from doubled venting and no venting experiments within the ridge valley transect intersecting the center of all five venting fields. The transects run from South to North and display along valley velocity (top figure), cross valley velocity (middle row), and vertical velocity (bottom row) components. Along axis velocities are positive towards the North-East, cross axis velocities are positive toward the West, and vertical velocities are positive upward. Vent field locations are marked by vertical lines.

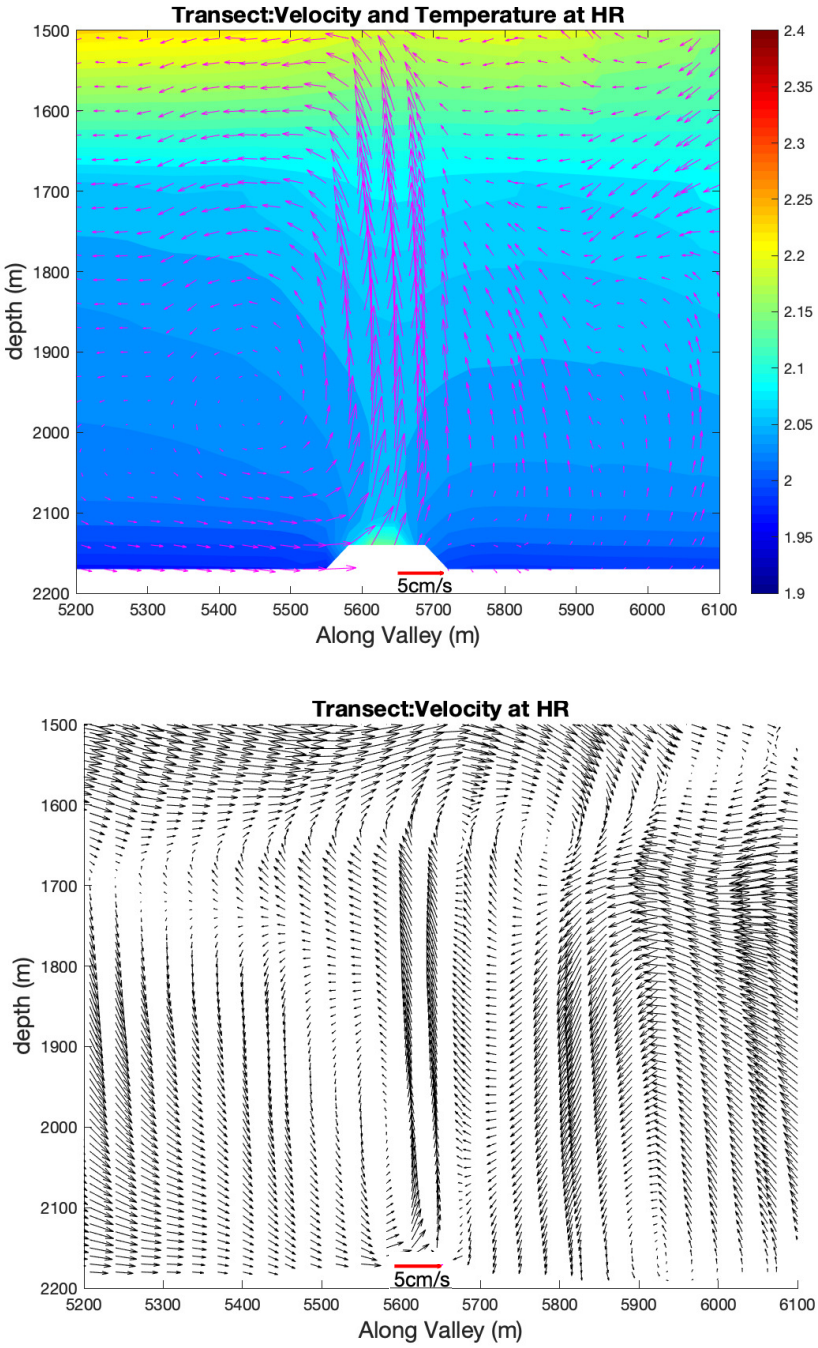

Figure 4.21: Along valley circulation anomalies at High Rise are calculated as a difference between the doubled venting and no venting cases. The full (non-anomalous) velocities in the doubled venting case are shown in black and white. The transect runs from the south end of the valley to the north, and is shown superimposed over temperature

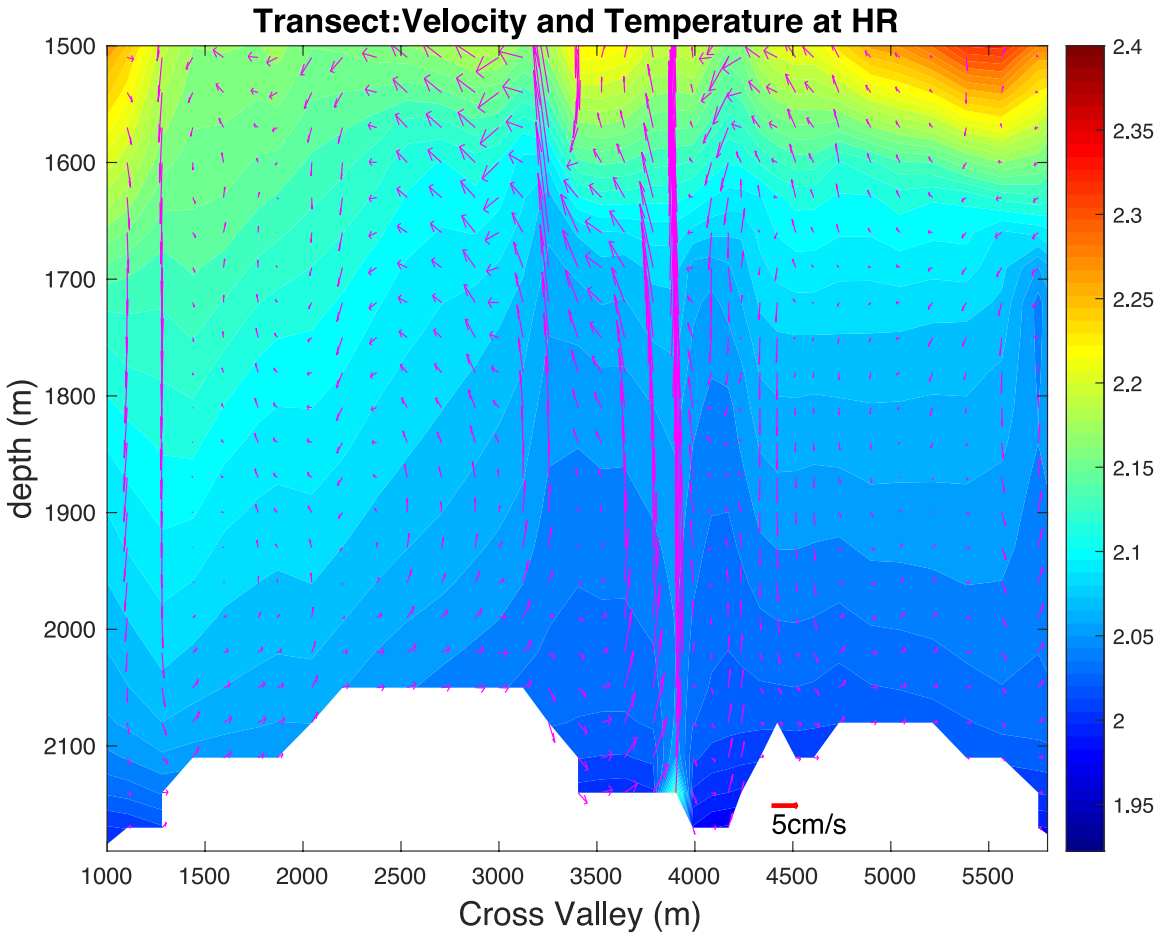

Figure 4.22: Cross valley circulation anomalies arising at High Rise are calculated as a difference between doubled venting and no venting cases. The transect runs from West to East perpendicular to the axial valley, shown superimposed over temperature ($^{\circ}C$)

Figure 4.22 shows the cross valley anomalous flows along the transect perpendicular to the ridge valley centered on the High Rise vent field with temperature contours. This figure displays a remarkable similarity to the behaviour of the venting-no venting anomalies seen in Figure 4.22, with strong vertical flows above the vent field causing hydrothermal circulation cells to develop.

Venting Anomalies: Difference between Winter and Summer Venting

This section compares the differences between the effects of Winter and Summer winds on the regional flow patterns within the Endeavour Ridge segment. Here the anomalies are taken to be the differences of 30 day averaged residual velocities calculated at each element on the mesh. The changing vent field between summer and winter was tested to see if near inertial or subinertial momentum could be observed. Also in the deep sea, near inertial internal waves propagate downwards to transfer energy at depth. However, spectral analysis of the data (as will be discussed in section 4.4) does not show any inertial oscillation captured by the wind forcing.

Figure 4.23 shows the difference of horizontal velocities calculated at constant depth levels chosen for the domain. Hydrothermal vent field locations are displayed as red asterisks. The scale of the differences are small, typically 2 cm/s or smaller throughout the domain, indicating no significant differences between the winter and summer wind driven cases. Due to these small differences in velocity from the summer and winter wind forcing cases, it can be determined that the flow of winds over the scale of domain used in this model do not result in any significant flow dependance on surface winds.

Figure 4.24 shows the difference in velocity behaviour on the along valley cross valley and vertical velocity transect of the Endeavour ridge. The along valley velocity can be seen to be predominantly southward, typically on the scale of mm/s. Cross valley velocities are similarly small, with magnitudes less than 2 cm/s. Vertical

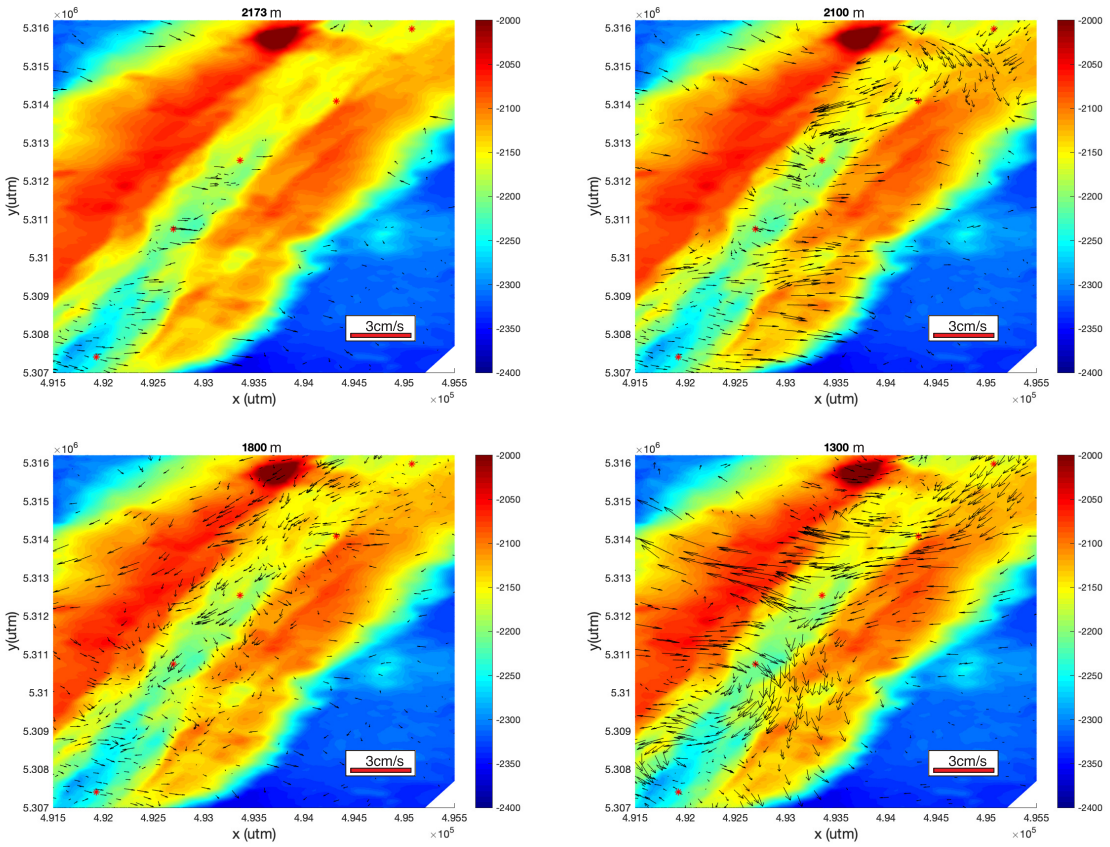

Figure 4.23: Depth dependent flow Anomalies are displayed throughout the ridge valley. Anomalies are calculated as the difference between the venting with winter wind and the venting with summer wind cases. The hydrothermal vent fields are marked by red asterisks within the domain.

velocities along the ridge transect can be seen to vary about zero, with minor variations up to two cm/s. Consistent with the horizontal flows through. the region that were seen in Figure 4.23, the transect velocities are small and suggest that the variations in winter and summer winds do not result in any significant alterations to flow within the valley.

Figure 4.25 shows the along ridge transect of the anomaly flow pattern near the High Rise venting field with the temperature background. The results here are consistent with the flow patterns observed previously, with near bottom velocities scattered and small, and velocities farther from the bottom more consistently southward.

Figure 4.26 shows the cross ridge transect flow patterns of velocity around the High Rise venting field. Similarly to Figure 4.26, the velocity anomalies between winter and summer winds do not seem to result in any clear differences in behaviour, with small patchy variations in velocity apparent through the region. Considering the low magnitudes seen in Figure 4.24, these winds do not seem to have a large impact on the flows within the ridge valley.

Summary of Results

There are several important observations that arise from our FVCOM studies of ridge-scale flow effects of hydrothermal venting: 1) There is strong topographical steering of tidally driven flows throughout the ridge valley; 2) Vent fields have a distinct influence on the flow parameters within the ridge system; 3) Results from

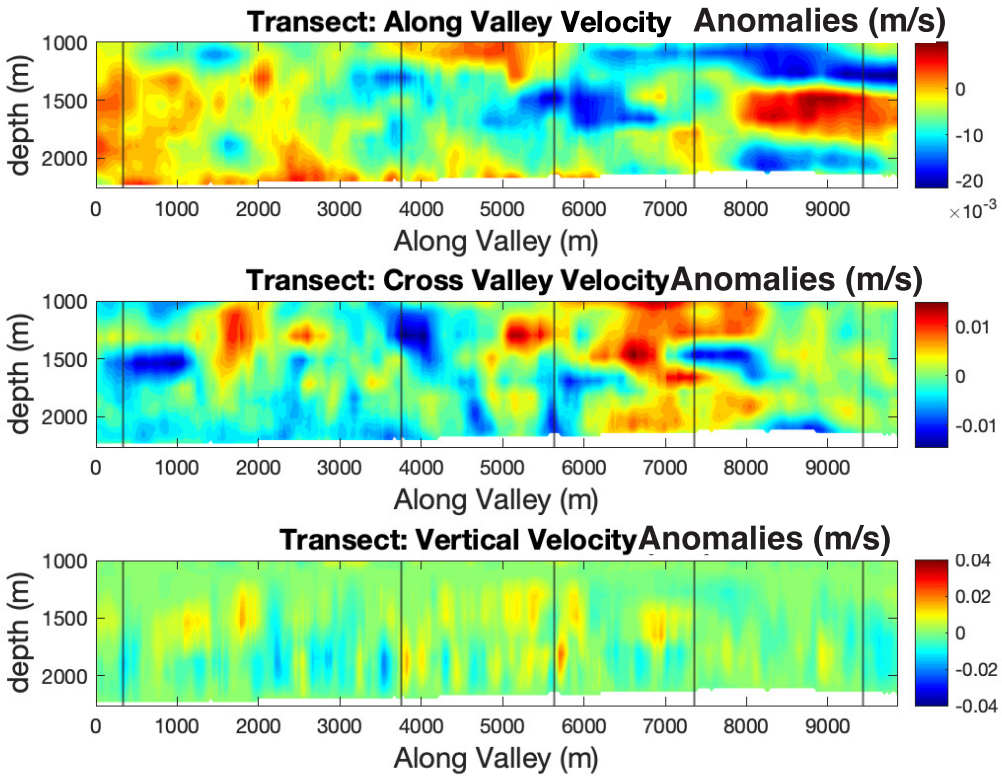

Figure 4.24: Residual velocity anomalies between winter and summer wind venting experiments within the ridge valley transect intersecting the center of all five venting fields. The transects run from South to North and display anomalies for the along valley velocity (top figure), cross valley velocity (middle row), and vertical velocity (bottom row). Along axis velocities are positive towards the North-East, cross axis velocities are positive toward the West, and vertical velocities are positive upward. Vent field locations are marked by vertical lines.

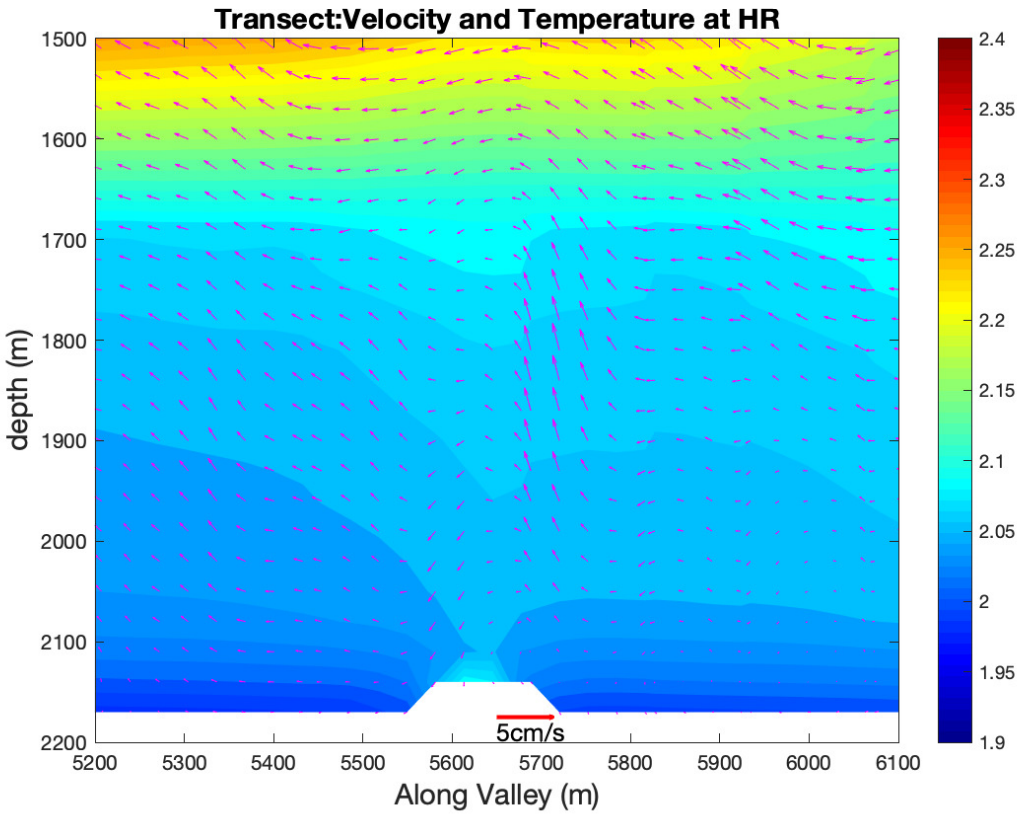

Figure 4.25: Along valley circulation anomalies at High Rise are calculated as a difference between the venting under winter wind and venting under summer wind cases. The transect runs from South to North, and is shown over temperature

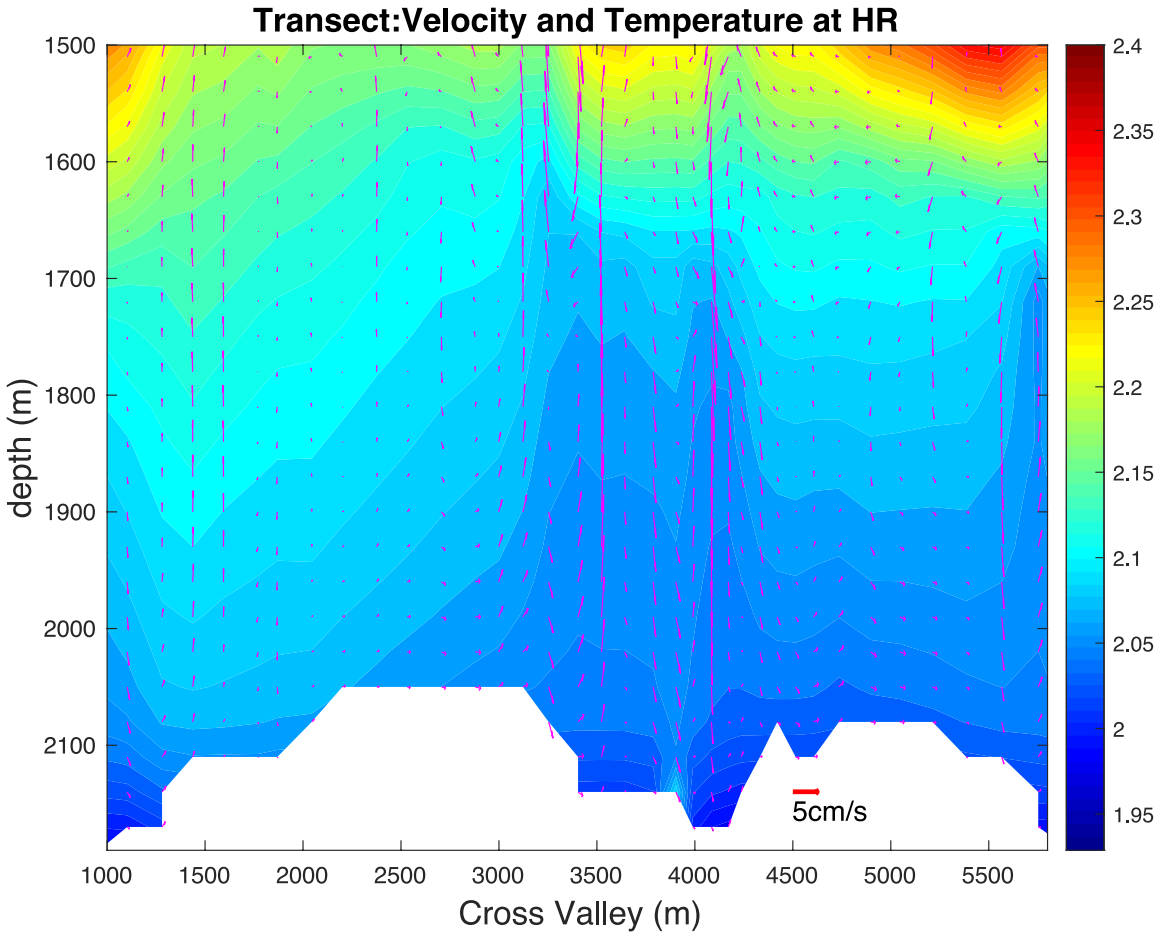

Figure 4.26: Cross valley circulation anomalies arising at High Rise are calculated as a difference between venting under winter wind and venting under summer wind cases. The transect runs from West to East perpendicular to the axial valley, shown superimposed over temperature ($^{\circ}C$)

both vertical velocity transects and 2D vector plots support the presence of vent driven circulation cells; 4) Vent driven circulation is best seen under conditions of weakest crossflow, i.e. in the central valley (particularly seen at High Rise); 5) The scale of these proposed circulation cell events is several hundreds of meters in diameter.

4.4 Nesting with the Hybrid Coordinate Ocean Model Data

The next phase of this modeling project is an exploratory use of model nesting in order to more fully incorporate the Endeavour Ridge segment regional dynamics into the model. This is a merged model scheme, where a low resolution mesh is utilized to force a high resolution mesh. This consists of applying boundary forcing across a domain much larger than our Endeavour Ridge domain to set up large scale inertial, geostrophic and generally any background ocean flows surrounding the Endeavour Ridge segment.

The outer boundary of the low resolution model was forced with Hybrid Coordinate Ocean Model (HYCOM) data (Halliwell 1998). The low resolution grid has a horizontal resolution varying from approximately 6 km on the outer boundary to 60 m on the high resolution boundary. The low resolution grid has 303400 centroids and 151778 nodes, while the high resolution grid has 302408 centroids and 152157 nodes as utilized in the previous experiment cases. Bathymetry for the low resolution model was obtained from Global Muliti-Resolution Topography Data Synthesis (GMRT) (Ryan et al. 2009) and has a spatial resolution of approximately

66m. This is seen in Figure 4.27. Similar to how the high resolution mesh was created, SMS was used to interpolate the bathymetry data to the low resolution mesh grid nodes. Bathymetry over the low resolution mesh was smoothed to improve the stability of the model. The strongest smoothing was applied to the boundaries, with lesser smoothing used near the Endeavour Ridge segment.

Rotary spectral analysis (see Figure 4.28) of observed current flows within the Endeavour Ridge valley show that inertial flows are both present and intermediate in magnitude to the diurnal and semidiurnal tidal flows. This figure shows the clockwise and counterclockwise velocity power spectral densities (vpsd) applied to observed u and v velocities at 125 meters above the bottom, taken from a mooring in the northwest part of the axial valley. The data over a year were converted into hourly data and a 10 day time window was utilized for both clockwise and counter-clockwise energy. The inertial period is located at a period of $0.67 days$ and a peak at this location can be seen in the figure. Peaks for the tidal periods can also be seen at 0.5 days (the semi-diurnal tidal period) and at 1.0 day (the diurnal tidal period).

The FVCOM model forced with tides and winds discussed previously does not include any inertial oscillation as shown in Figure 4.29. In this figure, similar 10 day periods of hourly data were used and 5 resulting spectra were averaged together. The semidiurnal and diurnal tides are evident, but there are no other signals.

The large domain model mesh is forced with four relaxation zones having a linear attenuation, and the model was run for 40 days of 2018 starting January 23rd, which corresponds to winter conditions. Surface elevation, salinity, temperature, and

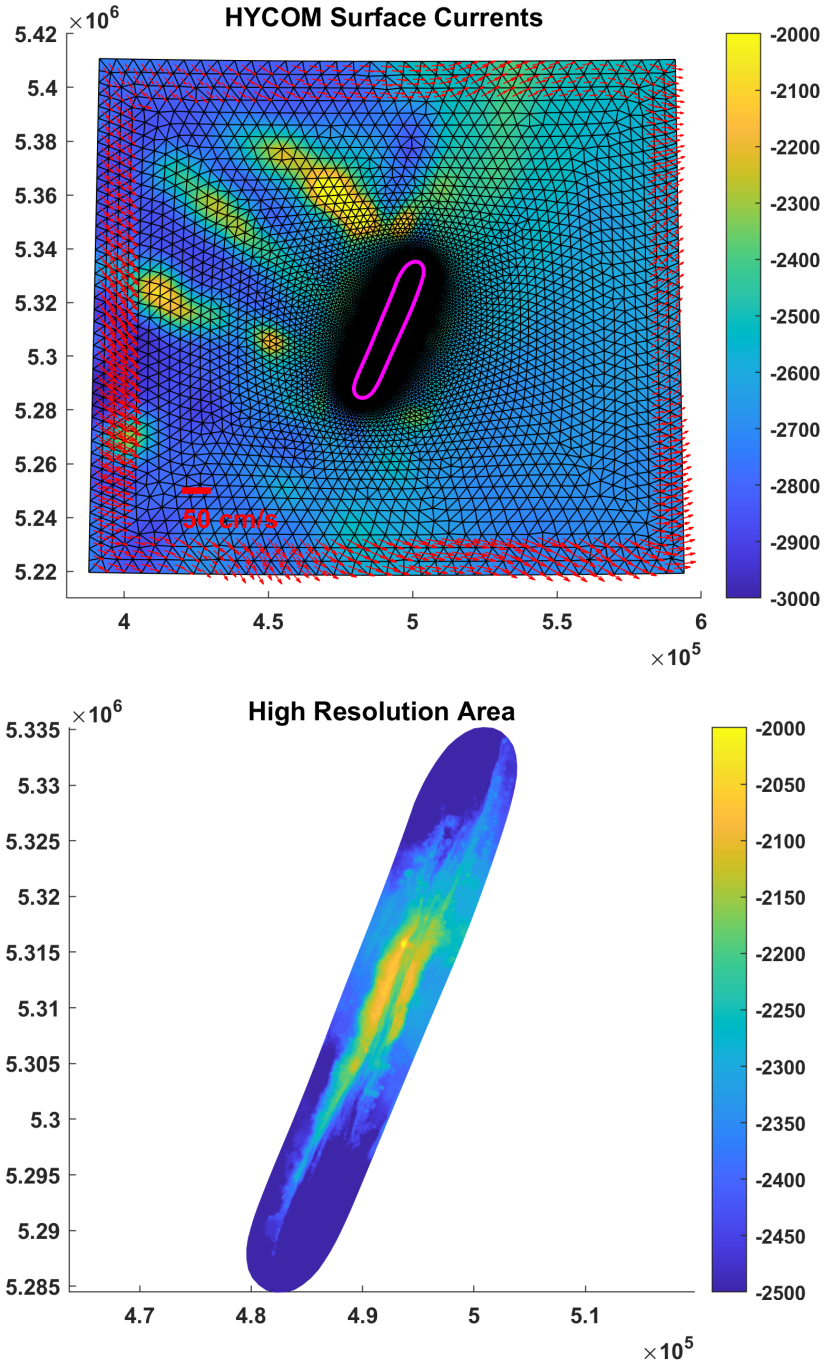

Figure 4.27: Low resolution model is forced via a four node three element relaxation zone on the outer boundary from HYCOM data. The high resolution nested domain is shown in magenta.

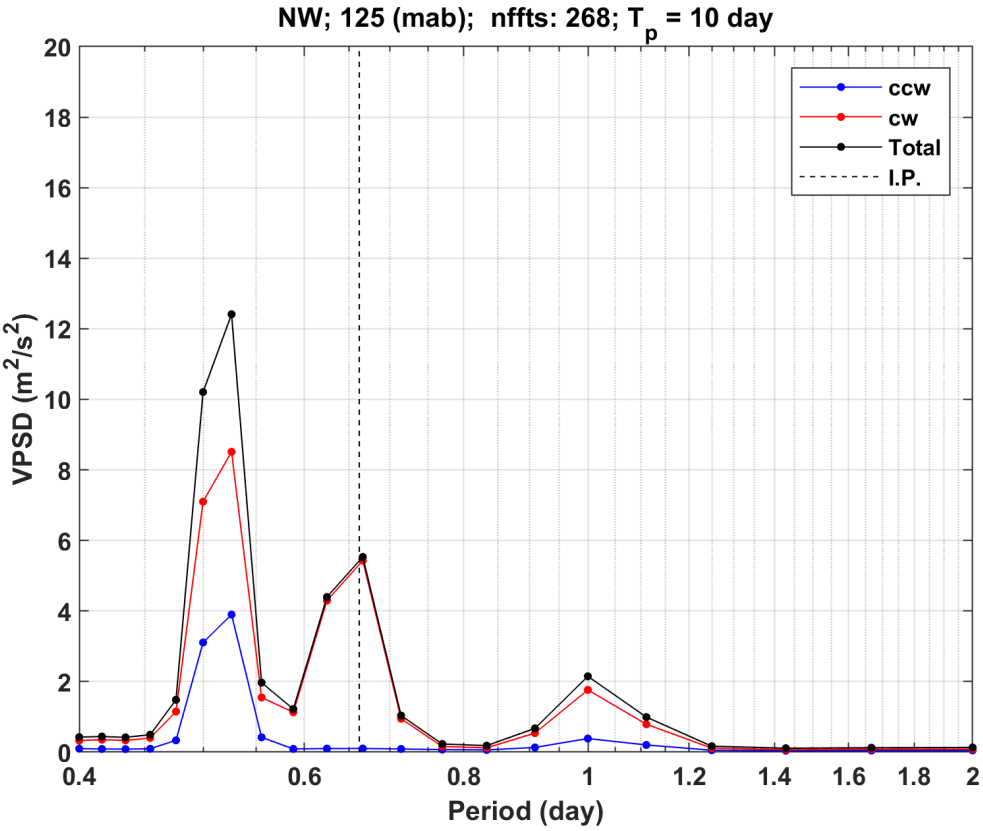

Figure 4.28: Rotary Spectral data both clockwise (cw) and counter-clockwise (ccw) was taken from the North-West mooring in the Endeavour Ridge Valley. Velocity power spectral densities are calculated over a time period (T_p) of 10 days for 268 fast Fourier transforms (nffts). The inertial period (I.P) is marked by a dotted line

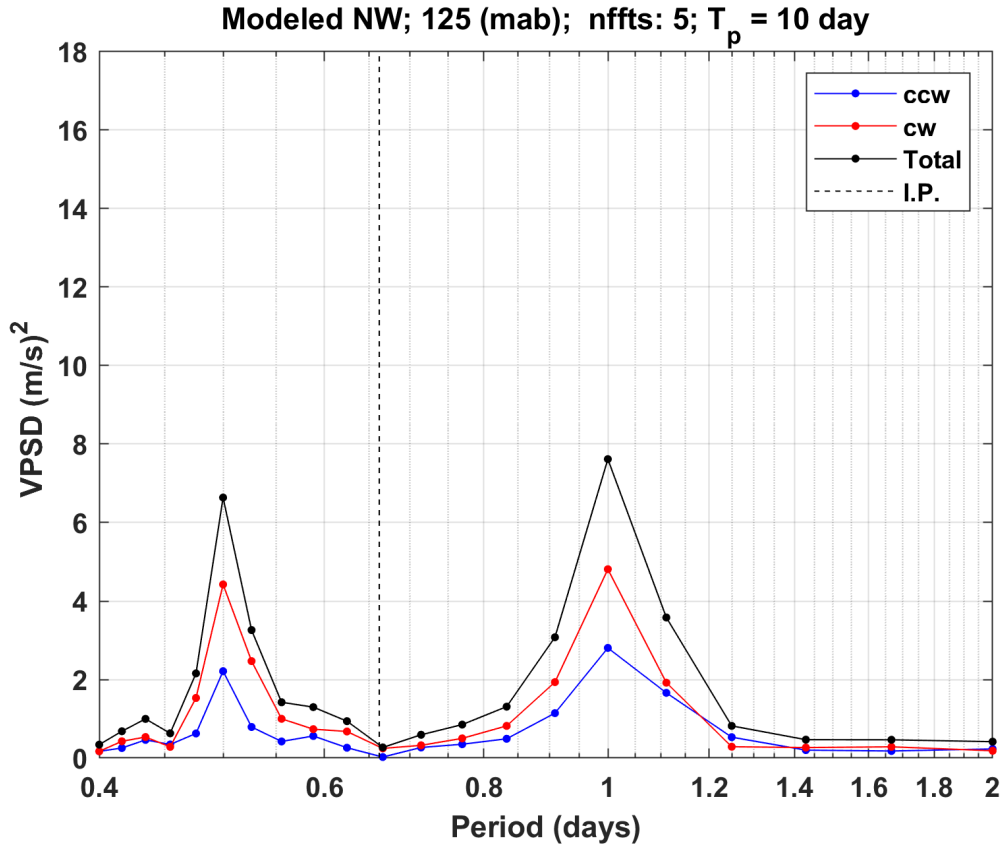

Figure 4.29: Rotary Spectral data both clockwise and counter-clockwise was calculated from the tidally forced, non-nested model under conditions of winter winds and standard venting injection. Velocity power spectral densities are calculated over a time period (T_p) of 10 days for 5 fast Fourier transforms (nffts). The inertial period (I.P) is marked by a dotted line

(u,v) velocities were downloaded from the Global Ocean Forecasting System 3.1(41 layer HYCOM and Navy compiled Ocean Data Assimilation - Global 1/120 Analysis hindcast data) and interpolated to the nodes in the relaxation zone. Figure 4.30 shows that the interpolation scheme which maps HYCOM data onto the model nodes in the relaxation zone and onto the sigma layers is effective. The comparison is made with a nearest HYCOM grid point on the northeast corner of the mesh and depths at 900, 1500 and 2000m were captured. This gives us confidence that the model can be properly forced on the low resolution boundary with inertial effects.

Preliminary Results with HYCOM Nesting: Low Resolution Outputs

Figure 4.31 shows the rotary spectral analysis of the low resolution model output near the NorthWest mooring location. Similar to the signature seen in Figure 4.28, there is a clear spike in the inertial band. This indicates that the HYCOM forced relaxation boundary successfully captures the inertial flows through the Endeavour Ridge Segment.

Figure 4.32 shows the residual horizontal velocities (30 day average) that result from inertial forcing at the boundary of the low resolution nested domain. At 2173m depth, velocities of 3cm/s can be observed traveling south through the ridge valley. At 2100m depth, above the northern sill, these southward velocities can be seen throughout the northern valley. At this depth, flows can be seen to move over the deeper sections of the ridges. Just above the ridges at 1800 m, a uniform flow over the top of the ridge system can be seen. This indicates that the residual flows

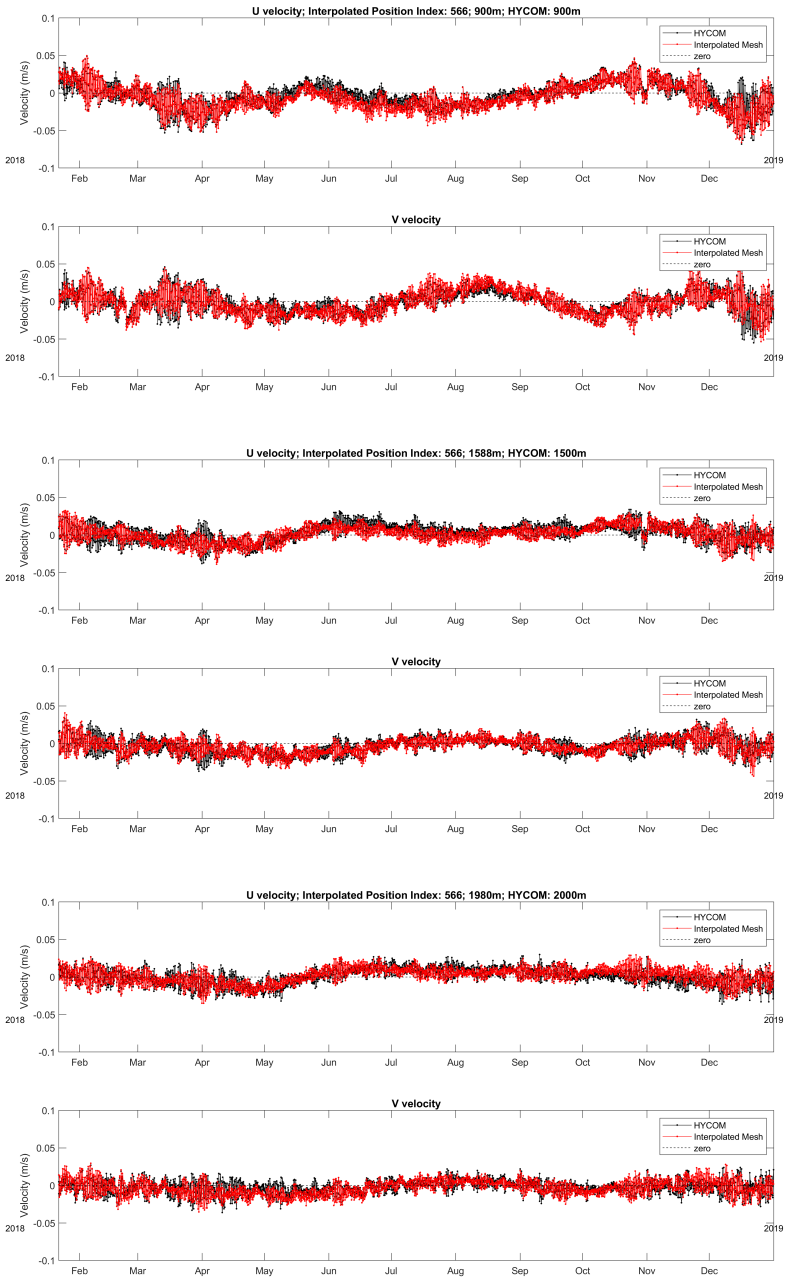

Figure 4.30: Velocity output from the low resolution model is compared to the HYCOM data at that location. Three depths are provided, one near 1000m, one near 1500m and one near 2000m

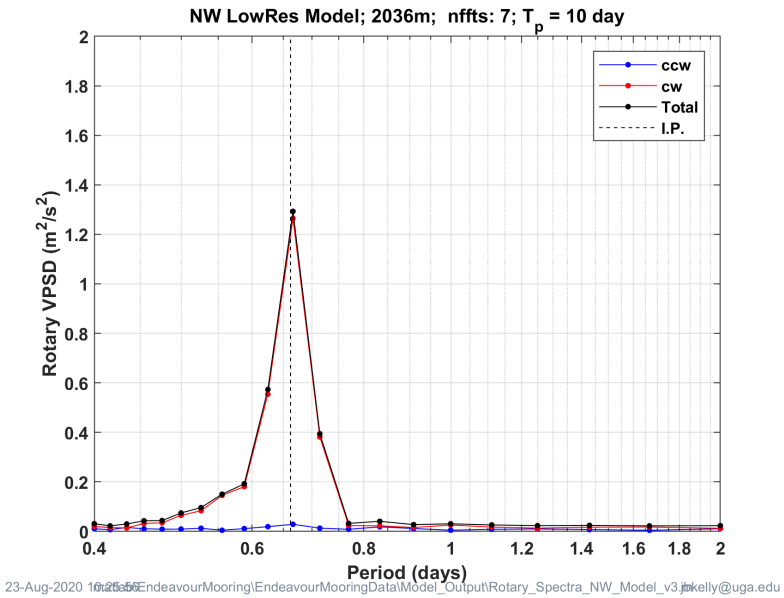

Figure 4.31: Rotary Spectral data both clockwise (cw) and counter-clockwise (ccw) was calculated from the HYCOM forced, low resolution model. Velocity power spectral densities are calculated over a time period (T_p) of 10 days for 7 fast Fourier transforms (nffts). The inertial period (I.P) is marked by a dotted line

from inertial and sub-inertial flows result in a southwesterly directed flow over the ridge system. The velocities reach magnitudes up to 7cm/s, comparable to the residual velocities seen to result from tidal forcings. Even stronger velocities can be seen to flow over the ridge at depths of 1300m. Here the residual flows are directed westward over the top of the ridge system and reach magnitudes up to 10cm/s.

Figure 4.33 shows the transect of velocity along the Endeavour ridge valley. The residual effects from inertial forcing result in an along valley velocity flowing from north to south, with larger inflow velocities at the northern end and decreasing southward. Above 1500m in the south end of the valley, flows toward the north can be observed. Cross valley velocities can be primarily seen to be flowing westward

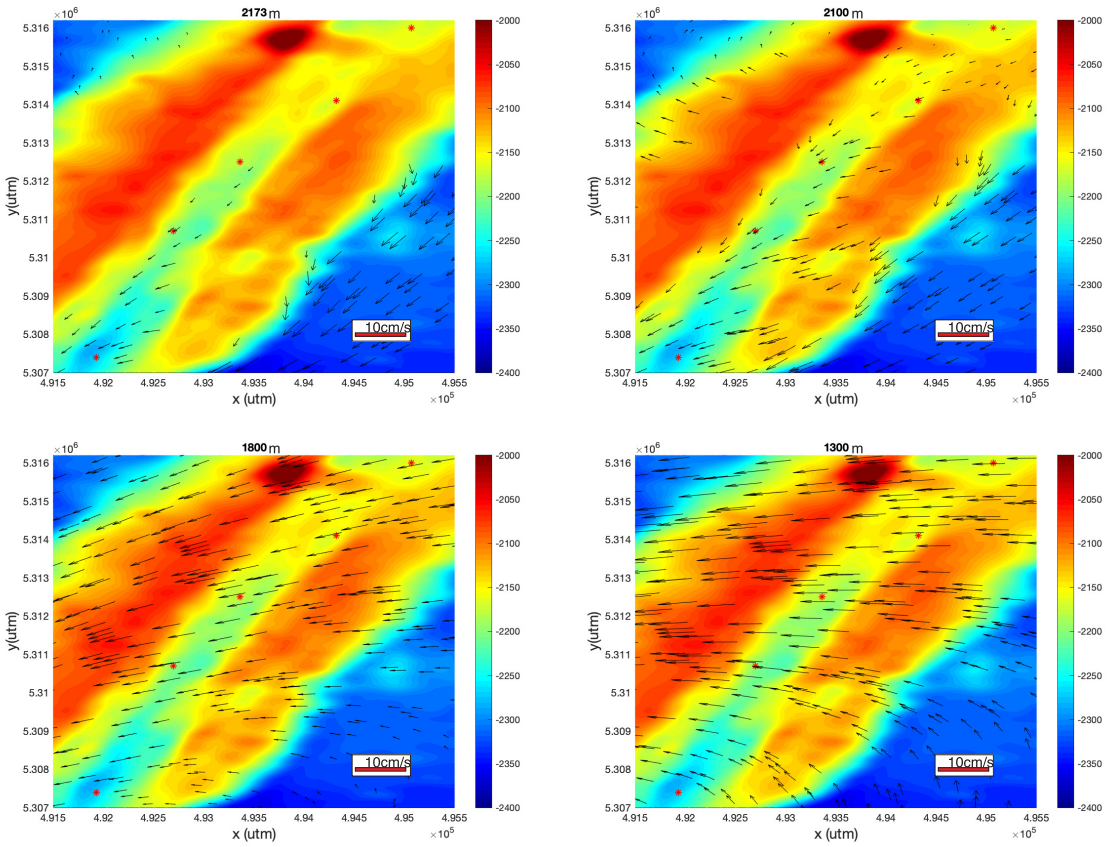

Figure 4.32: Depth dependent residual velocities are displayed throughout the ridge valley. Values are calculated from a 30 day average of the low resolution, HYCOM inertially forced model. The hydrothermal vent fields are marked by red asterisks within the domain. Model does not include any tidal component.

over the ridge system, consistent with the flows seen in Figure 4.32. As is expected, vertical velocities are low and centered about zero.

The influences of inertial forcing on residual flow patterns within the ridge valley have been shown to generate velocities in the ridge valley that are on the same order of magnitude as the residual flows generated from tidal forcings. This indicates that the inertial influences are indeed important to take into consideration when developing a full and complete idea of flows throughout the ridge valley. The southward flows that are seen to develop with the inertial forcing may not be sufficient to overcome the inflow velocities at the south from tidal forcing. This suggests there will still be a zone of convergent flow within the ridge valley, but it may occur at a different location than was seen in the non-nested case.

It is important to discuss the results obtained from the non-nested model runs in light of the nested model forcing results. Though they may not reflect the actual physical picture of flows occurring within the valley, the non-nested results are able to inform the conditions under which hydrothermal circulation cells arise, informing where circulation cells are likely to occur. There were several main conclusions from the results of the non-nested model runs discussed in section 4.3. Each of these points will be reexamined and considered in the context of the initial results from the low resolution inertial forcing model.

Strong topographical steering was observed as a result of the tidally forced flows at the boundary as seen in Figure 4.11. This steering results in strong (up to 10cm/s) residual flows through the valley. Flows are directed into the valley at both

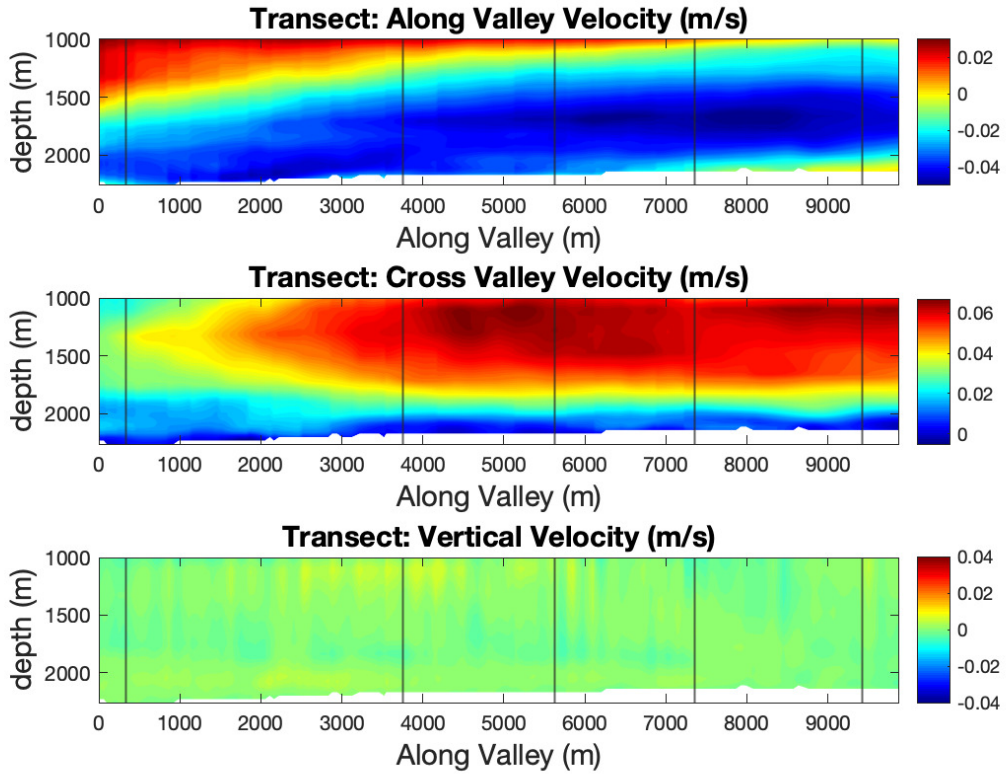

Figure 4.33: Residual velocities within the ridge valley transect intersecting the center of all five venting field locations (vertical lines). The transects run from South to North and display along valley velocity (top figure), cross valley velocity (middle row), and vertical velocity (bottom row). Along axis velocities are positive towards the North-East, cross axis velocities are positive toward the West, and vertical velocities are positive upward. This transect represents velocity through the ridge valley caused by the HYCOM inertial forcing driven over 4 relaxation layers at the boundary.

ends, and converge in the central valley where the interaction of the northward and southward flows creates an area of diminished background crossflow. Inertial forcings on the low resolution nesting model in Figure 4.32 were seen to develop residual horizontal flow magnitudes on the same scale, predominantly southward through the ridge valley. When taken together with the tidal influences, the inertial flows will modify the flow pattern through the ridge system. This will result in a strengthening of the inflows at the northern end of the valley, while diminishing inflow velocities at the southern end of the valley. The strengthened inflow from the north will force the convergent zone towards the south end of the valley towardthe Main Endeavour vent field. It is important to note that the examination of low resolution residual flows suggests the magnitude of the inertially forced flows will not be sufficient to overcome the tidally forced inflows at the south end of the valley. The consequence of this is that a convergent zone (similar to that in the non-nested result) will form within the ridge valley.

Hydrothermal venting activity was seen to result in distinct flow velocity anomalies within the ridge system (see section 4.3.2). Of particular note are the positive vertical velocity anomalies seen to form directly above the vent fields (on the scale of 4cm/s), as well as increased inflow velocities on the southern sides of the venting regions (on the scale of 2cm/s). These phenomena are evident in Figure 4.16. These behaviours can be seen to occur both where the venting region is under conditions of low background crossflow (at High Rise in the central valley) as well as where the venting region is under conditions of larger background crossflows (at

Main Endeavour and Mothra vent field sites). This indicates that even under alternate external flow conditions, such as those caused by inertially forced flows through the ridge valley, the velocity anomalies due to hydrothermal venting will retain behaviour predicted by the non-nested model.

Results from the non-nested modeling studies support the presence of vent driven circulation cells within the ridge valley under conditions of weak horizontal crossflow. This can be seen in Figure 4.17. This indicates that circulation cells are likely to arise between adjacent venting fields in a ridge valley at regions of convergent flow. This observation implies two things. First, it shows that the formation of hydrothermally driven circulation cells is possible under the conditions of low crossflow on either side of venting fields. Second, it displays that these cells arise within the Endeavour Ridge Valley, specifically at the High Rise vent field. Regardless of the manner in which the inclusion of the inertially forced low resolution nesting model changes the dynamics within the ridge system, circulation cells form at regions of venting without a strong horizontal crossflow. Even with inertial effects on the flow dynamics within the Endeavour Ridge valley (implemented through the nesting model), the conditions under which hydrothermally driven circulation cells occur are still present within the valley. As the convergent zone is pushed south, the High Rise vent field will experience stronger horizontal flow velocities, which will inhibit the formation of hydrothermally induced circulation cells at that location. The crossflows at the main Endeavour Field will decrease due to this migration of the convergent zone, making conditions more

favorable for the formation of circulation cells in this region. Overall, though their location will be pulled further south by the inclusion of inertial forcing, conditions that give rise to circulation cells as seen in the non-nested results will be present.

The final conclusion that was made in section 4.3 discussing the non-nested results is that the hydrothermal circulation cells that arise within the Endeavour Ridge valley are on the scale of hundreds of meters in diameter. The scale of the circulation cells may change depending on the external crossflow conditions that occur within the valley depending on the overlap of the convergent zone and venting locations. This overlap of convergent zone and vent fields will depend on the final results of the nested model. We would expect to see approximately the same sizes of circulation cells due to the fact that these cells have to cycle fluid through the scale of the hydrothermal plume, but the exact size is dependent on the external flow conditions, as was seen in the examination of circulation around High Rise in Figure 4.17, where the circulation cell on the northern side of the field was seen to be both smaller and higher up in the water column, presumably due to enhanced flow from the northern end of the valley.

The majority of the conclusions made from the non-nested model results still hold under conditions of the nesting model runs and the concomitant incorporation of inertial forcing: 1) Tidal boundary forcing will still be topographically forced through the valley, 2) vent fields have a distinct influence of flow patterns even under strong crossflow conditions. These are unaffected because they are conclusions independent

of the actual flow. However, accounting for the inertial flow will likely alter the size and location of circulation cells that form within the Endeavour Ridge valley.

CHAPTER 5

SUMMARY, CONCLUSIONS, AND FUTURE RECOMMENDATIONS

5.1 Overview

Throughout this research dissertation, there were two main prongs of investigation into the physical effects of hydrothermal venting and their influence on their surroundings. The first was an in depth examination into the detailed physical characteristics of the hydrothermal vent plume and the internal processes that contribute to driving the mixing and conservation of turbulent quantities. The second was a large domain, ridge scale examination into the influences of multiple adjacent hydrothermal venting fields on currents within the ridge valley. As these investigations are two very different ways of examining hydrothermal plume behaviour and interactions with surroundings, we draw different sets of conclusions from each one.

5.2 Turbulent Properties of a Hydrothermal Plume

In order to put the overall results and conclusions of the Large Eddy Simulation research project described in Chapters 2 and 3 into a framework, it is helpful to recall the physical meanings of turbulence characteristics and their effects throughout the plume. LESs are a powerful tool that is needed to understand these

turbulent characteristics within the initial 30m rise height of a hydrothermal plume. As the hydrothermal vent injects heat and mass into the cold ambient ocean, the buoyant hydrothermal effluent rapidly rises and mixes with entrained ambient water, creating a turbulent buoyant plume. Velocity gradients in the rising fluid bring about shear, resulting in a production of turbulent kinetic energy because of momentum fluxes. Local buoyant instabilities also generate turbulent kinetic energy, but surprisingly this effect is small. Considering these two production terms, as well as the upward advection of turbulent kinetic energy, it is possible to quantify the rate of dissipation of TKE for the hydrothermal plume assuming a steady state balance of production and dissipation.

Mixing in the plume results in a production of thermal variance because of stronger temperature gradients resulting in heat fluxes. Vertical advection turns out to be an important contribution to thermal variance, and dissipation is assumed to balance this gain. Production is important to consider because values can reach comparable magnitudes to the advection contributions, depending on background crossflow and region within the plume.

Once the dissipation rates for TKE and thermal variance are known, the strength of the refractive index fluctuations, our observational turbulence measurement, was obtained. This allows for the modeled internal characteristics to be compared to real world observations of vent plumes, and allows us to draw conclusions to the internal mechanisms and dependencies on acoustic forward scatter.

It was found that the thermal variance dissipation rate dominates over the TKE dissipation rate in determination of the refractive index fluctuations. This leads us to the conclusion that the total refractive index is dependent on the advection of thermal variance for the region of the plume we studied.

The model shows a sensitivity to the Smagorinsky mixing coefficients chosen, and these may need to be appropriately tuned depending on the physical location that the model is trying to replicate. Use of an isotropic vertical and horizontal Smagorinsky mixing coefficient in the model is seen to result in turbulence characteristics much larger than are realistic, as well as not showing any response to crossflow. Increase in source heat transport (and hence heat flux) results in a slight increase in many turbulence characteristics, as well as increased resistance to horizontal crossflow. Increase in the plume source area (and hence a decrease in heat flux) is seen to lower the overall magnitude of turbulence characteristics within the plume, as well as to increase the resistance to horizontal crossflow. In all, this modeling project has successfully mapped the internal physical mechanisms by which the heat and mass injected by a hydrothermal vent bring about the dissipation of TKE and thermal varince, and the dominant factors that control the observed turbulent plume behaviours.

5.3 Ridge Scale Circulation Effects with Multiple Vent Fields

The Endeavour Ridge segment of the Juan de Fuca Ridge is a system of five hydrothermal venting sites within the ridge valley. Tidally forced topographically

steered currents run through this valley, creating a residual flow that converges in the central valley. Interactions between these currents and venting are examined through this research, aiming to uncover the synergistic effects of adjacent field interaction on the ridge scale flows, a much larger scale than previously examined in our single plume study.

Vent fields are seen to cause residual hydrothermally induced circulation cells in regions between two adjacent venting sites. Strong topographical steering of tidally driven flow throughout the ridge valley results in circulation cells being more evident near to the center of the valley (where residual crossflows are weakest). These cells reach up to several hundred meters in diameter, and are located to either side of the vent field. This is evidence as to the existence of hydrothermally driven circulation cells that result from interactions between adjacent venting fields constrained within a ridge valley.

5.4 Future Recommendations

Through this dissertation, we have presented the results of two different methods we used to explore the physical characteristics and influences of hydrothermal venting. We used LES to focuses on a single vent plume in order to elucidate the important mechanisms by which the venting activity injects and disperses turbulent energy and temperature variability throughout the ocean bottom, and we used FVCOM to explore the effects and influences that multiple hydrothermal venting fields have on regional currents through a spreading ridge. Both of these projects provide jumping

off points for further research and exploration into the physical characteristics of hydrothermal plumes and their interaction with their environment.

The turbulent convection model that was used to investigate the internal turbulence characteristics of a hydrothermal plume was shown to be able to represent the physical plume at Dante, as well as to identify internal turbulent mechanisms that occur within a focused high temperature venting plume. This method can be tuned to other real world plumes in order to identify characteristics that have not been measured, and make predictions as to how those plumes disperse heat and effluent into the deep ocean surroundings. Further research that can be done to build improvements to the accuracy of these predictions would be to explore the tuning of the vertical Smagorinsky coefficient. In this study we have tested two values for the vertical Smagorinsky coefficient, and a more in depth examination of the influence of increasing or decreasing this parameter would be valuable to improving the predictions made by the model.

Results from the Chapter 3 displayed interesting effects of increasing heat flux that were dependent on either changing the source area or changing the vent heat output. Increasing heat flux through decreasing source area was seen to cause characteristic magnitudes to increase at times of low background crossflow, while magnitudes at high crossflows were unchanged. Increase in heat flux through increase in total heat transport from the vent was seen to cause characteristic magnitudes to increase during high crossflows, while magnitudes at low crossflows remained mainly unchanged. This unexpected interplay warrants further

Table 5.1: Proposed model runs

	20 MW	40 MW	80 MW
6x6m^2	Ex1, 0.55MW/m^2	Ex2, 1.1MW/m^2	Ex3, 2.2MW/m^2
4x4.5m^2	Ex4, 1.1MW/m^2	Ex5, 2.2MW/m^2	Ex6, 4.4MW/m^2
3x3m^2	Ex7, 2.2MW/m^2	Ex8, 4.4MW/m^2	Ex9, 8.8MW/m^2

experimentation to fully characterize the dependance of the plume characteristics on both source area and heat output, by way of heat flux. Future work should consist of a matrix of model experiment to account for a range of both heat output and source area. Experiments should be set such that comparisons can be made between experiments with differing source conditions, but identical heat fluxes. An example of a matrix of cases is shown in Table 5.1.

From this set of nine model experiments, three sets of analyses can be done. First will be to examine increasing heat output at constant source area (Ex. 1, 2, and 3; Ex. 4, 5, and 6; Ex. 7, 8, and 9). Second will be the examination of decreasing source area with constant heat output(Ex. 1, 4, and 7; Ex. 2, 5, and 8; Ex. 3, 6, and 9). Third will be to compare cases with the same heat flux values, but different source conditions (Ex. 2 and 4; Ex. 3, 5, and 7; Ex. 6 and 8). These sets of comparisons should fully elucidate the relationship between the source conditions that influence heat flux, and the resultant effects on the turbulent plume characteristics of interest during times of no crossflow and maximum crossflow.

Our regional scale FVCOM model provides a good examination of the residual valley currents generated from tidal forces and the influence of hydrothermal venting on these regional currents. The nested forcing component of this research is

in its initial stages and adds any geostrophic and inertial forcing seen to be present throughout the region. Future work for this model consists of adding tides together with multiple venting conditions similar to the analysis that has been carried out in the non-nested model runs. The refinement and expansion of this work will include an examination of the low resolution FVCOM output with comparison to the HYCOM data within the large scale region and in particular on the boundary of the high resolution mesh to ensure that the boundary forcing on the high resolution model is a good representation of the inertial signal. In addition, sea surface height calculations made from the Tidal Model Driver program should be used to force the high resolution model for the year of 2018. These predicted heights are compared to the sea surface heights recorded by the North West mooring in Figure 5.1. This comparison shows that there is an excellent fit between the predicted tides and the actual sea surface heights experienced by the NW mooring. This gives confidence that the high resolution model will have appropriate tidal forcing along the boundary. Finally a comparison of high resolution modeled results to moored data time series at various depths, and an extended model run covering the entire year of 2018 to build a continual picture of the venting effects through different seasons needs to be done.

These recommendations will better elucidate how the hydrothermal fluid injected into the bottom ocean realistically interacts with the regional scale flows, and will serve to setup a more physically representative picture of the regional scale flow patters. While this modeling gives insight as to the formation of hydrothermally driven circulation cells within the ridge valley, there are even more potential

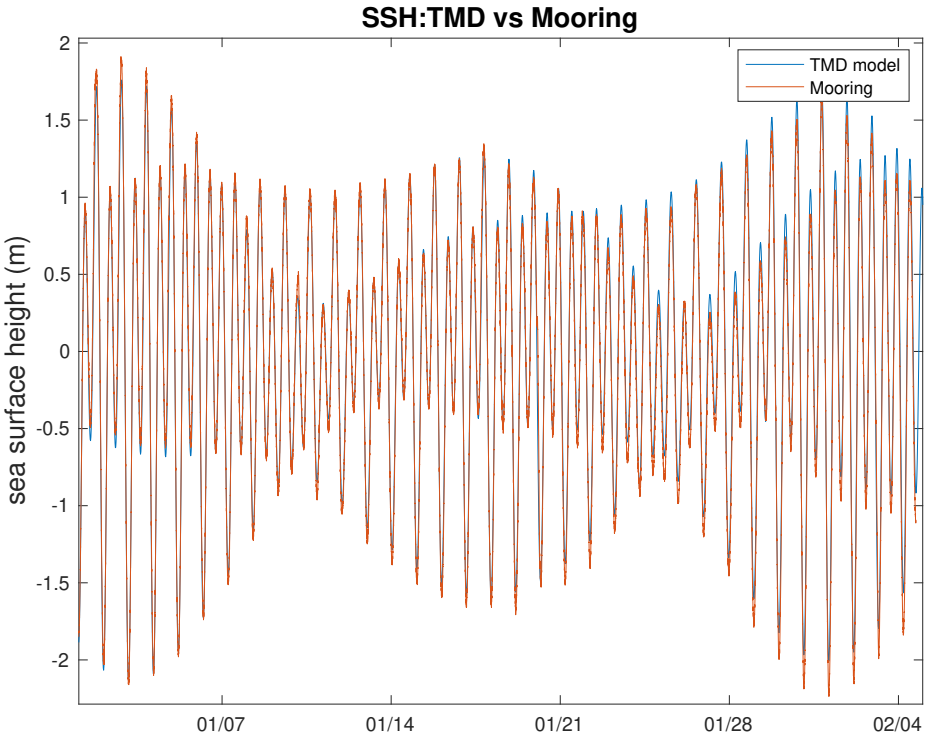

Figure 5.1: Sea surface height time series obtained from TMD (blue) is compared to the NW valley mooring data (red) to demonstrate accuracy of the forcing that will be used on the high resolution boundary. Data is representative of sea surface heights in 2018

directions that this model could be expanded to address further research questions. A large concern of hydrothermal modeling concerns the dispersion of chemicals and larvae from in and round the venting site. The incorporation of Lagrangian particle tracking would simulate the transport (both vertically and laterally) of vent larvae throughout the region. The use of dye tracking FVCOM modules would be useful in order to build and track the dispersion of vent chemical signals through the region. In both cases, these tracking methods would be able to define where vent effluent is transported through the region (as temperature and salinity are not good tracers), and identify locations within the ridge valley that would experience regions of increased chemical concentration, or pockets of larval aggregation. These model results will serve to build a temporally variable chemical concentration regional profile, as well as to guide targeted observational research and sample collection.

Appendix A

1. Model Operation

To run the turbulent convection large eddy and FVCOM simulations, we made use of the Georgia Advanced Computing Resource Center (GACRC). The GACRC has access to multiple groups of compute nodes with varying processor power, various compilers, and a large amount of memory and storage. This research project is carried out on the Sapelo2 cluster, with a CentOS Linux operating system. There are over 500 software packages currently installed on Sapelo2 with more being continually added.

The LES model was run using a PGF90 compiler (PGI 17.9), linked with netCDF 4.1.3 libraries included on the Sapelo2 cluster. We ran the model on one node with eight threaded cores for parallelization, 10GB of memory, and a walltime limit of 15 days. These values were selected through testing to complete the modeled runs in the shortest amount of time without increasing the computer requirements too far.

The turbulent convection model outputs two netCDF files, one that resolves the full plume over its rise height and bending, and the other that resolves near source plume (this is hereafter referred to as the cone values) at all time steps. The full spatial extent of the plume is on a domain of approximately 192m x192m in the horizontal by up to 384m in the vertical. This was chosen to be able to observe the physical plume behaviour throughout its full spatial extent. The cone values

represent a 200 gigabyte file that is output on a region extending to 25 m above source. This output file was designed to be able to resolve the turbulent characteristics. Both of the file types are analyzed and explored fully within the results section of this research.

The FVCOM model was run on the GACRC on 6 nodes with 48 processors each. The model output every 20 minutes into daily files of 2 gigabytes each.

2. Turbulence Equations

The turbulent kinetic energy and thermal variance equations originate from the Navier-Stokes momentum equation and the heat equation. These quantities can be obtained by performing a Reynolds decomposition ($u = U + u', \theta = \Theta + \theta'$) on the steady state ($\frac{\partial}{\partial t} = 0$) version of the momentum and heat equation, multiplying each by the turbulent velocity or temperature respectively, and then averaging. Note that the divergence terms other than the transport are neglected.

The three dimensional momentum equation is

$$\frac{\partial}{\partial t}\mathbf{u} + (\mathbf{u} \cdot \nabla)\mathbf{u} = -\nabla p/\rho_o + \nu\nabla^2\mathbf{u} - g\rho'/\rho_o\hat{k} \tag{A.1}$$

The advection term for TKE becomes,

$$(\mathbf{u}\cdot\nabla)\mathbf{u} => \overline{u_i'(U_j+u_j')\frac{\partial}{\partial x_j}(U_i+u_i')} = \overline{(U_j+u_j')\frac{\partial}{\partial x_j}\frac{u_i'u_i'}{2}} + \overline{u_i'u_j'}\frac{\partial U_i}{\partial x_j} \tag{A.2}$$

$$= \overline{u_j\frac{\partial}{\partial x_j}q^2} + \overline{u_i'u_j'S_{ij}}; \qquad S_{ij} = \tfrac{1}{2}(\frac{\partial U_i}{\partial x_j} + \frac{\partial \partial U_j}{\partial x_i}) \tag{A.3}$$

$$= \overline{\frac{\partial}{\partial x_j}u_jq^2} + \overline{\frac{\tau_{ij}}{\rho_0}S_{ij}}; \qquad \overline{u_i'u_j'} = \frac{\tau_{ij}}{\rho_0}\text{is the Reynolds stress} \tag{A.4}$$

The viscous term becomes,

$$\nu\nabla^2\mathbf{u} => \overline{u_i'\nu\nabla^2(U_i+u_i')} = \overline{\nu u_i'\frac{\partial^2}{\partial {x_j}^2}u_i'} \tag{A.5}$$

$$= \overline{\nu u_i'\frac{\partial}{\partial x_j}(\frac{\partial u_i'}{\partial x_j} + \frac{\partial u_j'}{\partial x_i})} \tag{A.6}$$

$$= \overline{\nu\frac{\partial}{\partial x_j}u_i'(\frac{\partial u_i'}{\partial x_j} + \frac{\partial u_j'}{\partial x_i})} - \overline{\nu(\frac{\partial u_i'}{\partial x_j} + \frac{\partial u_j'}{\partial x_i})\frac{\partial u_i'}{\partial x_j}} \tag{A.7}$$

$$\overline{\nu\frac{\partial}{\partial x_j}u_i'(\frac{\partial u_i'}{\partial x_j} + \frac{\partial u_j'}{\partial x_i})} - \overline{\nu 2 s_{ij}s_{ij}}; \qquad s_{ij} = \tfrac{1}{2}(\frac{\partial u_i'}{\partial x_j} + \frac{\partial u_j'}{\partial x_i}) \tag{A.8}$$

The buoyancy term becomes,

$$-g\rho'/\rho_o\hat{k} => -g\frac{\overline{\rho'u_i'}}{\rho_o}\hat{k} \tag{A.9}$$

$$= \overline{\frac{g}{\rho_o}K_v\frac{\partial\rho_o}{\partial z}}; \qquad \overline{\rho'w'} = -K_V\frac{\partial\rho_o}{\partial z}\text{is the buoyancy flux} \tag{A.10}$$

$$= \overline{-K_vN^2} \tag{A.11}$$

Therefore the TKE equation is (neglecting all divergence terms except vertical advection),

$$\overline{\frac{\partial}{\partial x_j} u_j q^2} + \overline{\frac{\tau_{ij}}{\rho_0} S_{ij}} = -\overline{K_v N^2} - \bar{\epsilon} \tag{A.12}$$

The TKE dissipation rate is then,

$$\epsilon = -\tau_{ij} S_{ij} - K_v N^2 - \frac{\partial}{\partial z}\overline{w q^2} \tag{A.13}$$

$$= P - B - \frac{\partial}{\partial z} w q^2 \tag{A.14}$$

The heat equation is,

$$\frac{\partial}{\partial t}\theta + (\mathbf{u} \cdot \nabla)\theta = K_\theta \nabla^2 \theta \tag{A.15}$$

The advection becomes,

$$(\mathbf{u} \cdot \nabla)\theta => \overline{\theta'(U_i + u_i')\frac{\partial}{\partial x_i}(\Theta + \theta')} = \overline{\theta' u_i \frac{\partial}{\partial x_i}\theta'} + \overline{(-K_i \frac{\partial \theta}{\partial x_i})\frac{\partial \theta}{\partial x_i}} \tag{A.16}$$

$$= \overline{u_i \frac{\partial}{\partial x_i}\frac{\theta'^2}{2}} - \overline{K_i (\frac{\partial \Theta}{\partial x_i})^2}; \qquad -\theta' u_j' = K_j \frac{\partial \Theta}{\partial x_j} \text{is the heat flux} \tag{A.17}$$

$$= \frac{\partial}{\partial x_i}\frac{u_i \theta'^2}{2} - P_\theta \tag{A.18}$$

$$\tag{A.19}$$

The diffusive term is,

$$K_\theta \nabla^2 \theta => \overline{\theta' K_\theta \frac{\partial^2}{\partial x_j^2}(\Theta + \theta')} \tag{A.20}$$

$$= K_\theta \overline{\frac{\partial}{\partial x_j}(\theta' \frac{\partial \theta'}{\partial x_j})} - K_\theta \overline{\frac{\partial \theta'}{\partial x_j} \frac{\partial \theta'}{\partial x_j}} \tag{A.21}$$

Therefore neglecting the divergence term on the molecular diffusion term and the horizontal advection terms, the thermal variance equation is then,

$$\frac{\partial}{\partial z} w \frac{\theta'^2}{2} - P_\theta = -\epsilon_\theta \tag{A.22}$$

The thermal dissipation is thus,

$$\epsilon_\theta = P_\theta - \frac{\partial}{\partial z} w \frac{\theta'^2}{2} \tag{A.23}$$

BIBLIOGRAPHY

Adams, D. K., McGillicuddy, D. J., Zamudio, L., Thurnherr, A. M., Liang, X., Rouxel, O., German, C. R., & Mullineaux, L. S. (2011). Surface-generated mesoscale eddies transport deep-sea products from hydrothermal vents. *Science*, *332*(6029), 580–583. doi:10.1126/science.1201066

Allen, S. E., & Thomson, R. E. (1993). Bottom-trapped subinertial motions over midocean ridges in a stratified rotating fluid. *Journal of Physical Oceanography*, *23*, 566–581.

Aquaveo. (2020). *Surface-water modeling system (v12.1)*. 12.1. Aquaveo. Engineering Computer Graphics Laboratory, Brigham Young University, Provo, Utah.

Baker, E. T., & German, C. R. (2004). On the global distribution of hydrothermal vent fields. In *Geophysical monograph series* (Vol. 148, pp. 245–266). doi:10.1029/148GM10

Baker, E. T., German, C. R., & Elderfield, H. (1995). Hydrothermal plumes over spreading-center axes: Global distributions and geological inferences. In *Geophysical monograph series* (Vol. 91, pp. 47–71). doi:10.1029/GM091p0047

Baker, E. T., & Massoth, G. J. (1987). Characteristics of hydrothermal plumes from two vent fields on the Juan de Fuca Ridge, northeast Pacific Ocean. *Earth and Planetary Science Letters*, *85*(1-3), 59–73. doi:10.1016/0012-821X(87)90021-5

Barge, L. M., Abedian, Y., Doloboff, I. J., Nuñez, J. E., Russell, M. J., Kidd, R. D., & Kanik, I. (2015). Chemical gardens as flow-through reactors simulating natural hydrothermal systems. *Journal of Visualized Experiments*, *2015*(105). doi:10.3791/53015

Barge, L. M., Flores, E., Baum, M. M., Velde, D. G., & Russell, M. J. (2019). Redox and pH gradients drive amino acid synthesis in iron oxyhydroxide mineral systems. *Proceedings of the National Academy of Sciences of the United States of America*, *116*(11), 4828–4833. doi:10.1073/pnas.1812098116

Beaulieu, E. S., & Szafranski, K. (2018). Interridge global database of active submarine hydrothermal vent fields, version 3.4. world wide web electronic publication available from http://vents-data.interridge.org. Retrieved from https://vents-data.interridge.org

Beaulieu, S. E., Baker, E. T., & German, C. R. (2015). Where are the undiscovered hydrothermal vents on oceanic spreading ridges? *Deep-Sea Research Part II: Topical Studies in Oceanography*, *121*, 202–212. doi:10.1016/j.dsr2.2015.05.001

Bennett, S. A., Hansman, R. L., Sessions, A. L., ichi Nakamura, K., & Edwards, K. J. (2011). Tracing iron-fueled microbial carbon production within the hydrothermal plume at the Loihi seamount. *Geochimica et Cosmochimica Acta*, *75*(19), 5526–5539. doi:10.1016/j.gca.2011.06.039

Berdeal, I. G., Hautala, S. L., Thomas, L. N., & Johnson, H. P. (2006). Vertical structure of time-dependant currents in a mid-ocean ridge axial valley. *Deep-Sea Research*, *53*, 367–386.

Boyer, T., Antonov, J. I., Baranova, O. K., Coleman, C., Garcia, H. E., Grodsky, A., Johnson, D. R., Locarnini, R. A., Mishonov, A. V., O'Brien, T., Paver, C., Reagan, J., Seidov, D., Smolyar, I. V., & Zweng, M. M. (2013). 2013: World ocean database 2013.

Breier, J. A., Toner, B. M., Fakra, S. C., Marcus, M. A., White, S. N., Thurnherr, A. M., & German, C. R. (2012). Sulfur, sulfides, oxides and organic matter aggregated in submarine hydrothermal plumes at 9 °50'N East Pacific Rise. *Geochimica et Cosmochimica Acta*, *88*, 216–236. doi:10.1016/j.gca.2012.04.003

Cenedese, C., & Linden, P. F. (2014). Entrainment in two coalescing axisymmetric turbulent plumes. *Journal of Fluid Mechanics*, *752*. doi:10.1017/jfm.2014.389

Chan, S. N., & Lee, J. H. (2016). A particle tracking model for sedimentation from buoyant jets. *Journal of Hydraulic Engineering*, *142*(5). doi:10.1061/(ASCE)HY.1943-7900.0001112

Chen, C., Beardsley, R. C., & Cowles, G. (2006). An unstructured-grid, finite-volume coastal ocean model (FVCOM) system. *Oceanography*, *19*(SPL.ISS. 1), 78–89. doi:10.5670/oceanog.2006.92

Corliss, J., Dymond, J., Gordon, L. I., Edmond, J. M., von Herzen, R. P., Ballard, R. D., Green, K., Williams, D., Bainbridge, A., Crane, K., & van Andel, T. H. (1979). Submarine thermal springs of Galapagos Rift. *Science*, (4385), 1073–1083.

Cullen, J. T., & Coogan, L. A. (2017). Changes in fe oxidation rate in hydrothermal plumes as a potential driver of enhanced hydrothermal input to near-ridge sediments during glacial terminations. *Geophysical Research Letters*, *44*(23), 11, 951–11958.

Dai, Z., Tseng, L. K., & Faeth, G. M. (1994). Structure of round, fully developed, buoyant turbulent plumes. *Journal of Heat Transfer*, *116*(2), 409–417. doi:10.1115/1.2911413

Devenish, B. J., Rooney, G., Webster, H., & Thomson, D. (2010). The Entrainment Rate for Buoyant Plumes in a Crossflow. *Boundary-Layer Meteorology*, *134*, 411–439.

Dick, G. J., Anantharaman, K., Baker, B. J., Li, M., Reed, D. C., & Sheik, C. S. (2013). The microbiology of deep-sea hydrothermal vent plumes: Ecological and biogeographic linkages to seafloor and water column habitats. doi:10.3389/fmicb.2013.00124

DiIorio, D., & Farmer, D. (1998). Separation of current and sound speed in the effective refractive index for a turbulent environment using reciprocal acoustic transmission. *J. Acoust. Soc. Am. 103*, 321–329.

Dymond, J., & Roth, S. (1987). Plume dispersed hydrothermal particles: A time-series record of settling flux from the endeavour ridge using moored sensors. *Geochimico a Cosmochimica Acta*, *52*, 2525–2536.

Findlay, A. J., Gartman, A., Shaw, T. J., & III, G. W. L. (2015). Centration and partitioning in the first 1.5 m of hydrothermal trace metal concent plumes

along the mid-atlantic ridge; tag, snakepit, and rainbow. *Chemical Geology*, *412*, 117–131.

Fitzsimmons, J. N., Boyle, E. A., & Jenkins, W. J. (2014). Distal transport of dissolved hydrothermal iron in the deep South Pacific Ocean. *Proceedings of the National Academy of Sciences of the United States of America*, *111*(47), 16654–16661. doi:10.1073/pnas.1418778111

Gao, X., Dong, C., Liang, J., Yang, J., Li, G., Wang, D., & McWilliams, J. (2019). Convective instability-induced mixing and its parameterization using large eddy simulation. *Ocean Modelling*, *137*, 40–51.

George, W. K., Alpert, R. L., & Tamanini, F. (1977). Turbulence measurements in an axisymmetric buoyant plume. *International Journal of Heat and Mass Transfer*, *20*(11), 1145–1154. doi:10.1016/0017-9310(77)90123-5

German, C. R., Casciotti, K. A., Dutay, J. C., Heimbürger, L. E., Jenkins, W. J., Measures, C. I., Mills, R. A., Obata, H., Schlitzer, R., Tagliabue, A., Turner, D. R., & Whitby, H. (2016). Hydrothermal impacts on trace element and isotope ocean biogeochemistry. *Philosophical Transactions of the Royal Society A: Mathematical, Physical and Engineering Sciences*, *374*(2081). doi:10.1098/rsta.2016.0035

German, C. R., Resing, J. A., Xu, G., Yeo, I. A., Walker, S. L., Devey, C. W., Moffett, J. W., Cutter, G. A., Hyvernaud, O., & Reymond, D. (2020). Hydrothermal Activity and Seismicity at Teahitia Seamount: Reactivation of

the Society Islands Hotspot? *Frontiers in Marine Science*, *7*, 1–11. doi:10.3389/fmars.2020.00073

Halliwell, J., George R. (1998). Simulation of North Atlantic Decadal/Multidecadal Winter SST Anomalies Driven by Basin-Scale Atmospheric Circulation Anomalies. *Journal of Physical Oceanography*, *28*(1), 5–21. doi:10.1175/1520-0485(1998)028<0005:SONADM>2.0.CO;2. eprint: https://journals.ametsoc.org/jpo/article-pdf/28/1/5/4428993/1520-0485(1998)028_0005_sonadm_2_0_co_2.pdf

Helfrich, K. R., & Speer, K. G. (1995). Oceanic hydrothermal circulation: Mesoscale and basin-scale flow. In *Geophysical monograph series* (Vol. 91, pp. 347–356). doi:10.1029/GM091p0347

Hendrix, A. R., Hurford, T. A., Barge, L. M., Bland, M. T., Bowman, J. S., Brinckerhoff, W., Buratti, B. J., Cable, M. L., Castillo-Rogez, J., Collins, G. C., Diniega, S., German, C. R., Hayes, A. G., Hoehler, T., Hosseini, S., Howett, C. J. A., McEwen, A. S., Neish, C. D., Neveu, M., Nordheim, T. A., Patterson, G. W., Patthoff, D. A., Phillips, C., Rhoden, A., Schmidt, B. E., Singer, K. N., Soderblom, J. M., & Vance, S. D. (2019). The nasa roadmap to ocean worlds. *Astrobiology*, *19*(1), 1–27. doi:10.1089/ast.2018.1955

Herschy, B., Whicher, A., Camprubi, E., Watson, C., Dartnell, L., Ward, J., Evans, J. R., & Lane, N. (2014). An Origin-of-Life Reactor to Simulate Alkaline Hydrothermal Vents. *Journal of Molecular Evolution*, *79*(5-6), 213–227. doi:10.1007/s00239-014-9658-4

Kalnay, E., Kanamitsu, M., Kistler, R., Collins, W., Deaven, D., Gandin, L., Iredell, M., Saha, S., White, G., Woollen, J., Zhu, Y., Leetmaa, A., Reynolds, B., Chelliah, M., Ebisuzaki, W., Higgins, W., Janowiak, J., Mo, K. C., Ropelewski, C., Wang, R., J. Jenne, & Joseph, D. (1996). The ncep/ncar 40-year reanalysis project. *Bulletin of the American Meteorological Society*, *77*, 437–472.

Kaye, N. B., & Linden, P. F. (2004). Coalescing axisymmetric turbulent plumes. *jfm*, *502*, 41–63.

Kelley, D. S., Karson, J. A., Blackman, D. K., Fruh-Green, G. L., Butterfield, D. A., Lilley, M. D., Olson, E. J., Schrenk, M. O., Roe, K. K., Lebon, G. T., Rivizzigno, P., & Party, A.-6. S. (2001). An off-axis hydrothermal vent field near the mid-atlantic ridge at 30n. *Nature*, *412*.

Kelley, D., Delaney, J., Yoerger, D., Caress, D., Clague, D., & Denny, A. (2015). Processed bathymetry grids (netcdf:gmt format) derived from multibeam sonar data from the juan de fuca - endeavour spreading center segment assembled as part of the jdf:endeavour$_b$*athymetrydatacompilation*. *Integrated Earth Data Applications (IEDA)*.

Kotsovinos, N. E. (1977). Plane Turbulent buoyant jets. Part 2. Turbulence structure. *Journal of Fluid Mechanics*, *81*, 45–62.

Kotsovinos, N. E., & List, E. J. (1977). Plane turbulent jets. Part 1. Integral properties. *Journal of Fluid Mechanics*, *81*, 45–62.

Lavelle, J. W., & Cannon, G. A. (2001). On subinertial oscillations trapped by the Juan de Fuca Ridge, northeast Pacific. *Journal of Geophysical Research: Oceans*, *106*(C12), 31099–31116. doi:10.1029/2001jc000865

Lavelle, J. W., Di Iorio, D., & Rona, P. (2013). A turbulent convection model with an observational context for a deep-sea hydrothermal plume in a time-variable cross flow. *Journal of Geophysical Research: Oceans*, *118*(11), 6145–6160. doi:10.1002/2013JC009165

Lavelle, J. (1997). Buoyancy-driven plumes in rotating, stratified cross flows: Plume dependence on rotation, turbulent mixing, and cross-flow strength. *J. Geophys. Res. 102*, 3405–3420.

Lilly, D. (1962). On the numerical simulation of buoyant convection. *Tellus*, *14*, 148–172.

Linder, C. (2017). The hot spot beneath Yellowstone Park. *Oceanus*, *52*(2), 54–60.

List, E. J. (1982). Turbulent Jets and Plumes. *Annual Review of Fluid Mechanics*, *14*(1), 189–212. doi:10.1146/annurev.fl.14.010182.001201

Lupton, J. E., Delaney, J. R., Johnson, H. P., & Tivey, M. K. (1985). Entrainment and vertical transport of deep-ocean water by buoyant hydrothermal plumes. *Nature*, *316*, 621–623.

Lupton, J. E. (1995). Hydrothermal plumes: Near and far field. In *Geophysical monograph series* (Vol. 91, pp. 317–346). doi:10.1029/GM091p0317

Lupton, J. E., & Craig, H. (1981). A major helium-3 source at 15s on the east pacific rise. *Science*, *214*(4516).

Matulka, A., López, P., Redondo, J. M., & Tarquis, A. (2014). On the entrainment coefficient in a forced plume: Quantitative effects of source parameter. *Nonlinear Processes in Geophysics*, *21*(1), 269–278. doi:10.5194/npg-21-269-2014

McDuff, R. E. (1995). Seafloor hydrothermal systems: Physical, chemical, biological, and geological interactions. In S. E. Humphris, R. A. Zierenberg, L. S. Mullineaux, & R. E. Thomson (Eds.), (Chap. Physical Dynamics of Deep-Sea Hydrothermal Plumes, Vol. 91). American Geophysical Union.

Millero, F. (2013). *Chemical oceanography* (4th ed.). Boca Raton, FL: CRC Press.

Moffett, J. W., & German, C. R. (2018). The U.S.GEOTRACES Eastern Tropical Pacific Transect (GP16). *Marine Chemistry*, *201*, 1–5. doi:10.1016/j.marchem.2017.12.001

Morton, B. R., Taylor, G., & Turner, J. S. (1956). Turbulent gravitational convection from maintained and instantaneous sources. *Proceedings of the Royal Society of London. Series A, Mathematical and Physical Sciences*, *234*(1-23).

Mullineaux, L. S., Metaxas, A., Beaulieu, S. E., Bright, M., Gollner, S., Grupe, B. M., Herrera, S., Kellner, J. B., Levin, L. A., Mitarai, S., Neubert, M. G., Thurnherr, A. M., Tunnicliffe, V., Watanabe, H. K., & Won, Y. J. (2018). Exploring the ecology of deep-sea hydrothermal vents in a metacommunity framework. doi:10.3389/fmars.2018.00049

Nishioka, J., Obata, H., & Tsumune, D. (2013). Evidence of an extensive spread of hydrothermal dissolved iron in the Indian Ocean. *Earth and Planetary Science Letters*, *361*, 26–33. doi:10.1016/j.epsl.2012.11.040

Padman, L., & Erofeeva, S. (2004). A barotropic inverse tidal model for the arctic ocean. *Geophysical Research Letters*, *31*(2). doi:10.1029/2003GL019003. eprint: https://agupubs.onlinelibrary.wiley.com/doi/pdf/10.1029/2003GL019003

Papanicolaou, P. N., & List, E. J. (1987). Statistical and spectral properties of tracer concentration in round buoyant jets. *International Journal of Heat and Mass Transfer*, *30*(10), 2059–2071. doi:10.1016/0017-9310(87)90086-X

Papanicolaou, P. N., & List, E. J. (1988). Investigations of round vertical turbulent buoyant jets. *Journal of Fluid Mechanics*, *195*, 341–391. doi:10.1017/S0022112088002447

Phillips, B. T. (2017). Beyond the vent: New perspectives on hydrothermal plumes and pelagic biology. *Deep-Sea Research Part II: Topical Studies in Oceanography*.

Porte-Agel, F., Meneveau, C., & Parlange, M. (1998). Some basic properties of the surrogate subgrid-scale heat flux in the atmospheric boundary layer. *Boundary-Layer Meteorology*, *88*, 425–444.

Resing, J. A., Sedwick, P. N., German, C. R., Jenkins, W. J., Moffett, J. W., Sohst, B. M., & Tagliabue, A. (2015). Basin-scale transport of hydrothermal dissolved metals across the South Pacific Ocean. *Nature*, *523*(7559), 200–203. doi:10.1038/nature14577

Reveillaud, J., Reddington, E., McDermott, J., Algar, C., Meyer, J. L., Sylva, S., Seewald, J., German, C. R., & Huber, J. A. (2016). Subseafloor microbial communities in hydrogen-rich vent fluids from hydrothermal systems along the Mid-Cayman Rise. *Environmental microbiology*, *18*(6), 1970–1987. doi:10.1111/1462-2920.13173

Rona, P. A., Bemis, K. G., Silver, D., & Jones, C. D. (2002). Acoustic imaging, visualization, and quantification of buoyant hydrothermal plumes in the Ocean. *Marine Geophysical Research*, *23*(2), 147–168. doi:10.1023/A:1022481315125

Rona, P. A., & Trivett, D. A. (1992). Discrete and diffuse heat transfer at ashes vent field, Axial Volcano, Juan de Fuca Ridge. *Earth and Planetary Science Letters*, *109*(1-2), 57–71. doi:10.1016/0012-821X(92)90074-6

Ryan, W. B. F., Carbotte, S. M., Coplan, J. O., O'Hara, S., Melkonian, A., Arko, R., Weissel, R. A., Ferrini, V., Goodwillie, A., Nitsche, F., Bonczkowski, J., & Zemsky, R. (2009). Global multi-resolution topography synthesis. *Geochemistry, Geophysics, Geosystems*, *10*(3). doi:10.1029/2008GC002332. eprint: https://agupubs.onlinelibrary.wiley.com/doi/pdf/10.1029/2008GC002332

Sagaut, P., & Meneveau, C. (2006). *Large eddy simulation for incompressible flows: An introduction*. Scientific Computation. Springer Berlin Heidelberg. Retrieved from https://books.google.com/books?id=SH90vyraAT0C

Sander, S. G., & Koschinsky, A. (2011). Metal flux from hydrothermal vents increased by organic complexation. *Nature Geoscience*, *4*(3), 145–150. doi:10.1038/ngeo1088

Sarrazin, J., Rodier, P., Tivey, M. K., Singh, H., Schultz, A., & Sarradin, P. M. (2009). A dual sensor device to estimate fluid flow velocity at diffuse hydrothermal vents. *Deep-Sea Research Part I: Oceanographic Research Papers*, *56*(11), 2065–2074. doi:10.1016/j.dsr.2009.06.008

Sheng, J., Meng, H., & Fox, R. (2000). A large eddy PIV method for turbulence dissipation rate estimation. *Chemical Engineering Science*, *55*, 4423–4434.

Smagorinsky, J. (1963). General circulation experiments with the primitive equations, part i: The basic experiment. *Mon. Wea. Rev*, *91*, 99.

Smagorinsky, J. (1993). Some historical remarks on the use of nonlinear viscosities. In B. Galperin & S. Orszag (Eds.), *Large eddy simulation of complex engineering and geophysical flows* (pp. 3–36). Cambridge University Press, New York.

Sohn, R., Harris, R., Linder, C., Luttrell, K., Lovalvo, D., Morgan, L., Seyfried, W., & Shanks, P. (2017). Exploring the Restless Floor of Yellowstone Lake. *Eos*. doi:10.1029/2017eo087035

Sreenivas, K. R., & Prasad, A. K. (2000). Vortex-dynamics model for entrainment in jets and plumes. *Physics of Fluids*, *12*(8), 2101–2107. doi:10.1063/1.870455

Stüben, D., Stoffers, P., Cheminée, J. L., Hartmann, M., McMurtry, G. M., Richnow, H. H., Jenisch, A., & Michaelis, W. (1992). Manganese, methane,

iron, zinc, and nickel anomalies in hydrothermal plumes from Teahitia and Macdonald volcanoes. *Geochimica et Cosmochimica Acta*, *56*(10), 3693–3704. doi:10.1016/0016-7037(92)90162-C

Tagliabue, A., & Resing, J. (2016). Impact of hydrothermalism on the ocean iron cycle. *Philosophical Transactions of the Royal Society A: Mathematical, Physical and Engineering Sciences*, *374*(2081). doi:10.1098/rsta.2015.0291

Takai, K., Nunoura, T., Ishibashi, J. I., Lupton, J., Suzuki, R., Hamasaki, H., Ueno, Y., Kawagucci, S., Gamo, T., Suzuki, Y., Hirayama, H., & Horikoshi, K. (2008). Variability in the microbial communities and hydrothermal fluid chemistry at the newly discovered Mariner hydrothermal field, southern Lau Basin. *Journal of Geophysical Research: Biogeosciences*, *113*(2). doi:10.1029/2007JG000636

Teague, J., Miles, J., Connor, D., Priest, E., Scott, T., Naden, J., & Nomikou, P. (2017). Exploring Offshore Hydrothermal Venting Using Low-Cost ROV and Photogrammetric Techniques: A Case Study from Milos Island, Greece. *PeerJ*, (2017). doi:10.20944/preprints201710.0014.v1

Thomson, R. E., Roth, S. E., & Dymond, J. (1990). Near-inertial motions over a mid-ocean ridge: Effects of topography and hydrothermal plumes. *Journal of Geophysical Research: Oceans*, *95*(C5), 7261–7278. doi:10.1029/JC095iC05p07261. eprint: https://agupubs.onlinelibrary.wiley.com/doi/pdf/10.1029/JC095iC05p07261

Thomson, R. E., Mlhály, S. F., Rabinovich, A. B., McDuff, R. E., Veirs, S. R., & Stahr, F. R. (2003). Constrained circulation at Endeavour ridge facilitates colonization by vent larvae. *Nature*, *424*(6948), 545–549. doi:10.1038/nature01824

Thomson, R. E., Subbotina, M. M., & Anisimov, M. V. (2005). Numerical simulation of hydrothermal vent-induced circulation at Endeavour Ridge. *Journal of Geophysical Research: Oceans*, *110*(1), 1–14. doi:10.1029/2004JC002337

Thomson, R. E., Subbotina, M. M., & Anisimov, M. V. (2009). Numerical simulation of mean currents and water property anomalies at Endeavour Ridge: Hydrothermal versus topographic forcing. *Journal of Geophysical Research: Oceans*, *114*(9). doi:10.1029/2008JC005249

Thurnherr, A. M., Richards, K. J., German, C. R., Lane-Serff, G. F., & Speer, K. G. (2002). Flow and mixing in the rift valley of the Mid-Atlantic Ridge. *Journal of Physical Oceanography*, *32*(6), 1763–1778. doi:10.1175/1520-0485(2002)032<1763:FAMITR>2.0.CO;2

Thurnherr, A. M., & Laurent, L. C. (2012). Turbulence observations in a buoyant hydrothermal plume on the east pacific rise. *Oceanography*, *25*(1), 180–181. doi:10.5670/oceanog.2012.15

Turner, J. S. (1986). Turbulent entrainment: The development of the entrainment assumption, and its application to geophysical flows. *Journal of Fluid Mechanics*, *173*, 431–471. doi:10.1017/S0022112086001222

Wajsowiczw, R. C. (1993). A consistent formulation of the anisotropic stress tensor for use in models of the large-seale oeean cireulation. *105*, 333–338.

White, S. N., Chave, A. D., & Reynolds, G. T. (2002). Investigations of ambient light emission at deep-sea hydrothermal vents. *Journal of Geophysical Research: Solid Earth*, *107*(B1), EPM 1–1–EPM 1–13. doi:10.1029/2000jb000015

Williams, G. (1972). Friction term formulation and convective instability in a shallow atmosphere. *J. Atmosph. Sci. 29*, 870–876.

Wright, J., & Rothery, D. (1989). *The ocean basins: Their structure and evolution* (2nd ed.). Oxford: Butterworth-Heinemann.

Wu, J., Wells, M. L., & Rember, R. (2011). Dissolved iron anomaly in the deep tropical-subtropical Pacific: Evidence for long-range transport of hydrothermal iron. *Geochimica et Cosmochimica Acta*, *75*(2), 460–468. doi:10.1016/j.gca.2010.10.024

Wu, X. (2017). Inflow Turbulence Generation Methods. *Annual Review of Fluid Mechanics*, *49*(1), 23–49. doi:10.1146/annurev-fluid-010816-060322

Xu, G., & DiIorio, D. (2011). The relative effects of particles and turbulence on acoustic scattering from deep-sea hydrothermal vent plumes. *J. Acoust. Soc. Am. 130*(4). doi:10.1121/1.3624816

Xu, G., & DiIorio, D. (2012). Deep sea hydrothermal plumes and their interaction with oscillatory flows. *Geochemistry Geophysics Geosystems. 13*, Q0AJ01. doi:10.1029/2012GC004188

Xu, G., Jackson, D. R., & Bemis, K. G. (2017). The relative effects of particles and turbulence on acoustic scattering from deep-sea hydrothermal vent plumes revisited. *Journal of the Acoustical Society of America*, *141*, 1446–1458.

Xu, G., & Lavelle, J. W. (2017). Circulation, hydrography, and transport over the summit of Axial Seamount, a deep volcano in the Northeast Pacific. *Journal of Geophysical Research: Oceans*, *122*(7), 5404–5422. doi:10.1002/2016JC012464

Xu, G., McGillicuddy, D. J., Mills, S. W., & Mullineaux, L. S. (2018). Dispersal of hydrothermal vent larvae at east pacific rise 9–10+.1667*em*°n segment. *Journal of Geophysical Research*.

Xu, G., & Di Iorio, D. (2012). Deep sea hydrothermal plumes and their interaction with oscillatory flows. *Geochemistry, Geophysics, Geosystems*, *13*(1). doi:10.1029/2012GC004188

Yu, H., Kanov, K., Perlman, E., Graham, J., Frederix, E., Burns, R., Szalay, A., Eyink, G., & Meneveau, C. (2012). Studying lagrangian dynamics of turbulence using on-demand fluid particle tracking in a public turbulence database. *Journal of Turbulence*, *13*, N12. doi:10.1080/14685248.2012.674643. eprint: https://doi.org/10.1080/14685248.2012.674643